MRI-guided robot for needle interventions in the prostate

ISBN: 978-90-393-5552-7

Print: Nauta en Haagen B.V.

MRI-guided robot for needle interventions in the prostate

MRI-geleide robot voor naaldinterventies in de prostaat

(met een samenvatting in het Nederlands)

Proefschrift

ter verkrijging van de graad van doctor aan de Universiteit Utrecht
op gezag van de rector magnificus, prof.dr. G.J. van der Zwaan,
ingevolge het besluit van het college voor promoties
in het openbaar te verdedigen
op dinsdag 24 mei 2011 des middags te 4.15 uur

door

Michiel Robertus van den Bosch

geboren op 11 januari 1981 te Nijmegen

Promotor: Prof. dr. ir. J.J.W. Lagendijk

Co-promotoren: Dr. ir. M.A. Moerland
Dr. M. van Vulpen

Het beschreven werk werd mede mogelijk gemaakt door een subsidie van KWF Kankerbestrijding (UU 2006-3638).

Deze uitgave is tot stand gekomen met de financiële steun van Nucletron B.V., Philips Healthcare, Elekta B.V. en CurieMed B.V.

Contents

1 Introduction

1.1. MRI guidance in prostate interventions

Magnetic resonance imaging (MRI) can be applied to non-invasively visualize patient's anatomy. Thanks to its superior soft tissue contrast, the prostate and surrounding critical structures can better be discriminated on MRI with respect to other image modalities, e.g. ultrasound (US), cone-beam computed tomography (CT) and portal imaging (see Figure 1.1).

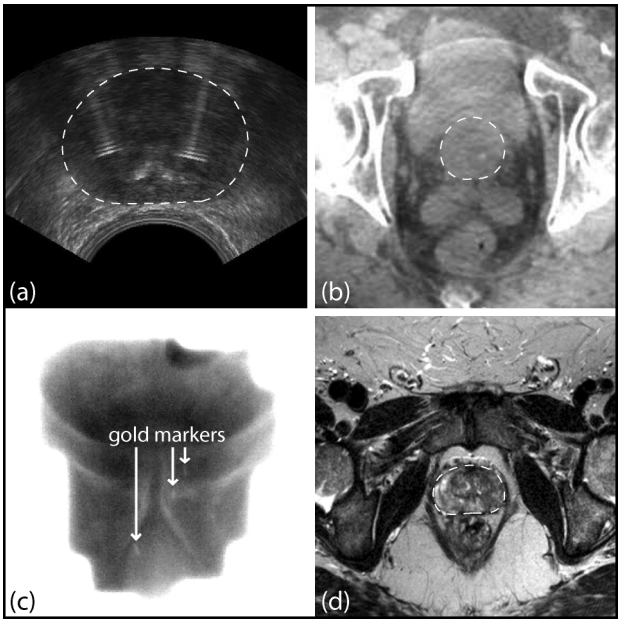

Figure 1.1. *Prostate localization with different image modalities: (a) US, (b) cone-beam CT [6], (c) MV portal imaging, (d) MRI. The dashed line represents the prostate contour. The arrows indicate the location of the ficudial gold markers, which can be used as a surrogate for the prostate itself.*

Furthermore, tumour suspicious regions can be defined using MRI techniques, such as T_2-weighted imaging, dynamic contrast-enhanced (DCE) MRI, diffusion-weighted imaging (DWI), and MR spectroscopy (MRS) [1-3]. T_2-weighted imaging characterizes the transverse magnetization relaxation rate of the

tissue, while DCE-MRI denotes the tissue perfusion and microvascular vessel permeability after intra-vascular injection of an contrast agent. In DWI, the diffusion restriction of water molecules in the tissue is indicated. The levels of different metabolites in the tissues can be measured by MRS.

The superior visualisation of patient's anatomical structures and tumour suspicious regions using MRI, provide the ability to improve the techniques applied to diagnose or treat prostate cancer. For example by increasing the detection rate of prostate biopsies [3] or, in case of tumour irradiation with external beam radiotherapy or brachytherapy, by escalating the dose to the tumour, while (better) sparing the surrounding critical structures [4,5].

Therefore, multiple institutes intend to perform or are performing diagnostic and treatment interventions inside the MR scanner to have online MRI during the intervention. In external beam radiotherapy, special MR scanners are integrated with linear accelerators or cobalt sources to achieve this goal [7-9]. Clinical MR scanners are already suitable to perform MRI-guided biopsies [10,11] and to position brachytherapy catheters or needles in the prostate under MRI guidance [10,12].

Upcoming minimally invasive treatment techniques, such as cryoablation (freezing) [13], laser ablation (heating) [14] and high intensity focused ultrasound (heating) [15] can also be applied in clinical MR scanners.

1.2. MR compatible robotic devices

Due to the MR bore, the access to the patient is restricted. To overcome this limitation and to accurately position the needle or the transducer needed to perform the intervention under real-time MRI guidance, MR compatible robotic devices have been developed at several institutes [16-23]. These systems have to deal with technical difficulties, such as the restriction to use solely non-ferromagnetic materials, the needle-induced prostate deformation, image artefacts caused by the robotic device and needle, and undesired tissue heating around the needle tip due to the resonating radio frequency (RF) waves that are needed to generate an MR image.

In general there are two different robotic devices. The first type automatically aligns the needle under MRI guidance, but requires a manual needle insertion.

These systems are generally called robotic needle guide manipulators. The second robotic type automatically inserts the needle under MRI guidance into the prostate after manual or automated needle alignment.

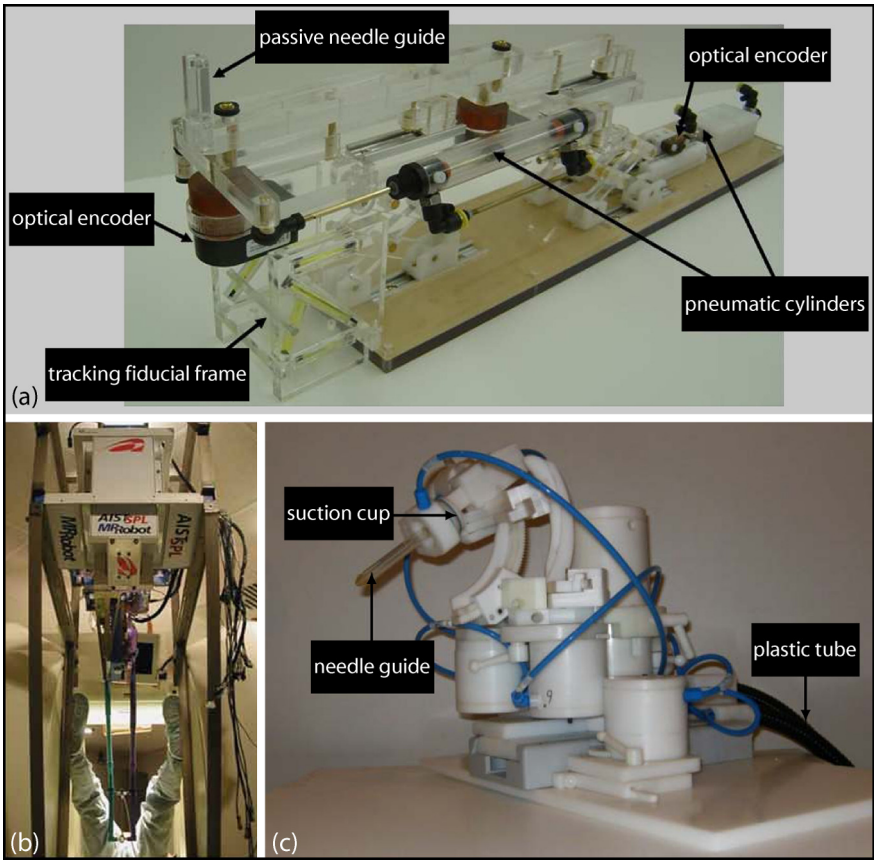

Figure 1.2. *(a) Robotic manipulator for transperineal prostate needle placement in a closed bore 3 T MR scanner [19], (b) Robotic device for needle placement during a transperineal prostate biopsy procedure in an open 0.5 T MR scanner [16], (c) Robotic manipulator for transrectal prostate biopsies in a closed bore 3 T MR scanner [17,24].*

Three remarkable robotic needle guide manipulators in prostate interventions are described by DiMaio *et al.* [16], Fischer *et al.* [19,20], and Schouten *et al.* [17], respectively (see Figure 1.2).

Fischer *et al.* described an MR-compatible robotic manipulator with two active and one passive (the encoded needle insertion) degrees of freedom [19,20].

Pneumatic cylinders realize the actuation, while optical encoders are used for position sensing. The manipulator does not contain any ferromagnetic material and can be applied for transperineal prostate needle placement in a 3 T closed bore MR scanner. By the use of rigid glass tubes filled with contrast agent (the tracking fiducial frame), the robot and image coordinates are registered. When the manipulator is placed in the desired position under MRI guidance, the needle is manually inserted along the needle guide. During the insertion, the needle is monitored by the encoded slider and real-time MR images. The reported root mean square value of the *ex vivo* needle alignment accuracy by the pneumatic control system was <1mm per axis [19].

DiMaio *et al.* reported a robotic device for needle placement that can be used during a transperineal prostate biopsy procedure in an open 0.5 T MR scanner (GE Signa SP, Milwaukee, WI) [16]. The robot is made of paramagnetic materials, such as titanium alloy and plastics, and driven by non-magnetic ultrasonic motors [18]. Its mechanical main body is positioned above the head of the surgeon and two rigid arms reach down into the surgical field. The ends of the arms are linked to form a tool holder, which in this study is a linear needle guide. The needle guide is positioned with the use of MR images and an optical tracker. Prior to the biopsy procedure 1.5 T MR images with better image contrast are acquired and fused with the 0.5 T MR images using a non-rigid registration model. Once the needle guide is in the desired position, the needle is manually inserted through the needle guide under MRI guidance, using fast MR scans. In gelatin phantom experiments [16], the robotic device placed needles within 2 mm of their intended targets. However, it is likely that the *in vivo* needle placement accuracy is worse, since patient movement, tissue deformation and needle deflection due to heterogeneous tissue are not covered in these gelatin experiments.

Schouten *et al.* described a robotic needle guide manipulator with five degrees of freedom that can be used to perform transrectal prostate biopsies in a closed bore 3 T MR scanner (Magnetom Trio, Siemens Medical Solutions, Erlangen, Germany) [17]. The robotic manipulator is constructed of plastic and can be controlled using a controller unit outside the scanning room. The needle guide (Invivo, Schwerin, Germany) contains a gadolinium-doped water reservoir to make the needle guide and its work channel visible on MR images. Furthermore, the needle guide has a mechanical safety mechanism consisting of a suction cup, which will automatically release when the force to the patient's rectal wall reaches a primary set value. When the needle guide is placed under

MRI guidance in the desired position, the patient table with the robotic manipulator is moved out of the MR bore. Then, an MR compatible biopsy gun (Invivo, Schwerin, Germany) is manually inserted through the work channel of the needle guide to take the biopsy. After the needle insertion, the patient table can be moved to its original position for the acquisition of new MR images. On these MR images, the needle position can be verified. In an agar phantom experiment the average in-plane error was 3.0 mm (range: 0-5.6 mm) [17]. Again, *in vivo* needle placement accuracy is likely to be worse, since patient movement, tissue deformation and needle deflection due to heterogeneous tissue are not covered in these agar experiments.

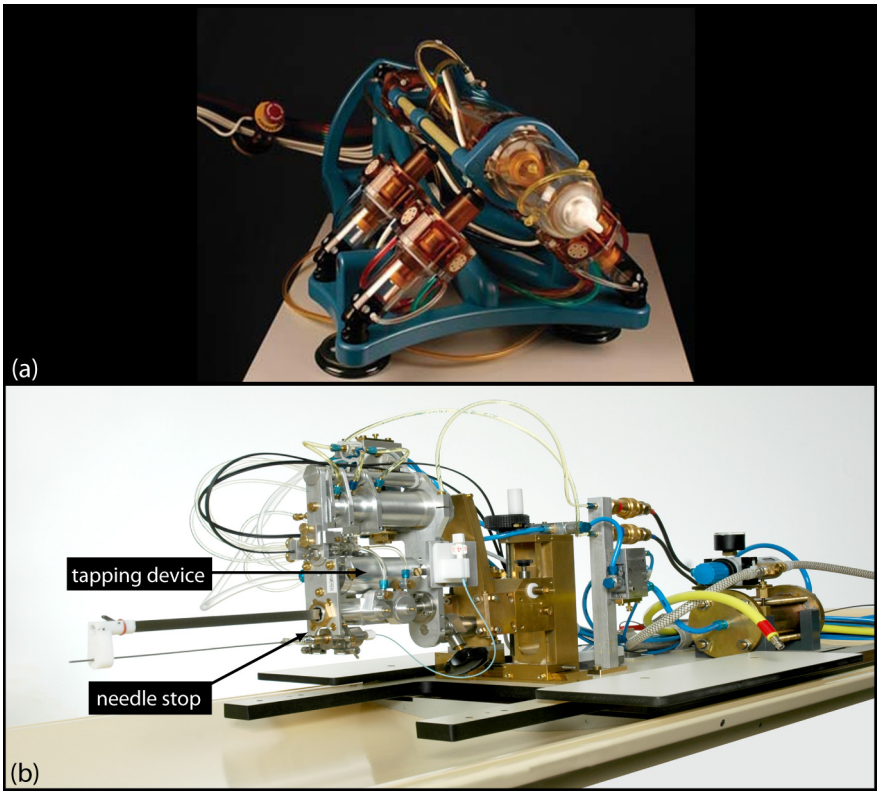

Figure 1.3. *Robots that (a) shoot [21,25] or (b) tap [23] the needle under MRI guidance to the target position to perform MRI-guided transperineal needle interventions in the prostate.*

Two robotic devices that can automatically insert a needle into the patient's prostate under MRI guidance are the one described by Muntener *et al.* [21] and

the one that is built at our institute: the University Medical Center Utrecht (UMCU) robot [23] (see Figure 1.3).

Muntener *et al.* reported an MR compatible robot with five degrees of freedom that fits inside standard closed-bore MR scanners to perform MRI-guided transperineal needle interventions of the prostate [21]. It consists of nonmagnetic and dielectric materials, such as fiber glass, ceramics, plastics, and rubber. The robot has been tested for MR compatibility in magnetic field strengths up to 7 T [22]. It uses pneumatic actuators to place and orient the robot as desired, while the actuation is encoded using fiber optics. A registration marker is used to register the coordinate system of the robot to the coordinate system of the image. Using MR images, the desired needle insertion point on the perineum and the target in the prostate are selected. Next, it is verified on the MR images that neither the rectum nor the urethra would be affected by the intended needle trajectory. Once the robot is in the desired position and the appropriate needle insertion depth has been set, the needle is shot to the target. In dogs, the median error for MRI-guided needle positioning and seed positioning was 2.0 mm (range: 0.9–3.2 mm) and 2.5 mm (range: 1.5–10.5 mm), respectively [21]. Although these values were obtained during *in vivo* experiments with probably tissue deformation, the positioning errors were defined in image coordinates (this error does not include deviations due to tissue deformation).

At our institute, we built an MR compatible robot that can be used for transperineal prostate interventions in a closed-bore 1.5 T MR scanner [23]. The robot is made of polymers and non-ferromagnetic materials, such as copper, titanium and aluminium. It has five degrees of freedom: four passive and one active, which is the needle insertion. The prostate accessibility is ensured using a needle entrance point just underneath the skin of patient's perineum, which is also the rotation point of the robotic needle insertion [27,28]. The UMCU robot contains a tapping device to tap the needle stepwise towards the prostate. Lagerburg *et al.* proved that needle tapping minimizes tissue deformation with respect to manual needle insertion [26]. Monitoring the needle trajectory using fast MR scans and stepwise needle tapping, provides the ability to retract the needle in time, in case of unexpected needle deflection or risk of piercing a critical structure. A hydraulic cylinder with needle stop, which displacement is measured by a small ferromagnetic potentiometer, limits the maximum needle insertion depth per tap. In the first patient experiments, the needle was manually aligned to the longitudinal axis of the scanner and pushed

just beneath the patient's skin through a predefined needle insertion point. Then, the needle trajectory was verified on a high resolution MR scan and the needle was automatically tapped to the target using a remote control outside the scanning room. During the stepwise tapping, the needle was tracked by fast orthogonal MR scans.

1.3. Outline of this thesis

This thesis describes the development and quality assurance of the UMCU robot. Furthermore, it reports the first *in vivo* experiences with this robot and discusses its possible future applications.

In Chapter 2, the results are presented of a feasibility study on the dose coverage in low-dose-rate (LDR) brachytherapy using divergent needle insertion methods with one or two rotation points of needle insertion. Chapter 3 describes a new method to detect undesired situations with risk of tissue heating around the needle tip caused by the RF waves needed to generate an MR image. The method is based on RF induced image artefacts and applied in phantom experiments. In Chapter 4, development considerations and quality assurance methods of MRI-guided robotic devices dedicated for needle interventions are listed. Chapter 5 reports the proof of principle of our robot. Four fiducial gold markers are placed under MRI guidance inside the prostate of a prostate cancer patient. In Chapter 6, it is investigated whether it is possible to quantify local prostate deformations, due to the needle insertion, by creating artificial landmarks in the prostate using single shot MR tagging. Chapter 7 discusses the impact of the various studies of this thesis and the future applications of the UMCU robot.

References

[1] Delongchamps NB, Rouanne M, Flam T, Beuvon F, Liberatore M, Zerbib M, Cornud F, "Multiparametric magnetic resonance imaging for the detection and localization of prostate cancer: combination of T2-weighted, dynamic contrast-enhanced and diffusion-weighted imaging," *BJU Int.* Nov 2. doi: 10.1111/j.1464-410X.2010.09808.x. [ahead of print] (2010).

[2] Groenendaal G, Moman MR, Korporaal JG, van Diest PJ, van Vulpen M, Philippens MEP, van der Heide UA, "Validation of functional imaging with pathology for tumor delineation in the prostate," *Radiother Oncol.* **94**, 145-150 (2010).

[3] Labanaris AP, Engelhard K, Zugor V, Nützel R, Kühn R, "Prostate cancer detection using an extended prostate biopsy schema in combination with additional targeted cores from suspicious images in conventional and functional endorectal magnetic resonance imaging of the prostate," *Prostate Cancer Prostatic Dis.* **13**, 65-70 (2010).

[4] van Vulpen M, van der Heide UA, "FLAME: Investigate the benefit of a focal lesion ablative microboost in prostate cancer," www.clinicaltrials.gov/ct2/show/NCT01168479, visited 15-11-2011.

[5] Daanen V, Gastaldo J, Giraud JY, Fourneret P, Descotes JL, Bolla M, Collomb D, Troccaz J, "MRI/TRUS data fusion for brachytherapy," *Int J Med Robot.* **2**, 256-261 (2006).

[6] Smitsmans MHP, de Bois J, Sonke JJ, Betgen A, Zijp LJ, Jaffray DA, Lebesque JV, van Herk M, "Automatic prostate localization on cone-beam CT scans for high precision image-guided radiotherapy," *Int J Radiat Oncol Biol Phys.* **15**, 975-984 (2005).

[7] Lamey M, Burke B, Blosser E, Rathee S, De Zanche N, Fallone BG, "Radio frequency shielding for a linac-MRI system," *Phys Med Biol.* **55**, 995-1006 (2010).

[8] Raaymakers BW, Lagendijk JJW, Overweg J, Kok JGM, Raaijmakers AJE, Kerkhof EM, van der Put RW, Meijsing I, Crijns SPM, Benedosso F, van Vulpen M, de Graaff CHW, Allen J, Brown KJ, "Integrating a 1.5 T MRI scanner with a 6 MV accelerator: proof of concept," *Phys Med Biol.* **54**, 229-237 (2009).

[9] Kron T, Eyles D, Schreiner JL, Battista J, "Magnetic resonance imaging for adaptive cobalt tomotherapy: A proposal," *J Med Phys.* **31**, 242-254 (2006).

[10] Susil RC, Camphausen K, Choyke P, McVeigh ER, Gustafson GS, Ning H, Miller RW, Atalar E, Coleman CN, Ménard C, "System for prostate brachytherapy and biopsy in a standard 1.5 T MRI scanner," *Magn Reson Med.* **52**, 683-687 (2004).

[11] Engelhard K, Hollenbach HP, Kiefer B, Winkel A, Goeb K, Engehausen D, "Prostate biopsy in the supine position in a standard 1.5-T scanner under real time MR-imaging control using a MR-compatible endorectal biopsy device," *Eur Radiol.* **16**, 1237-1243 (2006).

[12] Ares C, Popowski Y, Pampallona S, Nouet P, Dipasquale G, Bieri S, Ozsoy O, Rouzaud M, Khan H, Miralbell R, "Hypofractionated boost with high-dose-rate brachytherapy and open magnetic resonance imaging-guided implants for locally aggressive prostate cancer: a sequential dose-escalation pilot study," *Int J Radiat Oncol Biol Phys.* **75**, 656-663 (2009).

[13] Josan S, Bouley DM, van den Bosch M, Daniel BL, Butts Pauly K, "MRI-guided cryoablation: In vivo assessment of focal canine prostate cryolesions," *J Magn Reson Imaging.* **30**, 169-176 (2009).

[14] Woodrum DA, Gorny KR, Mynderse LA, Amrami KK, Felmlee JP, Bjarnason H, Garcia-Medina OI, McNichols RJ, Atwell TD, Callstrom MR, "Feasibility of 3.0T magnetic resonance imaging-guided laser ablation of a cadaveric prostate," *Urology.* **75**, 1514.e1-1514.e6 (2010).

[15] Chopra R, Burtnyk M, N'djin WA, Bronskill M, "MRI-controlled transurethral ultrasound therapy for localised prostate cancer," *Int J Hyperthermia.* **26**, 804-821 (2010).

[16] DiMaio SP, Pieper S, Chinzei K, Hata N, Haker SJ, Kacher DF, Fichtinger G, Tempany CM, Kikinis R, "Robot-assisted needle placement in open MRI: system architecture, integration and validation," *Comput Aided Surg.* **12**, 15-24 (2007).

[17] Schouten MG, Ansems J, Renema WKJ, Bosboom D, Scheenen TWJ, Fütterer JJ, "The accuracy and safety aspects of a novel robotic needle guide manipulator to perform transrectal prostate biopsies," *Med Phys.* **37**, 4744-4750 (2010).

[18] Chinzei K, Hata N, Jolesz F, Kikinis R, "Surgical assist robot for the active navigation in the intraoperative MRI: Hardware design issues," *Proceedings of the IEEE/RSJ International Conference on Intelligent Robots and Systems*, Takamatsu, Japan, 727–732 (2000).

[19] Fischer GS, Iordachita I, Csoma C, Tokuda J, Dimaio SP, Tempany CM, Hata N, Fichtinger G, "MRI-Compatible Pneumatic Robot for Transperineal Prostate Needle Placement," *IEEE ASME Trans Mechatron.* **13**, 295-305 (2008).

[20] Fischer GS, DiMaio SP, Iordachita I, Fichtinger G, "Robotic Assistant for Transperineal Prostate Interventions in 3T Closed MRI," *Med Image Comput Comput Assist Interv.* **10**, 425-433 (2007).

[21] Muntener M, Patriciu A, Petrisor D, Schär M, Ursu D, Song DY, Stoianovici D, "Transperineal prostate intervention: robot for fully automated MR imaging-system description and proof of principle in a canine model," *Radiology.* **247**, 543-549 (2008).

[22] Muntener M, Patriciu A, Petrisor D, Mazilu D, Bagga H, Kavoussi L, Cleary K, Stoianovici D, "Magnetic resonance imaging compatible robotic system for fully automated brachytherapy seed placement," *Urology.* **68**, 1313-1317 (2006).

[23] van den Bosch MR, Moman MR, van Vulpen M, Battermann JJ, Duiveman E, van Schelven LJ, de Leeuw H, Lagendijk JJW, Moerland MA, "MRI-guided robotic system for transperineal prostate interventions: proof of principle.", *Phys Med Biol.* **55**, 133-140. Feb 10 (2010).

[24] Fütterer JJ, Schouten MG, Scheenen TWJ, Barentsz JO, "MR-compatible transrectal prostate biopsy robot: a feasibility study", *oral presentation at the joint annual meeting ISMRM-ESMRMB*, Stockholm, Sweden, 2010.

[25] Adam Cunha J, Hsu IC, Pouliot J, Roach III M, Shinohara K, Kurhanewicz J, Reed G, Stoianovici D, "Toward adaptive stereotactic robotic brachytherapy for prostate cancer: demonstration of an adaptive workflow incorporating inverse planning and an MR stealth robot," *Minim Invasive Ther Allied Technol.* **19**,189-202 (2010).

[26] Lagerburg V, Moerland MA, van Vulpen M, Lagendijk JJW, "A new robotic needle insertion method to minimise attendant prostate motion," *Radiother Oncol.* **80**, 73-77 (2006).

[27] Van Gellekom MPR, Moerland MA, Battermann JJ, Lagendijk JJW, "MRI-guided prostate brachytherapy with single needle method-a planning study," *Radiother Oncol.* **71**, 327-332 (2004).

[28] van den Bosch MR, Lips IM, Lagerburg V, van Vulpen M, Lagendijk JJW, Moerland MA, "Feasibility of adequate dose coverage in permanent prostate brachytherapy using divergent needle insertion methods." *Radiother Oncol.* **86**, 120-125 (2008).

This chapter has been published as:

van den Bosch MR, Lips IM, Lagerburg V, van Vulpen M, Lagendijk JJW, Moerland MA, "Feasibility of adequate dose coverage in permanent prostate brachytherapy using divergent needle insertion methods," *Radiother Oncol.* **86**, 120-125 (2008).

Feasibility of adequate dose coverage in permanent prostate brachytherapy using divergent needle insertion methods

2

Abstract

Background and purpose: The purpose of this study is to investigate the feasibility of adequate dose coverage in permanent prostate brachytherapy using divergent needle insertion methods. These methods can be useful in magnetic resonance imaging (MRI) guided needle insertion techniques to avoid pubic arch interference.

Methods and materials: MRI data was collected from 10 patients with T1-T2 prostate cancer. An inverse planning algorithm based on simulated annealing was used to optimize the dose distribution for three needle insertion methods: divergent needles with a single rotation point, divergent needles with a double rotation point, and current parallel needle insertion method. The dose constraints were based on our clinical criteria and the recent ESTRO/EAU/EORTC recommendations.

Results: If the planning target volume (PTV) surrounded the prostate and only intraprostatic seeds were allowed, the mean PTV volume that received 100% of the prescribed dose (V_{100}) was 99% for all needle insertion methods. If the PTV was increased to the prostate with a 3 mm margin, the mean PTV V_{100} equalled 94%, 95%, and 94% for the single rotation point, double rotation point and current parallel needle insertion method, respectively. If in the latter case the tips of the seeds were placed 3 mm outside the apex and base of the prostate, the mean PTV V_{100} was 96% for all needle insertion methods.

Conclusion: This planning study shows that it is feasible to generate an adequate dose coverage using divergent needle insertion methods.

2.1. Introduction

Current permanent prostate brachytherapy techniques use transrectal ultrasound (TRUS) and a transperineal template to guide parallel needle insertion for seed delivery [2,15]. In general, the introduction of an implant technique is associated with a learning curve and operator-dependent implant quality [1,2,16]. A steep learning curve and more consistent results may come from the use of better image modalities like magnetic resonance imaging (MRI) to guide interactive needle insertion and to verify implant quality [1,11], and from the use of robotics.

We are currently developing a MRI compatible single needle implant robot that fits inside a closed MR scanner [18]. It taps the needle under different angles through a specific point (rotation point) just below the perineum skin into the prostate to avoid pubic arch interference and to ensure sufficient access to the prostate [8]. The resulting divergent needle bundle implies a larger inaccessible prostate volume behind the urethra compared to the current parallel needle insertion method (see Figure 2.1), which may lead to underdosage. Applying two rotation points can reduce this volume.

Various studies have shown that inverse planning by simulated annealing (IPSA) is a useful tool to find the optimal dose distribution [7,9,10]. It needs to be adapted for the divergent needle insertion method and for dose constraints based on our clinical criteria and the recent ESTRO/EAU/EORTC recommendations [15].

The purpose of this study is to investigate the feasibility of adequate dose coverage in permanent prostate brachytherapy using divergent needle insertion methods. This is done by comparing the optimal dose distribution obtained from our IPSA algorithm for the following needle insertion methods: parallel needle insertion method, single rotation point method, and double rotation point method (see Figure 2.1).

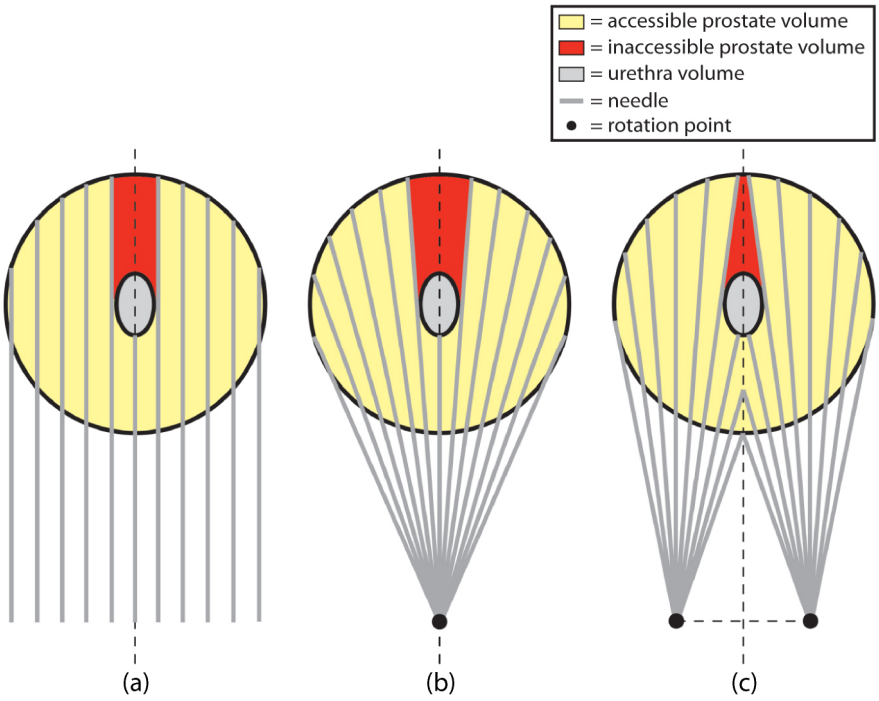

Figure 2.1. *Schematic visualization of the difference in inaccessible prostate volume in a coronal plane for the (a) current parallel needle insertion method, (b) single rotation point method, (c) double rotation point method.*

2.2. Methods and materials

For this study we adapted the IPSA algorithm for parallel needle brachytherapy techniques described by Pouliot *et al*. [12] and Lessard *et al*. [9,10] to an IPSA algorithm for permanent prostate brachytherapy with iodine-125 seeds that also includes divergent needle implant methods. It optimizes the dose distribution by placing seeds at or removing seeds from possible seed positions. In order to obtain an adequate level of accuracy we used a voxel size of 1.0 x 1.0 x 1.0 mm^3. Our structures of interest, seed position definitions and dose constraints are described below.

2.2.1. Structures of interest

MRI datasets were collected from 10 patients with T1-T2 prostate cancer, a prostate volume ≤ 50 cm^3, and a rectum that is 'straight' to ensure the rectum will not limit the accessibility to the prostate in any needle insertion method. The patient datasets included a 3D balanced steady state free precession (bSSFP) scan of the abdomen (voxel size ≤0.7 x 0.7 x 1.0 mm^3) and a survey scan (voxel size ≤1.8 x 1.8 x 25.0 mm^3).

For every patient, the prostate, rectum, bladder and urethra were delineated on the abdomen scan and reviewed by a radiation oncologist. The urethra diameter was set to a 10 French gauge catheter which use is recommended to avoid distension of the urethra [15]. Furthermore two different planning target volume (PTV) definitions were applied. In the first case, the PTV surrounded the prostate according to our clinical protocol. This definition will be indicated as PTV-P(rostate). In the second case, the PTV surrounded the prostate with a 3 mm margin to include possible extraprostatic extension (EPE) according to the recent ESTRO/EAU/EORTC recommendations [15]. This definition will be indicated as PTV-P(rostate)M(argin).

The survey scan was used to determine the central rotation point. This point is the intersection point of the body contour, the urethra plane (in which the urethra is situated), and a line parallel to the MR scanner table passing 18 gauge (needle thickness) beneath the urethra. In the double rotation point method, the rotation points are placed at 5 mm laterally from the central rotation point and perpendicular to the urethra plane.

2.2.2. Seed positions

To define the seed positions we make use of virtual templates and virtual needles. The needle positions of the simulated parallel needle insertion method mimic the ones of the current prostate implant technique. A virtual rectangular template with 5 mm spaced holes is placed perpendicularly to the urethra plane against the perineum. The central hole of the template is positioned at the central rotation point and virtual needles are placed parallel to each other through the template holes. Only needles that intersect the prostate contour are used to define the available seed positions.

In the single rotation point method a virtual hemispherical template, also with 5 mm spaced holes, is placed at the most distal prostate voxel with its centre at the central rotation point. In the double rotation point method two hemispherical templates are placed with the two lateral rotation points as centres. In this case needles covering the right part of the prostate pass through holes in the right template and needles covering the left part through the left template (see Figure 2.1c). Needles do not cross the urethra plane. Only the needles, passing from a rotation point to a template hole, that intersect the prostate contour are candidates to hold seeds.

Since extraprostatic seeds seem to have a higher risk of unwanted seed migration [5], we prefer to place all seeds inside the prostate. However it may be necessary to place seeds (partly) outside the apex and base of the prostate to achieve an adequate PTV-PM dose coverage [4]. Therefore we implemented both situations in our in-house developed algorithm by applying a seed placement margin at the apex and base of the prostate. In case of intraprostatic seeds the seed placement margin is 0 mm. In the other case we set the seed placement margin to 3 mm (so the tips of the seeds are situated 3 mm outside the apex and base of the prostate).

The seed positions are defined in three steps. First, virtual seeds are placed at the surface of the prostate, but not behind the urethra (see Figure 2.2a). Second, seeds are positioned between the surface seeds at equal interdistance (see Figure 2.2b). Third, single seeds are placed at the apex or base of the prostate depending on the needle position. In two adjacent needles, opposite seed locations are preferred to make the dose distribution homogeneous (see Figure 2.2c).

The seeds are simulated according to the Amersham 6711 I-125 seed model [14]. The seed dimensions are 0.8 mm in diameter and 4.6 mm in length. The air kerma strength of the seeds is set to 0.55 U (1 U = 1 μGy m^2 h^{-1}). For each seed position, the dose distribution is calculated using its orientation and the 2D dose-rate equation of the TG-43 report [14].

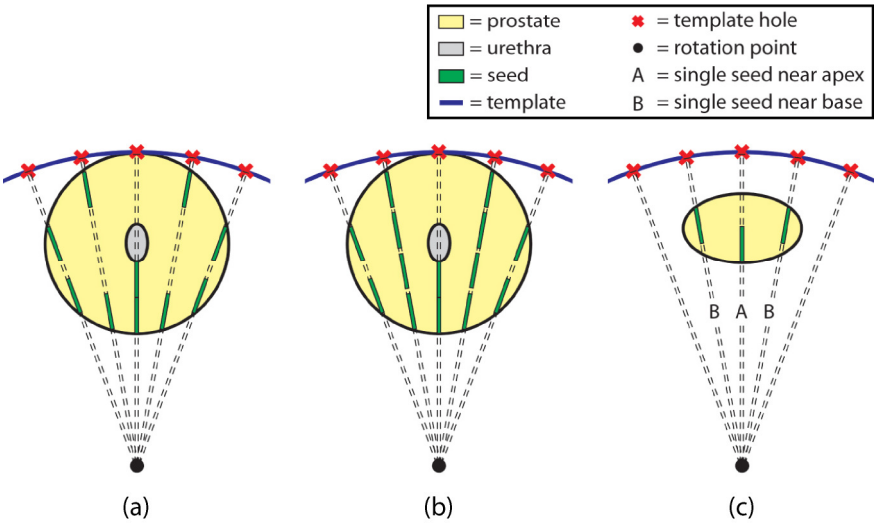

Figure 2.2. *Schematic visualization of the steps that are taken to define the seed positions. This example represents the single rotation point method. (a) First, seeds are positioned at the surface of the prostate, but not behind the urethra, (b) Second, seeds are placed between the surface seeds at equal interdistance, (c) Third, single seeds are positioned at apex or base of the prostate depending on the needle position as shown for a more dorsal oblique slice.*

2.2.3. Used dose constraints

According to the difference in PTV definition and the seed placement margin, the following three situations of interest were defined:

- situation A: PTV-P and seed placement margin of 0 mm
- situation B: PTV-PM and seed placement margin of 0 mm
- situation C: PTV-PM and seed placement margin of 3 mm

An overview of the applied dose constraints is shown in Table 2.1.

In general, we made use of two types of dose constraints, namely hard and soft dose constraints. Hard dose constraints are used to distinguish a useful and unacceptable dose distribution. The applied hard dose constraints correspond with our current clinical criteria (situation A) and reflect the ESTRO/EAU/EORTC recommendations (situation B & C) [15]. Soft dose constraints are used for balancing one dose constraint against another to get the optimal dose distribution.

Breaking a dose constraint results in a penalty (P) according to equation 2.1. The offset (β) gives a high penalty at the moment a (hard) dose constraint is broken.

$$P = \begin{cases} w(C_{min} - \Theta) + \beta & if \quad \Theta < C_{min} \\ w(\Theta - C_{max}) + \beta & if \quad \Theta > C_{max} \\ 0 & if \quad C_{min} \leq \Theta \leq C_{max} \end{cases} \tag{2.1}$$

where w is the weight, Θ is the obtained value, C_{min} is the dose constraint with a minimal value, C_{max} is the dose constraint with a maximal value.

Table 2.1. Overview of the applied dose constraints for the situations A, B and C

Dose constraint type	Parameter		Situation A		Situation B & C	
			w	β	w	β
Soft	PTV-PM	V_{100} = 100%	-	-	1.0	0
	PTV-P	V_{100} = 100%	1.0	0	1.0	0
		V_{150} = 66.7%	0.6	0	0.6	0
		V_{200} = 33.3%	0.6	0	0.6	0
	Rectum	V_{100} = 0%	0.4	0	0.4	0
	Urethra	V_{150} = 0%	0.2	0	0.2	0
Hard	PTV-PM	$V_{100} \geq$ 95%	-	-	100	100
		$V_{150} \leq$ 50%	-	-	100	100
	PTV-P	$V_{100} \geq$ 95%	100	100	100	100
		V_{150} < 70%	100	100	100	100
		V_{200} < 35%	100	100	100	100
	Rectum	D_{2cc} < 100%	100	100	100	100
		$D_{0.1cc}$ < 200Gy	100	100	100	100
	Urethra	$D_{10\%}$ < 150%	100	100	100	100
		$D_{30\%}$ < 130%	100	100	100	100

Where V_{100} is the volume that receives at least 100% of the prescribed dose (144 Gy); D_{2cc} is the dose to 2cc of the structure; $D_{10\%}$, dose to 10% of the structure.

2.3. Results

Optimal dose distributions were generated using our in-house developed IPSA algorithm for 10 patients, concerning the three situations (A, B, and C) and the three needle insertion methods (parallel, single rotation point and double rotation point). The mean prostate volume was 41 cm^3 (range 28 – 50 cm^3). An overview of the results is shown in Table 2.2.

Adequate dose coverage and uniformity were accomplished inside the prostate, while the urethra and rectum were spared sufficiently in all dose distributions of situation A (see Table 2.2).

In situation B, adequate dose coverage of the PTV-PM is difficult to achieve. Even in the case of the double rotation point, two out of ten dose distributions do not meet the clinical criteria. The algorithm places clusters of seeds at the base and apex of the prostate, nearby the urethra, to accomplish the 3 mm dose margin around the prostate. As a result the dose to the urethra is higher compared to situation A, although the dose constraints on urethra dose are not broken. Due to the hard dose constraint that aims at a PTV-PM V_{150} of ≤50%, the PTV-P V_{150} and V_{200} are lower than in situation A.

In case of situation C, all dose distributions of the three needle insertion methods fulfill the clinical criteria. Due to the seed placement margin of 3 mm, smaller clusters of the seeds (with respect to situation B) are situated nearby the urethra to accomplish the 3 mm dose margin around the prostate. As a result, the dose to the urethra is lower than in situation B.

In all situations the dose distributions of the divergent needle insertion methods are comparable with the ones of the current parallel needle insertion method.

Table 2.2. Overview of the results for the situations A, B, and C, and the three needle insertion methods of interest

	Parameter	Situation A			Situation B			Situation C			Clinical criteria
		Parallel	Single rotation point	Double rotation point	Parallel	Single rotation point	Double rotation point	Parallel	Single rotation point	Double rotation point	
PTV-PM	V_{100} (%)										
	Mean (SD)	-	-	-	94 (1)	94 (1)	95 (-)	96 (1)	96 (1)	96 (-)	≥95
	Range	-	-	-	91-96	92-95	94-96	95-97	95-97	95-97	≥95
	V_{150} (%)										
	Mean (SD)	-	-	-	50 (-)	50 (-)	50 (-)	50 (-)	50 (-)	50 (-)	≤50
	Range	-	-	-	49-50	50-50	49-50	50-50	50-50	50-50	≤50
PTV-P	V_{100} (%)										
	Mean (SD)	99 (-)	99 (-)	99 (-)	100 (-)	99 (-)	100 (-)	100 (-)	100 (-)	100 (-)	≥95
	Range	99-100	98-100	99-100	99-100	99-100	100-100	100-100	99-100	100-100	≥95
	V_{150} (%)										
	Mean (SD)	67 (-)	67 (-)	67 (-)	65 (1)	63 (1)	64 (2)	62 (1)	61 (2)	63 (1)	<70
	Range	67-67	67-67	67-67	64-67	62-65	61-66	61-63	58-63	60-65	<70
	V_{200} (%)										
	Mean (SD)	33 (-)	33 (-)	33 (-)	32 (1)	32 (1)	32 (1)	33 (-)	33 (-)	33 (-)	<35
	Range	33-33	33-33	33-33	30-34	30-33	30-33	33-33	33-33	33-33	<35
Rectum	$D_{0.1cc}$ (Gy)										
	Mean (SD)	147 (8)	147 (11)	147 (10)	171 (15)	178 (12)	166 (14)	154 (8)	155 (11)	156 (8)	<200
	Range	134-164	133-169	132-169	149-195	162-199	147-191	143-169	142-176	145-168	<200
	D_{2cc} (Gy)										
	Mean (SD)	108 (9)	108 (9)	107 (10)	120 (10)	122 (7)	119 (10)	116 (8)	117 (9)	117 (9)	<144
	Range	95-118	93-119	91-118	105-132	111-131	106-132	106-126	104-128	105-128	<144
Urethra	$D_{10\%}$ (Gy)										
	Mean (SD)	195 (4)	197 (4)	196 (6)	207 (5)	205 (7)	204 (6)	194 (3)	193 (2)	193 (2)	<216
	Range	189-203	190-202	191-207	197-213	193-214	195-216	190-199	191-196	190-195	<216
	$D_{30\%}$ (Gy)										
	Mean (SD)	187 (-)	187 (-)	187 (-)	186 (2)	186 (2)	187 (1)	186 (1)	187 (-)	187 (1)	<187
	Range	187-187	187-187	186-187	179-187	181-187	185-187	183-187	186-187	184-187	<187

Where V100 is the volume that receives at least 100% of the prescribed dose (144 Gy); D2cc is the dose to 2cc of structure; D10% is the dose to 10% of structure; Standard deviations (SD) lower than 0.5 are indicated by '(-)' in this table.

2.4. Discussion

This study, based on 10 patient MRI datasets, reveals that inverse planning of divergent I-125 implants leads to adequate prostate dose coverage for situation A, comparable to the current parallel needle insertion method. This result is in agreement with Fu *et al*. [6], who performed a planning study based on ultrasound images and an anatomical model. Fu *et al*. [6] concluded that divergent implants can achieve comparable results to parallel implants. We further elaborate the consequence of applying a 3 mm margin around the prostate as recommended by Salembier *et al*. [15]. In this case, it is difficult to

meet our clinical dose constraints when all seeds are placed inside the prostate (situation B). However, if the tips of the seeds are situated 3 mm outside the base and apex of the prostate, adequate dose coverage is achieved for all patients (situation C).

In general, the dose distributions may be further improved by reducing the diameter of the urethra catheter (to decrease the inaccessible prostate volume), by decreasing the distance between the template holes (to increase needle and consequently seed positions) and by increasing the distance between the two lateral rotation points (to minimize inaccessible prostate volume).

Also variation of dose constraints and weighting factors may lead to other optimal dose distributions, but it will not change the overall conclusion that with the three needle insertion techniques similar dose distributions are achievable.

This study quantifies the dose parameters that are routinely used in our clinic to evaluate implant quality. Salembier *et al*. [15] suggest to report additional parameters like natural dose ratio (NDR), homogeneity index (HI) and conformal index (CI). Since the NDR and HI are strongly correlated with parameters in Table 2.2, they would not alter the conclusions and it was decided not to include them in this study. The CI depends on the margin around the prostate to include possible EPE and seed placement margin rather than on different needle insertion techniques. Therefore it was not regarded as a relevant parameter for this study.

It is expected that post-implant dose distributions differ from the optimal (simulated) dose distributions, due to seed placement inaccuracy and edema development [3,13,17,20]. In future studies we want to find out which seed placement accuracy our MRI compatible robot can accomplish and what the prostate volume increase is during an I-125 implantation with our robot. Furthermore, we want to investigate whether our MRI compatible robot can reduce piercing of the penile bulb and neurovascular bundle with respect to the current parallel needle insertion method, and whether our MRI compatible robot can be used to boost dominant tumour lesions as defined by functional imaging [19].

2.5. Conclusion

In all situations the dose distributions of the divergent needle insertion methods are comparable with the ones of the current parallel needle insertion method. In case the PTV surrounds the prostate and all seeds are placed inside the prostate, both divergent needle insertion methods meet the clinical dose criteria for the prostate, urethra and rectum. However in case the PTV surrounds the prostate with a 3 mm margin, it is necessary to place the seeds partly outside the apex and base of the prostate to achieve adequate dose distributions for all patients.

References

[1] Ash D, Al-Qaisieh B, Bottomley D, Carey B, Joseph J, "The correlation between D90 and outcome for I-125 seed implant monotherapy for localised prostate cancer," *Radiother Oncol.* **79**, 185-189 (2006).

[2] Battermann JJ, Boon TA, Moerland MA, "Results of permanent prostate brachytherapy, 13 years of experience at a single institution," *Radiother Oncol.* **71**, 23-28 (2004).

[3] Bues M, Holupka EJ, Meskell P, Kaplan ID, "Effect of random seed placement error in permanent transperineal prostate seed implant," *Radiother Oncol.* **79**, 70-74 (2006).

[4] Butzbach D, Waterman FM, Dicker AP, "Can extraprostatic extension be treated by prostate brachytherapy? An analysis based on postimplant dosimetry," *Int J Radiat Oncol Biol Phys.* **51**, 1196-1199 (2001).

[5] Eshleman JS, Davis BJ, Pisansky TM, Wilson TM, Haddock MG, King BF, Darby CH, Lajoie WN, Oberg AL, "Radioactive seed migration to the chest after transperineal interstitial prostate brachytherapy: extraprostatic seed placement correlates with migration," *Int J Radiat Oncol Biol Phys.* **59**, 419-425 (2004).

[6] Fu L, Ng WS, Liu H, O'Dell W, Rubens D, Strang J, Schell MC, Brasacchio R, Liao L, Messing E, Yu Y, "Bouquet brachytherapy: feasibility and optimization of conically spaced implants," *Brachytherapy.* **4**, 59-63 (2005).

[7] Hsu IC, Lessard E, Weinberg V, Pouliot J, "Comparison of inverse planning simulated annealing and geometrical optimization for prostate high-dose-rate brachytherapy," *Brachytherapy.* **3**, 147-152 (2004).

[8] Lagerburg V, Moerland MA, van Vulpen M, Lagendijk JJW, "A new robotic needle insertion method to minimise attendant prostate motion," *Radiother Oncol.* **80**, 73-77(2006).

[9] Lessard E, Kwa SL, Pickett B, Roach M 3rd, Pouliot J, "Class solution for inversely planned permanent prostate implants to mimic an experienced dosimetrist," *Med Phys.* **33**, 2773-2282 (2006).

[10] Lessard E, Pouliot J, "Inverse planning anatomy-based dose optimization for HDR-brachytherapy of the prostate using fast simulated annealing algorithm and dedicated objective function," *Med Phys.* **28**, 773-779 (2001).

[11] Moerland MA, Wijrdeman HK, Beersma R, Bakker CJ, Battermann JJ, "Evaluation of permanent I-125 prostate implants using radiography and magnetic resonance imaging," *Int J Radiat Oncol Biol Phys.* **37**, 927-933 (1997).

[12] Pouliot J, Tremblay D, Roy J, Filice S, "Optimization of permanent 125I prostate implants using fast simulated annealing," *Int J Radiat Oncol Biol Phys.* **36**, 711-720 (1996).

[13] Reed DR, Wallner K, Ford E, Mueller A, Merrick G, Maki J, Sutlief S, Butler W, "Effect of post-implant edema on prostate brachytherapy treatment margins," *Int J Radiat Oncol Biol Phys*. **63**, 1469-1473 (2005).

[14] Rivard MJ, Coursey BM, DeWerd LA, Hanson WF, Huq MS, Ibbott GS, Mitch MG, Nath R, Williamson JF, "Update of AAPM Task Group No. 43 Report: A revised AAPM protocol for brachytherapy dose calculations," *Med Phys.* **31**, 633-674 (2004).

[15] Salembier C, Lavagnini P, Nickers P, Mangili P, Rijnders A, Polo A, Venselaar J, Hoskin P; GEC ESTRO PROBATE Group, "Tumour and target volumes in permanent prostate brachytherapy: a supplement to the ESTRO/EAU/EORTC recommendations on prostate brachytherapy," *Radiother Oncol.* **83**, 3-10 (2007).

[16] Stock RG, Stone NN, Tabert A, Iannuzzi C, DeWyngaert JK, "A dose-response study for I-125 prostate implants," *Int J Radiat Oncol Biol Phys.* **41**, 101-108 (1998).

[17] Taussky D, Austen L, Toi A, Yeung I, Williams T, Pearson S, McLean M, Pond G, Crook J, "Sequential evaluation of prostate edema after permanent seed prostate brachytherapy using CT-MRI fusion," *Int J Radiat Oncol Biol Phys.* **62**, 974-980 (2005).

[18] Van Gellekom MPR, Moerland MA, Battermann JJ, Lagendijk JJW, "MRI-guided prostate brachytherapy with single needle method-a planning study," *Radiother Oncol.* **71**, 327-332 (2004).

[19] van Lin EN, Fütterer JJ, Heijmink SW, van der Vight LP, Hoffmann AL, van Kollenburg P, Huisman HJ, Scheenen TWJ, Witjes JA, Leer JW, Barentsz JO, Visser AG, "IMRT boost dose planning on dominant intraprostatic lesions: gold marker-based three-dimensional fusion of CT with dynamic contrast-enhanced and 1H-spectroscopic MRI," *Int J Radiat Oncol Biol Phys.* **65**, 291-303 (2006).

[20] Waterman FM, Dicker AP, "Impact of postimplant edema on V(100) and D(90) in prostate brachytherapy: can implant quality be predicted on day 0?" *Int J Radiat Oncol Biol Phys.* **53**, 610-621 (2002).

This chapter has been published as:

van den Bosch MR, Moerland MA, Lagendijk JJW, Bartels LW, van den Berg CAT, "New method to monitor RF safety in MRI-guided interventions based on RF induced image artefacts," *Med Phys.* **37**, 814-821 (2010).

New method to monitor RF safety in MRI-guided interventions based on RF induced image artefacts

3

Abstract

Introduction: Serious tissue heating may occur at the tips of elongated metallic structures used in MRI-guided interventions, such as vascular guidewires, catheters, biopsy needles and brachytherapy needles. This heating is due to resonating electromagnetic radiofrequency (RF) waves along the structure. Since it is hard to predict the exact length at which resonance occurs under *in vivo* conditions, there is a need for methods to monitor this resonance behaviour. In this study we propose a method, based on the RF induced image artefacts, and demonstrate its applicability in two phantom experiments.

Methods: We developed an analytical model that describes the RF induced image artefacts as a function of the induced current in an elongated metallic structure placed parallel to the static magnetic field. It describes the total RF field as a sum of the RF fields produced by the transmit coil of the MR scanner and by the elongated metallic structure. Several spoiled Gradient Echo images with different nominal flip angle settings were acquired to map the B_1^+ field, which is a quantitative measure for the RF distortion around the structure. From this map the current was extracted by fitting the analytical model. To investigate the sensitivity of our method we performed two phantom experiments with different set-up parameters: one that mimics a brachytherapy needle insertion and one that resembles a guidewire intervention. In the first experiment, a short needle was placed centrally in the MR bore to ensure that the induced currents would be small. In the second experiment, a longer wire was placed in an off-center position to mimic a worst case scenario for the patient. In both experiments a Luxtron fiberoptic temperature sensor was positioned at the structure tip to record the temperature.

Results: In the first experiment, no significant temperature increases were measured, while the RF image artefacts and the induced currents in the needle increased with the applied insertion depth. The maximum induced current in the needle was 44 mA. Furthermore, a standing wave pattern became clearly visible for larger insertion depths. In the second experiment, significant temperature increases up to 2.4 °C in 1 min were recorded during the image

acquisitions. The maximum current value was 1.4 A. In both experiments, a proper estimation of the current in the metallic structure could be made using our analytical model.

Conclusion: We have developed a method to quantitatively determine the induced current in an elongated metallic structure from its RF distortion. This creates a powerful and sensitive method to investigate the resonant behaviour of RF waves along elongated metallic structures used for MRI-guided interventions, for example, to monitor the RF safety or to inspect the influence of coating on the resonance length. Principally, it can be applied under *in vivo* conditions and for noncylindrical metallic structures such as hip implants by taking their geometry into account.

3.1. Introduction

Elongated metallic structures used in MRI-guided interventions, such as vascular guidewires, catheters and biopsy needles, may provoke heating in surrounding tissue [1-4]. This heating is caused by the electromagnetic radiofrequency (RF) field needed to generate an MR image [1-4]. It primarily occurs at the structure tip [5] and can become a serious health hazard to patients when the RF waves can resonate along the structure. Under this condition, temperature rises over 35°C were observed in phantom studies [1,2].

At our department, we built an MR compatible robot to perform MRI-guided interventions such as biopsies and prostate brachytherapy in the nearby future [6]. It contains a tapping device to insert a titanium needle stepwise into the patient [6]. Since this needle is an elongated metallic structure, tissue heating around the needle may become an issue during MRI-guided intervention.

Yeung *et al*. [4] reported that it is theoretically possible to estimate the structure lengths or insertion depths at which resonance occurs beforehand, using the electric properties of the media surrounding this structure such as tissue and coating. In clinical practice, however, a proper estimation is generally not possible due to many factors such as heterogeneity of the tissue [2] and the unknown volume of this tissue [3,7]. Furthermore, the amount of RF heating in the tissue around a resonating structure also depends on the off-center position of the structure and its length [8]. For these reasons, there is a need for an RF safety monitoring method under *in vivo* conditions.

In this study, we demonstrate that the RF induced image artefact around the structure, provides such a method. The image artefact is the result of local signal variations due to local RF field distortions around the structure caused by an induced current in this structure [8-12]. The induced current correlates with tissue heating as reported by Nordbeck *et al*. [13]. This implies a relation between the amount of heating and severity of the RF artefact.

We first present a theoretical description of this artefact around an elongated metallic structure. Based on this description, we derive an analytical model to quantitatively determine the currents in elongated metallic structures using the RF induced image artefact. Finally, we apply it as an RF safety monitoring method for elongated metallic structures in two phantom experiments.

3.2. Methods

3.2.1. Theoretical considerations

Due to the presence of an elongated metallic structure in the MR scanner, the electromagnetic RF field produced by the transmit coil is distorted. This distorted RF field is the sum of the RF fields generated by the transmit coil of the MR scanner and by the elongated metallic structure [14]. In the following paragraph the latter field is described in more detail.

When an electromagnetic RF field of the transmit coil impinges on a cylindrical metallic structure, its free charge carriers are redistributed. The moving charge carriers constitute a current in the structure producing a magnetic field ($\vec{B}^{wire}$).

The Ampère's circuital law in integral form [15] links the total resulting magnetic field $\vec{B}^{total}$ to the current inside the wire, according to equation 3.1.

$$\oint_C \vec{B}^{total} \bullet \overrightarrow{dl} = \mu_0 \cdot \mu_r \cdot \left\{ \tilde{I} + \int_A \left(\sigma + i \cdot \omega \cdot \varepsilon_0 \cdot \varepsilon_r \right) \cdot \vec{E} \bullet \overrightarrow{dA} \right\} \qquad (3.1)$$

In this equation C represents a closed path, A is the surface enclosed by the path, μ_0 represents the permeability of vacuum, μ_r is the relative permeability of the medium, the phasor $\tilde{I}$ represents the current in the metallic structure, σ is the conductivity of the surrounding medium, ω is the angular frequency, $\vec{E}$ is the electric field perpendicular to the surface, and ε_0 and ε_r represent the permittivity of vacuum and the relative permittivity of the medium, respectively.

Close to the structure the total magnetic field is purely tangential due to the boundary condition at the metallic surface [15]. Moreover, the total electric field, which is the sum of electric fields produced by the coil and the structure, is normal to the surface of this highly conductive structure. This implies that the total electric field parallel to the structure is negligible in the proximity of this structure. As a result, Ampère's circuital law in integral form [15] can be simplified into equation 3.2 in this proximity region. It describes the tangential

magnetic field phasor ($\tilde{B}_{\varphi}$) as a function of the perpendicular distance from the structure (r), the position along this structure (z), and the current.

$$\tilde{B}_{\varphi}(r,z) = \frac{\mu_0 \cdot \mu_r \cdot \tilde{I}(z)}{2 \cdot \pi \cdot r} \tag{3.2}$$

In case $\tilde{B}_{\varphi}$ could directly be measured with MRI, we could determine the current in the structure using previous relation. In principle this is not possible, since only the left circularly polarized magnetic field, the so-called B_1^+ field, is efficient in the process of spin excitation [16]. The B_1^+ field produced by the structure ($\tilde{B}_{1+}^{wire}$) can be determined using the following equation, where the phasors $\tilde{B}_x$ and $\tilde{B}_y$ stand for the magnetic components of the RF field along the x-axis and the y-axis of the laboratory frame, respectively [17,18]:

$$\tilde{B}_{1+}^{wire}(x,y,z) = \frac{\tilde{B}_x^{wire}(x,y,z) + i \cdot \tilde{B}_y^{wire}(x,y,z)}{2} \tag{3.3}$$

Provided that the structure is placed parallel to the static magnetic field, these orthogonal magnetic field components can be derived from $\tilde{B}_{\varphi}$ using trigonometric expansion, where θ denotes the azimuth.

$$\tilde{B}_x^{wire}(x,y,z) = -\tilde{B}_{\varphi}(r,z) \cdot \sin\theta \tag{3.4}$$

$$\tilde{B}_y^{wire}(x,y,z) = \tilde{B}_{\varphi}(r,z) \cdot \cos\theta \tag{3.5}$$

Substituting these equations into equation 3.3 results in the following:

$$\tilde{B}_{1+}^{wire}(r,\theta,z) = \frac{(i \cdot cos\,\theta - sin\,\theta)}{2} \cdot \tilde{B}_{\varphi}(r,z) \tag{3.6}$$

The spins in the surrounding medium also experience the B_1^+ field produced by the transmit coil of the MR scanner ($\tilde{B}_{1+}^{coil}$) to generate an MR image. This 'background' field is defined as the applied B_1^+ field in case the induced current in the structure is zero. Using standard complex vector summation, the following equation can be derived for the total B_1^+ field ($\tilde{B}_{1+}^{total}$) around the structure, which describes the local RF field distortion.

$$\tilde{B}_{1+}^{total}(r,\theta,z) = \tilde{B}_{1+}^{coil}(r,\theta,z) + \tilde{B}_{1+}^{wire}(r,\theta,z) \tag{3.7}$$

Combining equations 3.6 and 3.7, and rewriting the phasors explicitly in their magnitudes and phases, the following equation can be obtained, where φ_0 and φ_1 represent the initial phase offsets in the rotating reference frame, and B_{1+}^{coil} and B_{1+}^{wire} the magnitude of the phasors $\tilde{B}_{1+}^{coil}$ and $\tilde{B}_{1+}^{wire}$, respectively:

$$\begin{aligned}\tilde{B}_{1+}^{total}(r,\theta,z) = {} & B_{1+}^{coil}(r,\theta,z) \cdot exp\{i \cdot \varphi_0(r,\theta,z)\} \\ & + \frac{(i \cdot cos\,\theta - sin\,\theta)}{2} \cdot B_{\varphi}(r,z) \cdot exp\{i \cdot \varphi_1(r,\theta,z)\}\end{aligned} \tag{3.8}$$

Assuming that $\tilde{B}_{1+}^{coil}$ and the phase offsets are constant along a circle close to the structure, and rewriting this equation into a real and an imaginary part, equation 3.8 becomes:

$$\begin{aligned}\tilde{B}_{1+}^{total}(r,\theta,z) = {} & \left(B_{1+}^{coil}(r,z) \cdot cos\,\varphi_0 - \frac{B_{\varphi}(r,z)}{2} \cdot sin\{\theta + \varphi_1(r,z)\} \right) \\ & + i \cdot \left(B_{1+}^{coil}(r,z) \cdot sin\,\varphi_0 + \frac{B_{\varphi}(r,z)}{2} \cdot cos\{\theta + \varphi_1(r,z)\} \right)\end{aligned} \tag{3.9}$$

The magnitude of the phasor $\tilde{B}_{1+}^{total}$ (indicated as B_{1+}^{total}) can be derived from equation 3.9, where $\theta_0(r,z) = \varphi_0(r,z) - \varphi_1(r,z)$.

$$B_{1+}^{total}(r,\theta,z) = \left(\frac{\{B_\varphi(r,z)\}^2}{4} + \{B_{1+}^{coil}(r,z)\}^2 - B_\varphi(r,z) \cdot B_{1+}^{coil}(r,z) \cdot \sin(\theta - \theta_0(r,z)) \right)^{1/2} \quad (3.10)$$

The latter equation describes the magnitude of the total B_1^+ field as a function of r, θ, and z. It can be fit to the measured B_{1+}^{total} data at a certain radius from the structure to extract B_φ. The output parameter B_φ can be converted into the magnitude of the current in the structure applying the simplified Ampère's circuital law (equation 3.2). The obtained current value represents the magnitude of the current phasor, also indicated as the peak value of the current. This process can be repeated for several radial positions to better estimate the current.

3.2.2. Experiment

To investigate the sensitivity of our method we performed two phantom experiments with different set-up parameters: one that mimics a prostate brachytherapy implantation performed by the robot and one that resembles a metallic guidewire intervention. In the first experiment, a short needle was placed centrally in the MR bore to ensure that the induced currents would be small. In the second experiment, a longer wire was placed in an off-center position to mimic a worst case scenario for the patient.

In both experiments several spoiled Gradient Echo (GE) images with different nominal flip angle (θ_{nom}) settings were acquired to map the B_1^+ distortion around the structure, and to estimate the current in it.

3.2.2.1. Experimental set-up

In the first experiment, a titanium needle including stylet (L = 20 cm, d = 1.3 mm) was inserted centrally into a phantom to depths of 5, 10, 13 and 16 cm (see Figure 3.1a). The phantom was situated in the center of a SENSE-Tx/Rx head coil placed centrally in the MR bore of a 3 T MR scanner (Achieva, Philips Medical Systems, Best, The Netherlands). It consisted of a plastic cylinder (L = 19 cm, d = 10 cm) filled with NaCl doped gelatin (3 g NaCl per liter gelatin) to simulate average conductive biological tissue surrounding the needle. The needle was fixated by the gelatin and situated parallel to the longitudinal axis of the scanner. A fiberoptic temperature sensor (Luxtron, Santa Clara, California, USA) was positioned near the tip of the needle to record the temperature in the surrounding medium.

In the second experiment, a copper wire (L = 80 cm, d = 1.7 mm) was centrally inserted to a depth of 34 cm into a PVC cylinder (L = 83 cm, d = 12 cm). The cylinder was filled with tap water that was doped with $MnCl_2$ (19.2 mg $MnCl_2 \cdot 4H_20$ per liter) to reduce the T_1 value. The phantom was placed in a 10 cm off-center position in the body coil of the 3 T MR scanner. The wire was surrounded by a perforated PVC tube (L = 83, d = 1.3 cm) to guide the wire during insertion. The tip of the wire was placed in a small 2 cc plastic tube that was filled with saline (9 g NaCL per liter H_20) to simulate the presence of high conductive biological tissue directly near the tip. Furthermore the fiberoptic temperature sensor was positioned near the wire tip to control whether a high temperature increase was achieved in the surrounding medium.

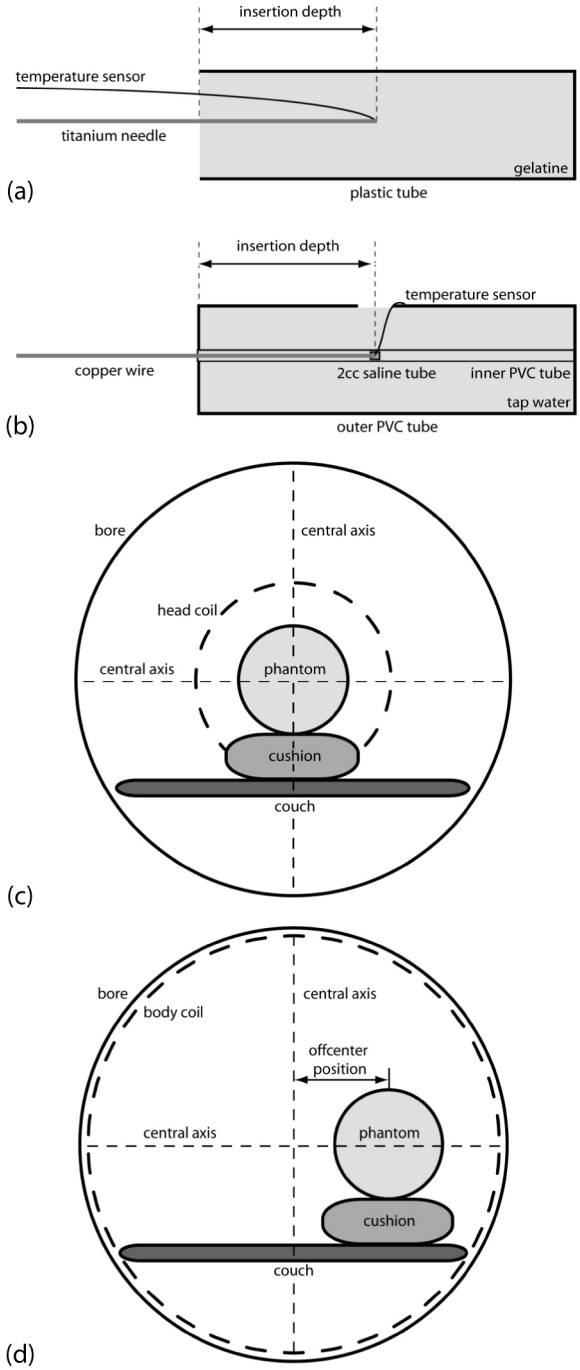

Figure 3.1. *Schematic overview of the phantoms used in the first experiment (a) and in the second experiment (b), and their positions in the MR scanner (c,d).*

3.2.2.2. B_1^+ mapping

The magnitude of the B_{1+}^{total} field can be mapped using several GE images with different θ_{nom} settings [19,20]. The acquisition times of these mapping techniques are long due to the relatively long repetition time (TR) of usually five times the largest T_1 value needed to reduce the saturation effects. In this study we used a B_1^+ mapping technique based on the signal equation for a spoiled GE sequence [16]. In addition to multiple GE images with different θ_{nom} settings, we acquired a separate T_1 map to compensate for the saturation effects. In this way the total acquisition time was strongly reduced.

For the first experiment we used the following multi-slice (MS) protocol to acquire several GE images with different θ_{nom} settings: TR = 300 ms, echo time (TE) = 2.1-2.3 ms, acquisition time = 82-109 s, field of view (FOV) = 120 x 120 x 209 mm^3, acquisition matrix = 120 x 120, slice thickness = 5 mm, slice gap = 1 mm, NSA = 3-4, local specific absorption rate (SAR) = 0.0-2.4 W/kg, θ_{nom} = 5, 25, 50, 75°. The main parameters of the MS protocol of the second experiment were: TR = 300 ms, TE = 2.1-3.2 ms, acquisition time = 136-273 s, FOV = 150 x 150 x 195 mm^3, acquisition matrix = 152 x 151, slice thickness = 5 mm, slice gap = 5 mm, NSA = 4, local SAR = 0.0-9.4 W/kg, θ_{nom} = 2, 4, 6, 10, 25, 50, 80, 110, and 150°.

The T_1 values of the phantoms were determined in a region away from the titanium needle or copper wire. For this purpose images were acquired using an inverse recovery (IR) protocol with different TR and IR delay. For the first experiment we used a protocol with: IR delay/TR=50/300, 200/400, 400/600, 800/1000 and 1400/1600 ms, TE = 14 ms, acquisition time = 21-107 s, FOV=150/150/4 mm^3, acquisition matrix =64 x 32, NSA = 2. In the second experiment only the FOV, acquisition matrix and acquisition time were different: FOV = 140 x 140 x 4 mm^3, acquisition matrix=64 x 64 and acquisition time = 42-214 s.

The mean T_1 value of a selected region of interest was determined (see Figure 3.2a) and used to compensate for the saturation effects.

The signal equation for the spoiled GE sequence (see equation 3.11) was fit on voxel basis to the multiflip angle data, where SI is the signal intensity, λ_{trans} is

the transmit sensitivity, and C represents a spatial varying factor that includes parameters as local spin density, local receive coil sensitivity, and T_2 effects [10,16].

$$SI(x,y,z) = C(x,y,z) \cdot \frac{sin(\lambda_{trans}(x,y,z) \cdot \theta_{nom}) \cdot (1 - e^{-TR/T_1})}{1 - e^{-TR/T_1} \cdot cos(\lambda_{trans}(x,y,z) \cdot \theta_{nom})} \quad (3.11)$$

This equation has two output parameters: C and λ_{trans}. The latter parameter is a relative measure for the RF field distortion caused by the metallic structure. To deal with the high dynamic range of the RF field distortion around the wire different flip angle combinations of at least four GE images were applied. Dataset combinations with high θ_{nom} are sensitive to low λ_{trans} and vice versa. By selecting the fits with the highest goodness of fit, an optimal λ_{trans} map was generated. A median filter with a 3x3 kernel was applied to remove noise.

The relative measure λ_{trans} was converted into an absolute B_1^+ field by multiplying it with a nominal B_1^+ magnitude (B_{1+}^{nom}) of 3.3 µT corresponding to a 50 degree flip angle for a rectangular pulse of 1 ms, according to equations 3.12 and 3.13 [16,18]. Equation 3.12 describes the nominal flip angle as a function of the gyromagnetic ratio (γ), the nominal magnitude of the B_1^+ field, and the duration of the rectangular RF pulse (τ) .

$$\theta_{nom} = \gamma \cdot B_{1+}^{nom} \cdot \tau \quad (3.12)$$

$$B_{1+}^{total}(r,\theta,z) = \lambda_{trans}(r,\theta,z) \cdot B_{1+}^{nom} \quad (3.13)$$

After the calculation of the B_{1+}^{total} map, the parameter B_φ was derived from this field map using the fit equation (see equation 3.10). Then the magnitude of the current was determined according to the simplified Ampère's circuital law (see equation 3.2), where the permeability constant of the medium was set to that of water: μ_r = 0.999991 [8]. All currents in this study are reported for these RF pulse settings.

3.3. Results

During the scans in the first experiment (needle insertion around isocenter) no significant temperature increase was recorded. Figures 3.2a and 3.2b show the acquired T_1 map and one of the obtained GE images, respectively. The mean T_1 value of the region of interest equalled 1133 ms (SD = 85 ms). A B_{1+}^{total} map was generated for each insertion depth (see Figure 3.2c). Due to the induced current in the wire the B_{1+}^{total} map is highly inhomogeneous around the wire. The bright spot indicates an amplification of the field, while the dark area represents a reduction. The magnification ranged from 0.7 to 1.5.

A typical example of a measured angular B_{1+}^{total} profile is shown in Figure 3.3a together with a fit according to equation 3.10. The agreement between the fit and the B_{1+}^{total} profile indicates the validity of this fit equation. This fit procedure can be repeated for several radial positions, resulting in a plot of the fit output parameters B_{φ} and B_{1+}^{coil} versus the radial position. Since the fit equation is a second order polynomial having symmetrical variables, it has two solutions that are mirrored with respect to each other (see Figures 3.3b and 3.3c). They are related by a factor of two.

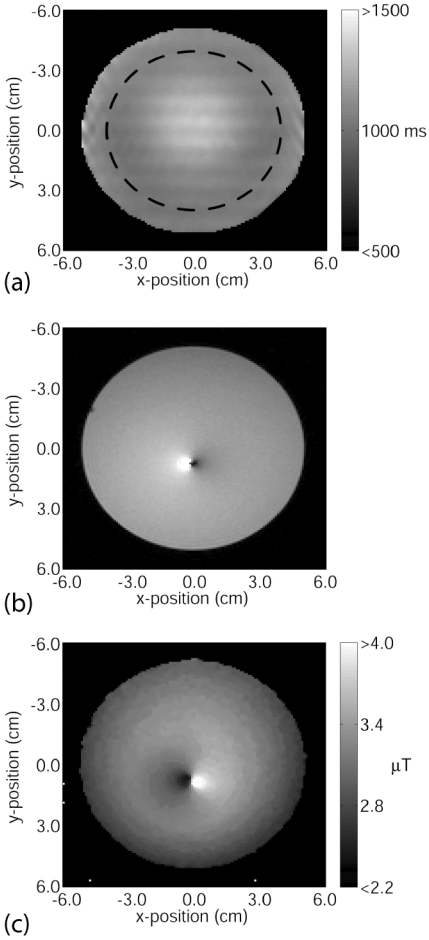

Figure 3.2. *(a) T_1 map of a transverse slice that did not intersect the needle. The dashed line encloses the region of interest used to calculate the mean T_1 value of the medium. (b) Transverse GE image of the phantom with the needle at a depth of 16 cm acquired using a θ_{nom} of 75°. (c) Derived B_{1+}^{total} map of an identical slice of the phantom.*

According to the previously described physical principles, the solution of interest should exhibit a flat B_{l+}^{coil} curve and a B_{φ} curve that is inverse proportional to the radius. Therefore the solution illustrated in Figure 3.3b is the solution of interest.

Figure 3.3d shows the current calculated from the B_{φ} values at different radii in the case of the maximum needle insertion depth of 16 cm. Currents in the needle at positions 2, 11 and 14 cm from the insertion point are depicted in this figure. The curve at 11 cm from the insertion point is representative for all other curves, expect the ones close to the insertion point or tip of the needle. This typical curve is approximately flat for radii ≥7 mm. The curves at positions 2 and 14 cm from the insertion point represent the obtained curves close to the insertion point and close to the needle tip, respectively. These curves are approximately flat between 7 and 10 mm, but decrease or increase for larger radii.

By determining the mean current value of a radius interval between 7 and 10 mm for each transverse plane, the current profile along the needle can be depicted for each insertion depth (see Figure 3.3e). This figure shows that the induced current in the needle increases with the insertion depth. The maximum current value is 44 mA. Also the standing wave pattern with one crest becomes more clear for larger insertion depths.

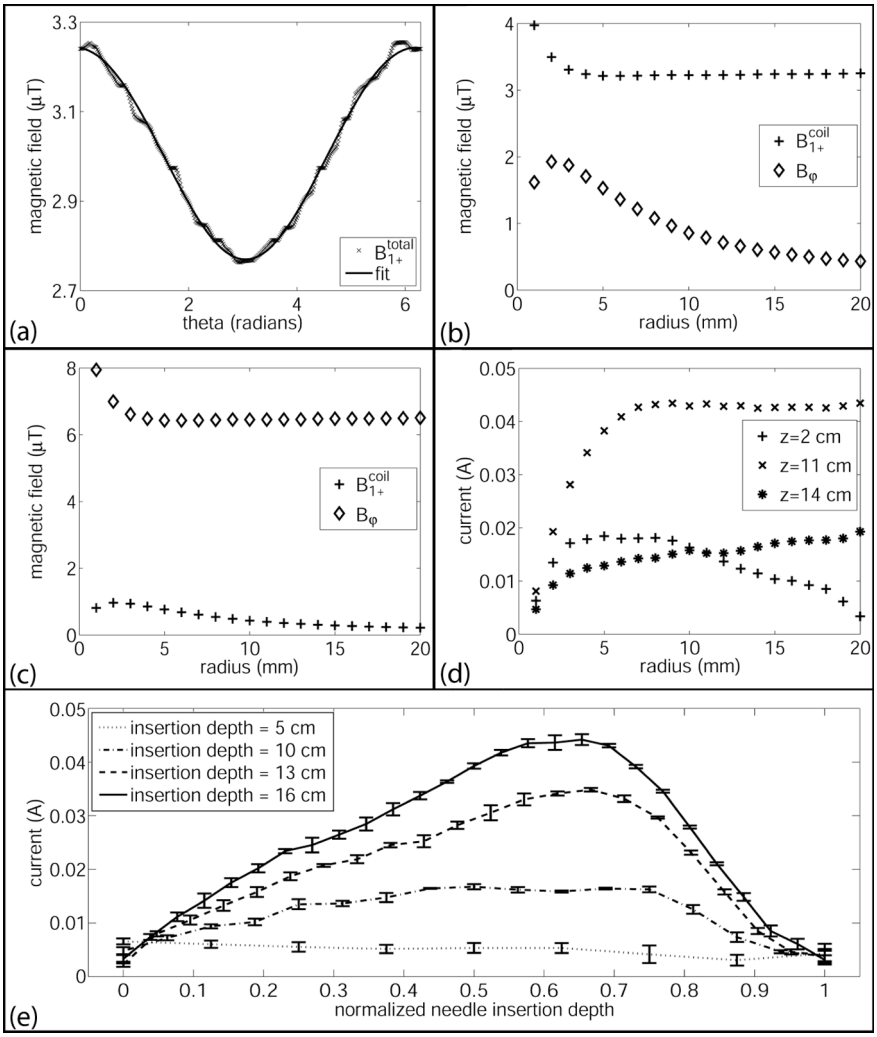

Figure 3.3. *(a)* B_{1+}^{total} *profile at a distance of 10 mm from the needle. (b) One of the two fit solutions. This solution is the one of interest as described in the text. (c) Other fit solution, which is a mirrored solution of the previous solution. (d) Current values calculated from the* B_{1+}^{total} *profile at different radii in specific transverse planes at position z from the insertion point. (e) Current profiles along the needle for all inspected insertion depths. The error bar represents the standard deviation. Position zero and position one are at the insertion point and needle tip, respectively.*

Significant temperature increases up to 2.4 °C in 1 min were recorded during the image acquisitions in the second experiment (off-center wire insertion). Figures 3.4a and 3.4b show the acquired T_1 map and one of the obtained GE

images, respectively. The mean T_1 value of the selected region of interest in the obtained T_1 map equalled 720 ms (SD = 63 ms). The generated total B_{1+}^{total} map was more inhomogeneous with respect to the one of the first experiment (see Figure 3.4c). The magnification ranged from 0.0 to >17 due to the high current induced in the wire.

Figure 3.5a shows current values generated from B_{1+}^{total} profiles at several radii for different transverse plane. These curves are representative for the other obtained curves, even the ones close to the insertion point, and demonstrate that the calculated current values are approximately constant for radii between 7 and 15 mm.

By determining the mean current value of this interval for each transverse plane, the current profile along the wire can be calculated (see Figure 3.5b). In this figure a wave pattern with two crests can be distinguished. This implies a higher resonance mode with respect to the first experiment. The maximum current value equals 1.4 A and is much higher than the induced current values of the first experiment.

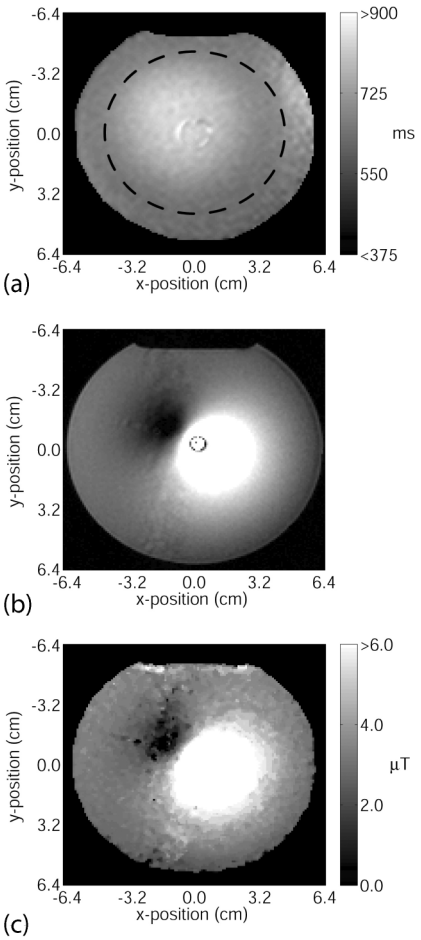

Figure 3.4. *(a) T_1 map of a transverse slice that did not intersect the wire. The dashed line encloses the region of interest used to calculate the mean T_1 value of the medium. (b) Transverse GE image of the phantom acquired with a θ_{nom} of 25°. (c) Derived B_{1+}^{total} map of an identical slice of the phantom.*

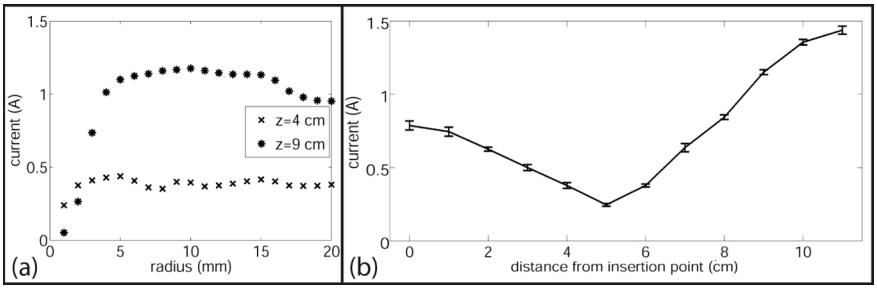

Figure 3.5. *Current values calculated from the B_{1+}^{total} profile at different radii in specific transverse planes at position z from the insertion point. (b) Current profiles along the wire for the inspected insertion depth (d=34cm). The error bar represents the standard deviation. Since the middle of the wire was placed halfway the longitudinal axis of the MR scanner to create the biggest potential difference at the wire tips and consequently obtain the highest tissue heating, only a limited part of the wire could be scanned.*

3.4. Discussion

This study reveals that it is possible to quantify the current in a metallic structure using the total B_1^+ field derived from the RF induced artefact in several GE images. The agreement between the fit that is based on our analytical model and the measured B_{1+}^{total} profile at specific radii (see Figure 3.3a) indicates that the assumptions made are valid: in the proximity of the structure the magnetic field produced by an elongated metallic structure is purely tangential, the quadrature field is constant along a circle centered on this structure, and the initial phase offset between these two fields in the rotating frame of reference is also constant along this circle. Independent measurement of the RF induced currents with some type of sensor are necessary for further validation of our method and may be possible in near future with recently developed sensors [13,21].

We demonstrated the usefulness of our method for two situations: needle insertion around isocenter and an off-center wire insertion. The results of the first situation exhibit an amplitude increase for higher insertion depths (see Figure 3.3e). Furthermore, a standing wave pattern became clearly visible for larger insertion depths. Although an induced current with a maximum amplitude of 44 mA in the needle could be determined, no significant temperature increase was recorded at the needle tip. This suggests that our method is a very sensitive method to investigate resonance behavior. The

induced current in the second situation was much higher (factor 32) than in the first experiment. Main causes are the off-center position of the wire and the larger length of the wire [8]. They both result in a higher induced current due to an increased potential difference at the structure tips. Furthermore the amplitude of the node was unequal to zero. This might be due to the averaging in the z-direction or the difference in wave amplitudes of the underlying waves that propagate in the positive and negative direction. This amplitude variation is the result of differences in reflection. One wave reflects at the tip and one at the medium-air interface.

As shown in Figures 3.3d and 3.5a we were able to obtain reliable values of the induced current in the elongated metallic structures from B_{1+}^{total} profiles at ≥7 mm from the structure. The susceptibility difference between titanium (180 ppm), copper (-9.8 ppm) and water (-9.0 ppm) may result in a susceptibility artefact around the structures [22], causing an improper estimation of the current in the structures from B_{1+}^{total} profiles at radii smaller than 7 mm. However, since the structures were placed parallel to the static magnetic field, the susceptibility artefact is confined to the tip of these elongated structures. Therefore we think the susceptibility artefact is not an issue in our experiments. More likely, the improper estimation of the current in the structures from B_{1+}^{total} profiles at these small radii is due to the relatively low number of sample points. Furthermore, the B_{1+}^{total} gradient inside one acquisition voxel is high close to the structure. In this case the measured B_{1+}^{total} value, which is an average B_{1+}^{total} value over the entire voxel, may not be representative for the local B_{1+}^{total} value at the corresponding voxel center. Moreover, the applied median filter does not only remove the noise, but also smoothes the data resulting in an under estimation of the B_{1+}^{total} value close to the structure.

Figure 3.3d shows that the current determined from the B_{1+}^{total} profiles in the transverse planes at positions 2 and 14 cm from the insertion point, decreases or increases for large radii, respectively. This can be explained by the contribution of the electric field parallel to the needle, according to the Ampère's circuital law [15]. Namely, the electric field is no longer perpendicular to the surface of a conductor for large radii. This effect increases in the proximity of the tip. Since all acquired transverse images of the second experiment were located relatively close to the middle of the wire, the

contribution of the electric field was less noticeable with respect to the first experiment as is depicted in Figure 3.5a.

Taking the calculated current curves in all acquired transverse slices of both experiments into account, we propose a proper estimation of the current in a metallic structure can generally be made using the current values calculated from the B_{1+}^{total} profiles at a radius between 7 and 10 mm from this structure. The relatively small interval implies to apply the fit equation to an angular B_{1+}^{total} profile at specific radius as in this study, rather than to a radial B_{1+}^{total} profile at a specific angle.

Our method can be applied to estimate the RF safety of metallic structures in (human equivalent) phantoms, for example to inspect the influence of materials or coating on the resonance length. In this study we made use of two cylindrical metallic structures (a needle and a wire) placed parallel to the static magnetic field, but we believe our method will also be suitable for structures placed under an angle keeping the planes, in which the angular B_1^+ profiles are selected, perpendicular to the structure. In these planes the Ampère's circuital law is still applicable. Probably, the B_1^+ vector needs to be corrected by taking the angle between the structure and the static magnetic field into account, but we have to investigate this in the future. Furthermore, signal correction for the susceptibility artefact might be needed, because the artefact will no longer be confined to the tip of the structure. This might also imply that a B_1^+ mapping technique that can compensate for off-resonances caused by the difference in susceptibility is necessary. Recently, such a technique was described by Brunner *et al*. [23]. Also for noncylindrical metallic structures such as hip implants our method is applicable, by taking their geometry into account.

Principally, our method can also be applied for heterogeneous tissues and thus under *in vivo* conditions, since it is based on the B_1^+ distortion and not on the induced artefact in a single image. Although the applied B_1^+ mapping technique is simple, accurate and robust [16], it is still time consuming due to the high number of θ_{nom} settings needed to deal with the high dynamic range of the RF field distortion and the acquisition of a T_1 map. For *in vivo* B_1^+ mapping, faster techniques have been developed, which are also capable of dealing with high RF distortions, within SAR limits [23-27].

We demonstrate that our method is suitable for monitoring the resonance behavior of RF waves along metallic structures placed parallel to the longitudinal axis of the MR bore. As the RF safety is dominated by tissue heating at the structure tip, we want to use the current profile to estimate the charge build-up and consequently the electric field intensity at this location. The electric field intensity can be converted into the SAR, which is a measure for the tissue heating [4].

3.5. Conclusion

We have developed a method to quantitatively determine the induced current in a metallic structure from its RF distortion, even for high distortions. This creates a powerful method to investigate the resonant behavior of RF waves along metallic structures used for MRI-guided interventions. In principle, the methodology is also applicable for *in vivo* purposes. The next step is to use these current profiles for the determination of the electric field intensity at the structure tip, from which the local tissue heating can be estimated.

References

[1] Dempsey MF, Condon B, Hadley DM, "Investigation of the factors responsible for burns during MRI," *J Magn Reson Imaging.* **13**, 627-631 (2001).

[2] Konings MK, Bartels LW, Smits HF, Bakker CJG, "Heating around intravascular guidewires by resonating RF waves," *J Magn Reson Imaging.* **12**, 79-85 (2000).

[3] Yeung CJ, Karmarkar P, McVeigh ER, "Minimizing RF heating of conducting wires in MRI," *Magn Reson Med.* **58**, 1028-1034 (2007).

[4] Yeung CJ, Susil RC, Atalar E, "RF safety of wires in interventional MRI: using a safety index," *Magn Reson Med.* **47**, 187-193 (2002).

[5] Park SM, Kamondetdacha R, Nyenhuis JA, "Calculation of MRI-induced heating of an implanted medical lead wire with an electric field transfer function," *J Magn Reson Imaging.* **26**, 1278-1285 (2007).

[6] Lagerburg V, Moerland MA, van Vulpen M, Lagendijk JJW, "A new robotic needle insertion method to minimise attendant prostate motion," *Radiother Oncol.* **80**, 73-77 (2006).

[7] Pictet J, Meuli R, Wicky S, van der Klink JJ, "Radiofrequency heating effects around resonant lengths of wire in MRI," *Phys Med Biol.* **47**, 2973-2985 (2002).

[8] Nitz WR, Oppelt A, Renz W, Manke C, Lenhart M, Link J, "On the heating of linear conductive structures as guide wires and catheters in interventional MRI," *J Magn Reson Imaging.* **13**, 105-114 (2001).

[9] Graf H, Lauer UA, Berger A, Schick F, "RF artifacts caused by metallic implants or structures which get more prominent at 3 T: an in vitro study," *Magn Reson Imaging.* **23**, 493-499 (2005).

[10] Bartels LW, Bakker CJG, Viergever MA, "Improved lumen visualization in metallic vascular implants by reducing RF artifacts," *Magn Reson Med.* **47**, 171-180 (2002).

[11] Park SM, Ph.D. Thesis, *MRI safety: Radiofrequency field induced heating of implanted medical devices*, (Purdue University, West Lafayette, 2006).

[12] Park SM, Sakaie K, Tkach J, Rezai AR, Nyenhuis JA, "Determination of induced currents in an implanted lead with MRI," *oral presentation at the ISMRM workshop on MRI safety: update, practical information, and future implications*, Virginia, USA, 2005.

[13] Nordbeck P, Weiss I, Ehses P, Ritter O, Warmuth M, Fidler F, Herold V, Jakob PM, Ladd ME, Quick HH, Bauer WR. "Measuring RF-induced currents inside implants: Impact of device configuration on MRI safety of cardiac pacemaker leads," *Magn Reson Med.* **61**, 570-578, (2009).

[14] Graf H, Steidle G, Martirosian P, Lauer UA, Schick F, "Effects on MRI due to altered rf polarization near conductive implants or instruments," *Med Phys.* **33**, 124-127 (2006).

[15] Lorrain P, Corson DR, Lorrain F, *Electromagnetic fields and waves*, 3rd ed. (H. Freeman and Company, New York, 1988).

[16] van den Berg CAT, Bartels LW, van den Bergen B, Kroeze H, de Leeuw AAC, van de Kamer JB, Lagendijk JJW, "The use of MR B1+ imaging for validation of FDTD electromagnetic simulations of human anatomies," *Phys Med Biol.* **51**, 4735-4746 (2006).

[17] Hoult DI, "The principle of reciprocity in signal strength calculations – a mathematical guide," *Concepts in Magnetic Resonance.* **12**, 173-187 (2000).

[18] Haacke EM, Brown RW, Thompson MR, Venkatesan R, *Magnetic Resonance Imaging – physical principles and sequence design*, 1st ed. (John Wiley & Sons, New York, 1999).

[19] Barker GJ, Simmons A, Arridge SR, Tofts PS, "A simple method for investigating the effects of non-uniformity of radiofrequency transmission and radiofrequency reception in MRI," *Br J Radiol.* **71**, 59-67 (1998).

[20] Alecci M, Collins CM, Smith MB, Jezzard P, "Radio frequency magnetic field mapping of a 3 Tesla birdcage coil: experimental and theoretical dependence on sample properties," *Magn Reson Med.* **46**, 379-385 (2001).

[21] Zanchi MG, Venook R, Pauly JM, Scott G, "An optically-coupled system for quantitative monitoring of MRI-induced RF currents into long conductors," *oral presentation at the ISMRM 16th scientific meeting & exhibition*, Toronto, Canada, 2008.

[22] Lagerburg V, Moerland MA, Seppenwoolde JH, Lagendijk JJW, "Simulation of the artefact of an iodine seed placed at the needle tip in MRI-guided prostate brachytherapy," *Phys Med Biol.* **53**, N59-67 (2008).

[23] Brunner DO, Pruessmann KP, "B1+ interferometry for the calibration of RF transmitter arrays," *Magn Reson Med.* **61**, 1480-1488 (2009).

[24] Cunningham CH, Pauly JM, Nayak HS, "Saturated double-angle method for rapid B1+ mapping," *Magn Reson Med.* **55**, 1326-1333 (2006).

[25] Dowell NG, Tofts PS, "Fast, accurate, and precise mapping of the RF field in vivo using the 180 degrees signal null," *Magn Reson Med.* **58**, 622-630 (2007).

[26] Yarnykh VL, "Actual flip-angle imaging in the pulsed steady state: a method for rapid three-dimensional mapping of the transmitted radiofrequency field," *Magn Reson Med.* **57**, 192-200 (2007).

[27] Nehrke K, "On the steady-state properties of actual flip angle imaging (AFI)," *Magn Reson Med.* **61**, 84-92 (2009).

This chapter has been submitted as:

van den Bosch MR, Moerland MA, de Leeuw H, van Schelven LJ, Dijkstra PT, van den Berg CAT, van Vulpen M, Lagendijk JJW, "The development and quality assurance of robotic devices for MRI-guided brachytherapy and tumour biopsy," *Phys Med Biol.* (2011).

The development and quality assurance of robotic devices for MRI-guided brachytherapy and tumour biopsy

4

Abstract

This study discusses the clinical introduction of MRI-guided robotic devices for MRI-guided needle interventions, such as brachytherapy and tumour biopsy. It provides background information and insights on how to deal with the MRI-related challenges, such as accessibility, MR compatibility, needle placement accuracy and safety, before the devices can be safely applied on patients. The University Medical Center Utrecht (UMCU) robot serves as illustration.

4.1. Introduction

Magnetic resonance imaging (MRI) is valuable in soft-tissue interventions over other image modalities, such as ultrasound and CT, due to its superior soft tissue contrast [1-4]. It establishes better visualization, localization and delineation of the target and surrounding critical structures at the moment of intervention [1-6]. However, accessibility is restricted inside MR systems.

At several institutes, robotic devices have been developed to overcome this limitation and to perform real-time MRI-guided needle interventions [7-13]. Although the principles of these robotic devices are different, they have common challenges to face before they can be safely applied on patients. MRI-related challenges concern: accessibility, MR compatibility, needle placement accuracy and safety.

This study discusses these challenges. The University Medical Center Utrecht (UMCU) robot serves as illustration [13].

4.2. Patient accessibility

For the design of the robot, the available space inside an MR scanner is important. The closed bore and the open MR scanner have both their own strengths and limitations.

Due to the gap between the two poles of an open MR scanner, the patient is accessible from (almost) any angle. This gap can either be in horizontal [14] or vertical direction [15]. Such an open scanner has two drawbacks. The first is the direction of the static magnetic field. This field is oriented vertically for a horizontal gap and horizontally for a vertical gap. Since the intervention needle will generally be positioned perpendicular to this field, the susceptibility artefact caused by the needle will be present along the entire needle in the MR image [6,16-18]. Another drawback is the lower magnetic field strengths that are available for these systems compared to closed bore MR scanners, resulting in lower image quality [19].

In a closed bore MR scanner the direction of the static magnetic field is oriented along the longitudinal axis of the MR bore, making it more logical to align the

intervention needle with this field. As a result, the susceptibility artefact caused by the needle is confined to the tip of the needle in the MR image [16-18].

The higher magnetic field strength results in a better signal-to-noise ratio (SNR) and consequently image quality [19]. However, there are also disadvantages of using high field strengths for robotic interventions. Static field distortions and signal intensity artefacts caused by the robot and the needle become more prominent at higher field strengths [3,16,19]. Also, the wavelength of the electromagnetic radiofrequency (RF) waves that are needed to generate an MR image become shorter, which might increase the risk of serious tissue heating around the intervention needle tip due to resonating RF waves along the needle [19-21]. At very high field strengths, the shorter RF waves can lead to destructive interferences of superimposed RF waves inside the human body, resulting in local regions of signal losses [19,22]. The tissue RF power deposition increases with higher field strengths, which might result in heat sensations by the patient [19].

Moreover, magnetic forces on metallic devices generally correlate with the magnetic field (gradient) strength of the MR scanner [23-25].

The UMCU robot will be primarily used for transperineal prostate interventions. We believe that a 1.5 T closed bore MR scanner provides sufficient SNR for adequate image quality and its field orientation is beneficial to place the needle along the static magnetic field. Therefore, we want to perform MRI-guided prostate interventions in such a scanner.

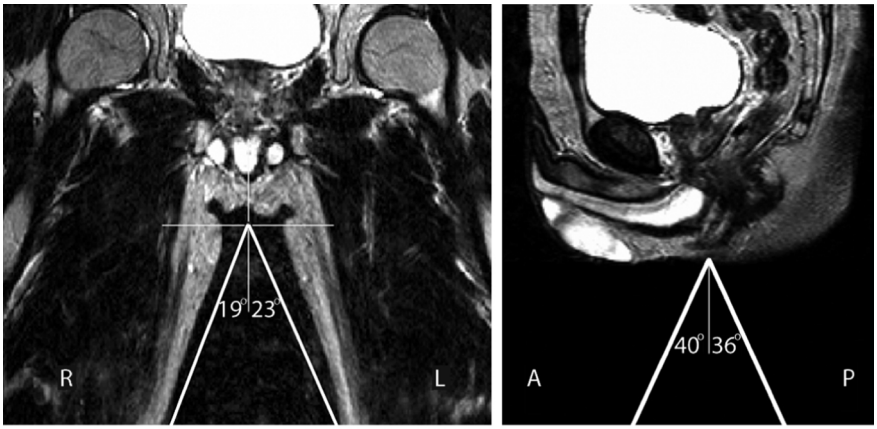

Figure 4.1. *Available space for the UMCU robot when the rotation point is placed just underneath the perineum skin of a typical patient (a) in the coronal plane, (b) in the sagital plane.*

To investigate the available space for prostate interventions, we performed a planning study on 5 patients [26]. These patients were placed in the intended patient position (supine position with legs spread) inside a 1.5 T closed bore MR scanner (Gyroscan, Philips Healthcare, Best, The Netherlands) and a T2 weighted turbo SE scan was acquired. In these scans, the space between patient's legs was estimated and the accessibility to the prostate was inspected (see Figure 4.1). For all patients, the entire prostate gland could be reached using a divergent needle insertion method [26]. The UMCU robot was designed for the available space.

4.3. MR compatibility of the robot

A robot that performs well outside a magnetic field may cause risks when used in a magnetic field. There are several difficulties, namely: ferromagnetism, induced currents, and signal intensity distortions in the MR image.

4.3.1. Ferromagnetism

Ferromagnetic structures may become dangerous projectiles when taken into the scanning room. They tend to move due to magnetic forces in regions where a spatial magnetic field gradient is present [23,24]. The force increases with the magnetic susceptibility of the material and the magnitude of the gradient. In general, the spatial gradients are maximal near the magnet portal [24]. When placed in a magnetic field, the structure inclines to rotate as a result of a magnetic torque [23,24].

In addition, ferromagnetic structures greatly distort the field uniformity inside the magnet destroying image quality. The use of ferromagnetic materials is generally prohibited in all MR scanners types. All robotic components should therefore be tested for non-ferromagnetism, before entering the MR scanning room.

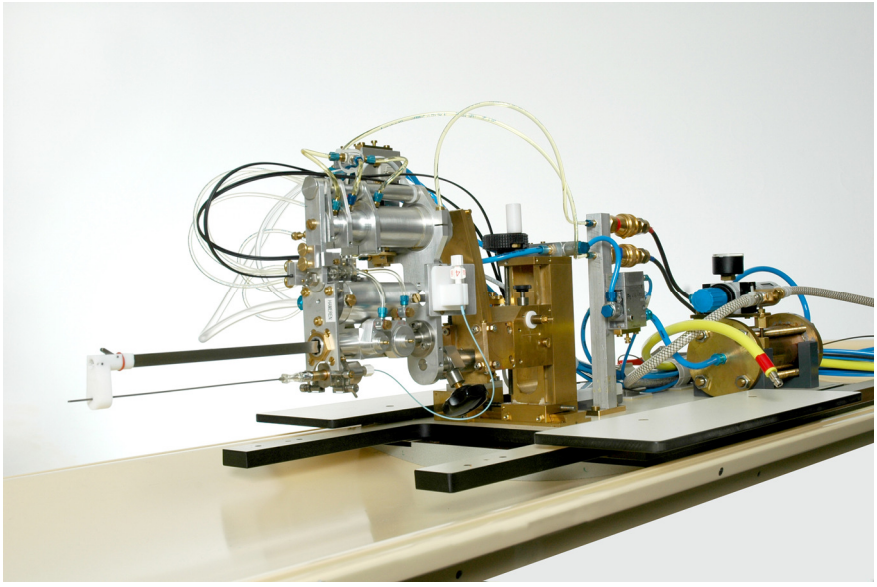

Figure 4.2. *The UMCU robot.*

The UMCU robot is pneumatically and hydraulically driven and consists of polymers and non-ferromagnetic materials as brass, copper, titanium and aluminium (see Figure 4.2). All components of the UMCU robot were tested for non-ferromagnetism by holding a low-field hand magnet close to them, before entering the MR scanning room. No forces were measured on the robotic components of the UMCU robot by the low-field hand magnet, except on a small potentiometer. Nevertheless, we use this sensor to monitor the displacement of the buffer stop [13] that limits the maximal needle insertion depth per tap, as a backup to the MR imaging (see paragraph 4.5.1). The small potentiometer was strongly attached to the massive robot. No forces were observed when sliding the robot into the 1.5 T MR scanner.

4.3.2. Induced currents

Eddy currents are evoked by a change in magnetic flux through conducting pathways and produce magnetic fields counteracting the original change in magnetic field [24,27,28]. The change in magnetic flux can be caused by time-varying magnetic fields, such as during gradient switching, resulting in image

artefacts (see further on) and vibrations of the concerning conductive component [28]. Moreover, eddy currents are induced when a conductive component moves through a static magnetic field gradient or rotates in a static magnetic field, resulting in a resistance to motion [24,27]. This may hamper the performance of a robotic device.

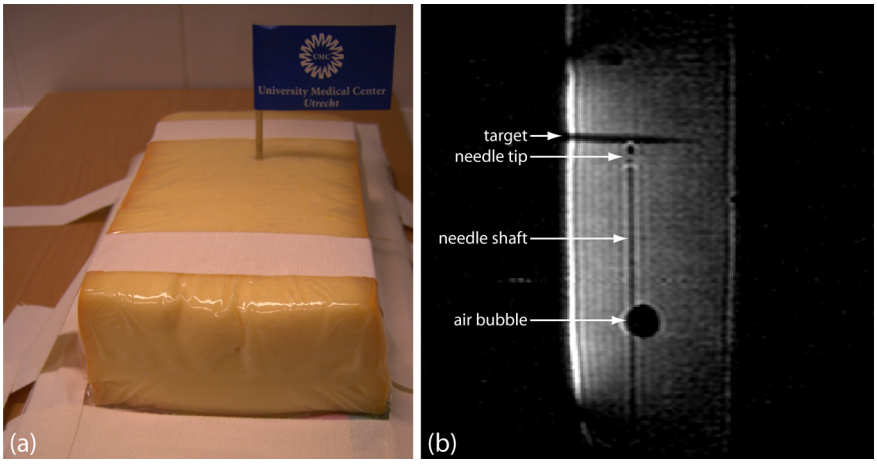

Figure 4.3. *(a) Cheese phantom with wooden stick, (b) Turbo SE scan of cheese phantom with the tip of the robotic needle against the wooden stick.*

Since the UMCU robot is primarily made of non-ferromagnetic but conductive metals, there is a risk of degraded system performance in the MR scanner. Precautions are taken to prevent or to minimize the area of loops and to electrically isolate critical structures. To test the UMCU robot, the robot was placed on the MR table outside a 1.5 T closed bore MR scanner (Achieva, Philips Healthcare, Best, The Netherlands). The needle was tapped into a piece of Dutch cheese with a thin wooden stick as target (see Figure 4.3). Afterwards, the robot was placed inside the scanner and the experiment was repeated. The performance of the robot inside and outside the magnetic field was identical. In both cases the needle insertion speed was 0.5 m/s and the target could be reached in the predefined number of steps. The potentiometer of the UMCU robot also functioned well inside the 1.5 T magnetic field, except during image acquisition, due to evoked currents. The recorded data contained spurious values, which could easily be removed using a median filter with a kernel size of 10 ms. The vibrations of the UMCU robot during image acquisitions were negligible.

4.3.3. Signal intensity distortions in the MR image

A material with a susceptibility other than its surrounding medium (for example human tissue) locally distorts the static magnetic field, leading to intra-voxel dephasing of the spins [16,29]. The intra-voxel dephasing results in signal intensity losses in the MR image. This artefact (susceptibility artefact) is less prominent in spin echo (SE) images compared to gradient echo (GE) images, due to the extra 180 degree refocusing pulse that can compensate for static magnetic field inhomogeneities [16,29,30]. In GE images, the artefact can be reduced by shortening the echo time [16,17,30], increasing the read-out gradient strength [30], aligning the material with the static magnetic field [6,16-18,30], and by using an MR scanner with lower field strength [16,17,30].

Eddy currents due to gradient switching may also cause signal intensity artefacts, so-called conductivity induced artefacts [29]. These artefacts increase with the strength and slew rate of the applied gradients [29]. In addition to signal intensity artefacts, both phenomena may induce geometric image distortions [16,31].

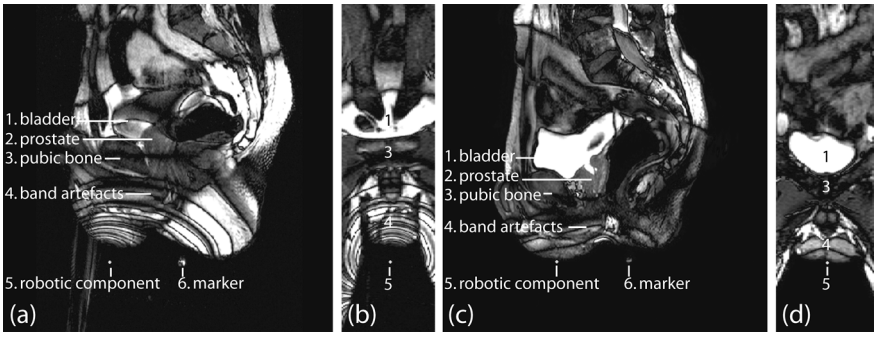

Figure 4.4. *Examples of signal intensity losses in a bSSFP MR image caused by the UMCU robotic (a,b) with ferromagnetic component, (c,d) after substituting the ferromagnetic component by a non-ferromagnetic component.*

To investigate the signal intensity artefacts caused by the UMCU robotic device, a volunteer was placed in front of the robot (without a needle) and a high resolution 3D balanced Steady State Free Precession (bSSFP) scan was acquired. This scan type is fast, provides a high T2/T1 contrast, but is sensitive to magnetic field inhomogeneities [32]. The main scan parameters were:

repetition time (TR) = 6.4 ms, echo time (TE) = 3.2 ms, acquisition time (T_{acq}) = 261 s, flip angle = 50°, read-out gradient 14.1 mT/m, FOV (FH/AP/RL) = 340 x 271 x 100 mm^3, acquisition voxel (FH/AP/RL) = 1.3 x 1.0 x 2.0 mm^3, overcontiguous slices = yes, number of signals averaged (NSA) = 6. Furthermore, a surface coil (SENSE Flex-L, Philips Healthcare, Best, The Netherlands) was used for signal reception.

In Figure 4.4a and 4.4b, black bands can be distinguished at the caudal end of the volunteer. These signal intensity losses are caused by the UMCU robot and indicate a distortion of the static magnetic field (act as 'isolines'). The artefacts bands are circularly shaped around a single point. Closer investigation of the UMCU robot revealed a small ferromagnetic pin at this location. The scan was repeated after the substitution of this ferromagnetic component by a non-ferromagnetic one. As a result the density of the black bands was strongly reduced (see Figures 4.4c and 4.4d).

4.4. Needle tip placement accuracy

In MRI-guided interventions the needle placement accuracy may be hampered by: geometric image distortions, the susceptibility artefact at the needle tip, tissue deformation during needle insertion and needle deflection. The latter cause will be discussed in the section 'safety'.

4.4.1. Geometric image distortions

Spins that are spatially encoded at the wrong position lead to geometric image distortions. These distortions hamper the needle placement accuracy, when the needle is shifted with respect to the target. In general, geometric image distortions [33] arise from non-linearity of the gradients (gradient errors) and the inhomogeneity of the static magnetic field (static field errors). The displacement due to the gradient error is independent of the orientation and strength of the applied gradient [33]. The size of the shift caused by the static error is inversely proportional to the gradient strength, and its direction is affected by the direction and polarity of this gradient [33].

The geometric image distortions can be induced by both the scanner and the object. Once the scanner-induced geometric errors are known, a correction for these errors can be performed [33]. The object-induced static field errors are caused by the difference in susceptibility between the robotic device and surrounding media. Eddy currents in the robotic device, caused by gradient switching, may induce gradient errors [16,31].

The geometric errors induced by the robot can be quantified using a grid phantom of equally spaced tubes (inter-tube distance = 4.2 cm, tube length = 34 cm and diameter = 4 mm) filled with $MnCl_2$ doped water (see Figure 4.5). The phantom was imaged in the 1.5 T Achieva MR scanner with and without the UMCU robot present. Two bSSFP scans were acquired with anterior as read-out gradient direction in the first scan and posterior in the second. In all scans the read-out gradient was 4.5 mT/m. Both datasets were summed to create an overlay. Furthermore, we applied the geometric image correction provided by the software of the MR scanner to correct for the scanner-induced geometric image distortions.

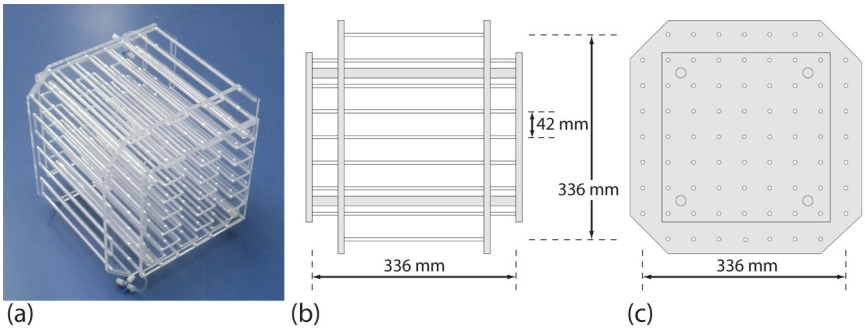

Figure 4.5. *(a) The tube phantom, (b and c) details of phantom geometry.*

In Figure 4.6, the white dots represent the cross-sections of the phantom tubes. The robot was situated at the feet side. Especially in this region, two shifted dots (belonging to the same tube) can be distinguished in the constructed overlays (see Figures 4.6a and 4.6b). The dot shift arises in the direction of the read-out gradient and is due to the static magnetic field error caused by the robot. Its magnitude equals half of the inter-dot distance and decreases with distance from the robot: e.g. 5.3 mm at the outer tube position close to the robot to 1.5 mm in the scanner isocenter. This corresponds to a static field

distortion of 16 and 5 parts per million (ppm), respectively. In the scans acquired without the robot present, only single dots can be distinguished, implying the static field error caused by the MR scanner is negligible.

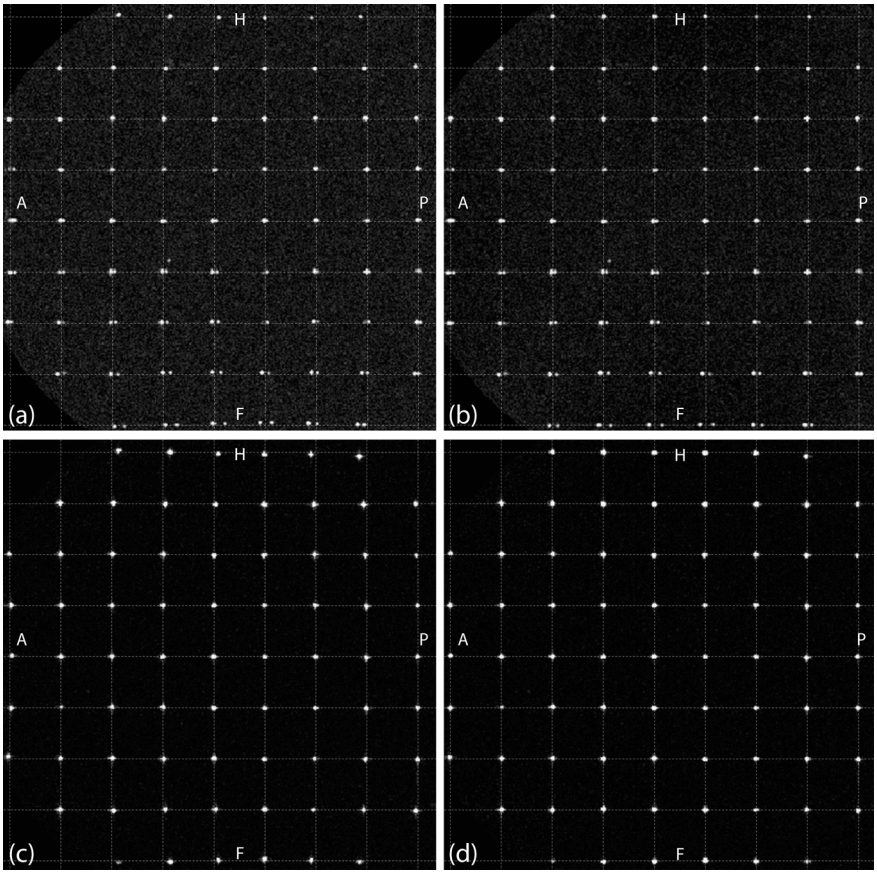

Figure 4.6. *(a) overlay of the two sagital planes of the tube phantom with the robot at the feet side, (b) overlay of both scans after applying the geometric image correction, (c) overlay of two bSSFP scans with opposed directions of the read-out gradient for a situation without the robot, (d) after applying the geometric image correction.*

The magnitude of the gradient error is defined as the distance between the mean dot position and the expected tube position based on the geometry of the phantom (cross point of the dashed lines in Figure 4.6). As illustrated in Figures 4.6b and 4.6d, the geometric image correction provided by the software

of the MR scanner can strongly reduce the magnitude of the gradient error (average tube position moves towards expected one). The differences in the gradient error between the situation with and without the robot present are negligible, except in the FH direction close to the robot. This implies the robot slightly affects the magnitude of the gradient error in this direction (error increase <2 mm).

4.4.2. The susceptibility artefact at the needle tip

As described in paragraph 4.3.3, a material with a susceptibility other than its surrounding medium induces a signal intensity artefact in the MR image. The appearance of this artefact depends on many geometric factors, e.g. material, shape, diameter, orientation [6,16-18,30], and acquisition parameters, e.g. sequence type, echo time, strength of read-out gradient [16,17,29,30]. In general, an intervention needle induces such an artefact, which may decrease the needle tip placement accuracy.

To illustrate the artefact dependency on the read-out direction and on the susceptibility difference between the intervention needle and the surrounding medium, a titanium needle (L = 20 cm, d = 1.65 mm) was inserted with the UMCU robot into two different phantoms to a depth of 10 cm in the 1.5 T Achieva scanner. The first phantom was a plastic cylinder (L = 20 cm, d = 11 cm) filled with gelatine. The second phantom was a piece of Dutch cheese. Two bSSFP scans with opposed directions of the read-out gradient were acquired. The main scan parameters were identical to the bSSFP scan in paragraph 4.3.3. The read-out gradient strength was high to minimize the geometric image distortions. The read-out directions were F and H. Also in this experiment the SENSE-flex-L coil was applied for signal reception.

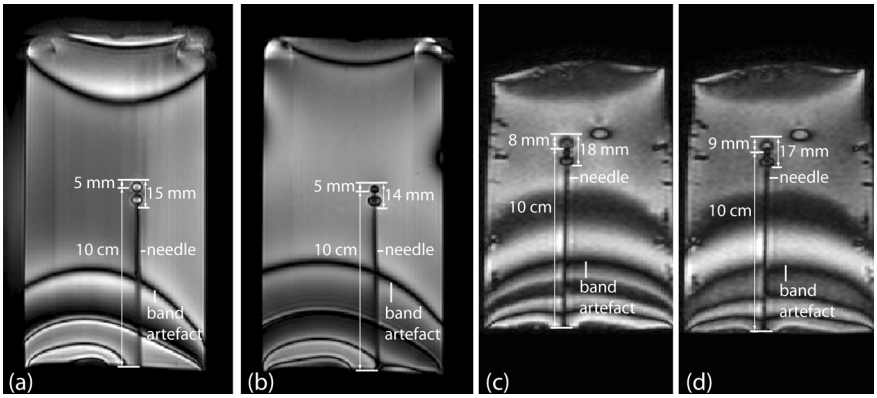

Figure 4.7. *Needle artefact in gelatin phantom for sagital image with (a) read-out direction F, (b) read-out direction H. Needle artefact in cheese phantom for coronal image with (c) read-out direction F, (d) read-out direction H.*

In the MR image of the gelatin phantom, the tip artefact is 15 mm in the scan with read-out direction F and equals 14 mm in the scan with read-out direction H. For the cheese phantom, the tip artefact is 18 mm and 17 mm in the image with read-out gradient F and H, respectively. Since the total needle artefact length is comparable in the images with opposite read-out gradients, it is assumed that the geometric image distortions are negligible. Hence, the needle insertion depth of 10 cm can be indicated in the images and the distance between the needle tip and the end of the artefact measured. This distance amounted 5 mm in the gelatin phantom and 8-9 mm in the cheese phantom. This difference is then caused by the susceptibility difference of the phantom material.

4.4.3. Tissue deformation during needle insertion

The third source that hampers the needle placement accuracy is the tissue deformation during needle insertion, as observed in experiments on patients [13,34]. These deformations are unpredictable [35], but can be minimized using advanced insertion techniques, such as needle shooting [10] and axial needle rotation [36]. The UMCU robot uses a tapping device [13] for needle tapping [37] to reduce deformation. The mean *in vivo* prostate motion during needle insertion can be reduced from 5.6 mm to 0.9 mm using the tapping device [34].

4.5. Safety

Regarding the patient safety, there are two main challenges that MRI-guided robotic devices have to cope with, namely needle deflection and RF-induced heating.

4.5.1. Needle deflection

Needle deflection is the primary source of needle placement error, especially for needles with an asymmetrical bevel [38]. Moreover, it can lead to undesired piercing of critical structures. By stepwise needle insertion and real-time MR imaging, the needle trajectory can be controlled [13]. If necessary the needle can be retracted for reinsertion.

To demonstrate the feasibility of real time needle tracking, a titanium needle including stylet (length 20 cm, outer diameter 1.65 mm) with a trocar point was tapped stepwise into a piece of Dutch cheese by the UMCU robot in the 1.5 T Achieva scanner. The target was marked by a wooden stick (see Figure 4.3) Fast bSSFP scans were acquired to monitor the needle trajectory during insertion.

These scans were composed of the orthogonal planes (coronal and sagital) with the intersection line on the needle according the following protocol: TR = 6.0 ms, TE = 3.0 ms, T_{acq} = 5 s, flip angle = 90°, read-out gradient 4.6 mT/m, FOV = 300 x 300 mm^2, acquisition voxel = 1.3 x 1.3 x 6.0 mm^3, number of slices = 2, NSA = 2. A surface coil (SENSE Flex-S, Philips Healthcare, Best, The Netherlands) was connected to the scanner for signal reception.

In Figure 4.8 a dark dot in the coronal plane and a dark line in the sagital plane can be discriminated. These structures correspond to the wooden stick. The black line that enlarges in the images of the different time points represents the needle. At the tip of the needle, a susceptibility artefact is clearly visible. Furthermore, artefacts caused by the air bubbles inside the cheese and some ringing artefacts caused by the robot can be distinguished.

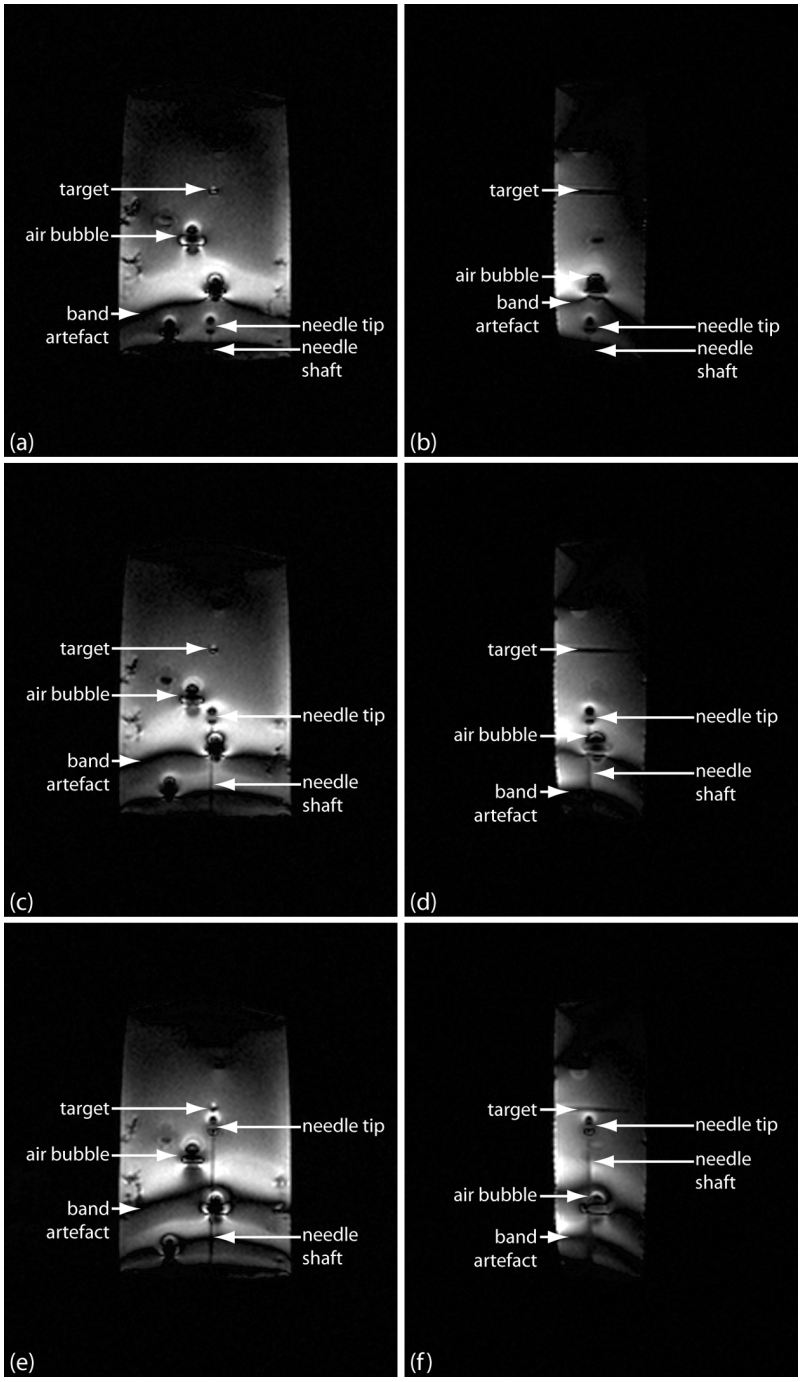

Figure 4.8. *(a, c, e) coronal and (b, d, f) sagital bSSFP images during needle tapping at different time points.*

4.5.2. RF-induced heating

The elongated conductive needle can act as a dipole antenna, which interacts with the electromagnetic RF field applied to generate an MR image [20,21,39-43]. The altered electric field is strongly increased at the tip of the needle, resulting in tissue heating in this region [41]. In case of resonance, temperature rises over 35ºC were reported in phantom experiments with long conductive wires [20,39]. The resonance properties and the amount of heat deposition depends on many factors, such as electrical properties [20,21] and volume [40,42] of the surrounding medium, the needle position within in the MR bore [42], the needle insertion depth or length [20,21,39,42,43], and the RF power of the sequence [21,39].

Due to the multiple factors, the amount of tissue heating is hard to predict. To investigate whether the intended intervention is safe with respect to the RF heating, (not a single but) several phantom experiments need to be performed that mimic worst case scenarios for the patient. Mostly, fiberoptic temperature sensors are positioned at the needle tip to measure the temperature increase [20,21,39,40,42,43]. A temperature versus insertion depth relation can be used to inspect whether a resonance situation was obtained [20,39,40,42]. Unwanted temperature rise can be predicted by analysis of the induced image artefacts around the needle [43].

The UMCU robot will be used for MRI-guided prostate interventions in a 1.5 T magnetic field. For this field strength, typical wavelengths in body tissue range from 43 cm in muscle to 105 cm in tissue with fat content [44]. The wavelength in air is larger, namely 470 cm [20]. This implies that (in theory) the minimal *in vivo* resonance length (half of wavelength) is 21.5 cm, when the needle is completely surrounded by muscle. Nevertheless, the resonance peak can be broad and differ from the calculated one [21]. It is also reported that the tip heating increases essentially quadratically with off-centre distance [42].

Since prostate interventions with the UMCU robot will be executed close to the isocenter of a 1.5 T MR scanner, centrally in the patient, and the required needle insertion depth is 6-13 cm to reach the entire prostate [45], we do not expect thermal injury using our robotic device with a 20 cm long titanium needle. To ensure the robotic device and the needle are uncoupled, they are interconnected by non-conductive plastic. In the several phantom experiments performed to mimic worst-case scenarios, no signs of heating were observed.

4.6. Discussion

This study provides an overview of the development considerations and quality assurance methods of a robotic device for MRI-guided needle interventions. To ensure that such a device is safe for use in an MRI environment, several general test methods were formulated [46,47]. Since evaluation criteria depend on the application, we applied a set of specific tests to ensure the safe introduction of MRI-guided prostate needle interventions using the UMCU robot in a 1.5 T closed bore MR scanner.

The geometry of robot devices is determined by the application and the space in the MR scanner. The space may be limited by the patient set-up, the use of moulds and additional coils.

Regarding the MR compatibility of a robotic device, the use of ferromagnetic materials is dissuaded. Not only because the ferromagnetic materials can become dangerous projectiles in a magnetic field [48,49], but also because they strongly disturb the MR image, as shown in Figure 4.4. The error source, a ferromagnetic pin, was too deep within the robotic device to be detected with a low-field hand magnet.

Since eddy currents may hamper the performance of the robot, it is recommended to minimize conductive loop areas and to avoid conductive loops where possible, for example by using non-conductive robotic materials. Nevertheless, in the 1.5 T magnetic field, the performance of the UMCU robot that contains various conductive components, was not limited by eddy currents. This demonstrates that an MR compatible robotic device can also be made of conductive materials.

The needle tip placement accuracy can be improved by reducing the scanner- and object-induced geometric image distortion. In general, the magnitude of the static field error can be reduced by increasing the read-out gradient [33] and in case of echo planar imaging (EPI) also the phase-encoding gradient [50]. The static field error can be further minimized by using materials with a susceptibility close to that of human tissue, like polymers. The magnitude of the gradient error can be strongly reduced by correcting for the MR scanner induced non-linearity of the gradients. The UMCU robot slightly enlarges the gradient error, probably due to eddy currents caused by gradient switching, but they are acceptable.

Needle tip artefacts are well understood, so that the underlying tip position can be reconstructed in tissue with known susceptibility [18]. Figure 4.7 illustrates the variation of needle tip artefact size in the bSSFP images of the cheese and gelatin phantom, suggesting it is harder to estimate the exact needle tip location in heterogeneous human tissue with unidentified susceptibility. The small dependence of the artefact shape on the direction of the read-out gradient might be explained by the inhomogeneous static magnetic field around the needle tip. The uncertainty in the needle tip localization can be reduced by the use of needle materials closer to human tissue and the optimization of the image sequence, e.g. larger read-out gradient strength, smaller echo time, and addition of an extra 180 degree refocusing pulse to compensate for static magnetic field inhomogeneities [6,16-18,29,30]. Furthermore, a marker placed on the robotic device can be used as a reference point to estimate the required needle insertion depth to reach the target [10]. In this case, both the marker and the target should be visualized during needle insertion to correct for any target displacement. Also for this set-up, it is recommended to monitor the needle trajectory and deflection.

Several advanced needle insertion techniques have been developed to minimize tissue deformation during needle insertion [10,36,37]. The UMCU robot taps the needle instead of pushing the needle into the prostate to minimize this deformation [13,34]. In the first in vivo experiments with our MR compatible robot, we still measured tissue deformation, despite the needle tapping [13]. This was due to the fact that the needle insertion speed (0.5 m/s) was lower than required [34]. This was caused by design changes that increased the mass of the needle holder, while the momentum remained approximately the same. The adverse consequences of insufficient needle velocity were not observed in our ex vivo experiments on the cheese and gelatin phantoms, which suggests that these phantom materials do not mimic the deformation of human tissue properly.

Needle deflection not only hampers the needle tip placement accuracy, but can also be a hazard for the patient when piercing critical structures. Frequent acquisition of two orthogonal MR images with the intersection line on the needle can be used to monitor the needle during insertion. Using these images, the needle trajectory can be controlled and needle deflection will be noticeable. Theoretically, the needle can move out of both planes without detection, therefore we also use a potentiometer to record needle insertion depth. If the needle deflects, it can be retracted for reinsertion. In the near future, it might

be possible to compensate for needle deflection using active steering needles [51].

Another safety risk is the tissue heating caused by resonating RF waves along an elongated conductive structure, such as the intervention needle [21,42]. Since it is hard to predict this situation under in vivo conditions [43], the risk is generally estimated using several phantom experiments that mimic worst-case scenarios for the patient. Mostly, fiberoptic temperature sensors are used to measure the temperature at the tip of the structure [20,21,39,40,42,43]. Since the heating is deposited locally, the measured temperature is highly dependent on the location of the temperature sensor with respect to the tip [41,52]. Another way to monitor the induced heating is by performing MR thermometry [52]. However, MR thermometry is hardly possible close to the needle tip due to the susceptibility artefact [52]. Our method based on RF induced image artefacts is a powerful and sensitive method to investigate the RF safety [43]. A new qualitative technique to estimate the safety risk is based on reversed RF polarization [53]. The last two methods are effective for detecting potentially dangerous situations non-invasively, although they do not measure the exact heat deposition at the needle tip.

The risk of tissue heating at the needle tip can be reduced by the use of needle coating [21] or can even be excluded by using non-conductive needle materials. In theory, the RF waves can also induce currents in the conductive robotic components, resulting in heating in the surrounding tissue. Therefore, any contact of the patient with conductive robotic components (except the needle) should be avoided.

4.7. Conclusion

This study gives an overview of the main challenges of the development and clinical introduction of robotic devices for MRI-guided interventions. It gives background information, identifies the main pitfalls and provides insights on how to deal with them. This study is useful for people new in the field and for institutes, willing to further optimise their robotic device or introduce their robotic device into the clinic.

References

[1] Tempany C, Straus S, Hata N, Haker S, "MR-guided prostate interventions," *J Magn Reson Imaging.* **27**, 356-367 (2008).

[2] Jürgenliemk-Schulz IM, Tersteeg RJHA, Roesink JM, Bijmolt S, Nomden CN, Moerland MA, de Leeuw AAC, "MRI-guided treatment-planning optimisation in intracavitary or combined intracavitary/interstitial PDR brachytherapy using tandem ovoid applicators in locally advanced cervical cancer," *Radiother Oncol.* **93**, 322-330 (2009).

[3] Peters NHGM, Meeuwis C, Bakker CJG, Mali WPThM, Fernandez-Gallardo AM, van Hillegersberg R, Schipper MEI, van den Bosch MAAJ, "Feasibility of MRI-guided large-core-needle biopsy of suspiscious breast lesions at 3 T," *Eur Radiol.* **19**, 1639-1644 (2009).

[4] Hambrock T, Somford DM, Hoeks C, Bouwense SAW, Huisman H, Yakar D, van Oort IM, Witjes JA, Fütterer JJ, Barentsz JO, "Magnetic resonance imaging guided prostate biopsy in men with repeat negative biopsies and increased prostate specific antigen," *J Urol.* **183**, 520-527 (2010).

[5] Kerkhof EM, Raaymakers BW, van der Heide UA, van de Bunt L, Jürgenliemk-Schulz IM, Lagendijk JJW, "Online MRI guidance for healthy tissue sparing in patients with cervical cancer: an IMRT planning study," *Radiother Oncol.* **88**, 241-249 (2008).

[6] Kühn JP, Langner S, Hegenscheid K, Evert M, Kickhefel A, Hosten N, Puls R, "Magnetic resonance-guided upper abdominal biopsies in a high-field wide-bore 3-T MRI system: feasibility, handling, and needle artifacts," *Eur Radiol.* **20**, 2414-2421 (2010).

[7] DiMaio SP, Pieper S, Chinzei K, Hata N, Haker SJ, Kacher DF, Fichtinger G, Tempany CM, Kikinis R, "Robot-assisted needle placement in open MRI: system architecture, integration and validation," *Comput Aided Surg.* **12**, 15-24 (2007).

[8] Fischer GS, Iordachita I, Csoma C, Tokuda J, DiMaio SP, Tempany CM, Hata N, Fichtinger G, "MRI-compatible pneumatic robot for transperineal prostate needle placement," *IEEE/ASME Trans Mechatron.* **13**, 295-305 (2008).

[9] Melzer A, Gutmann B, Remmele T, Wolf R, Lukoscheck A, Bock M, Bardenheuer H, Fischer H, "INNOMOTION for percutaneous image-guided interventions: principles and evaluation of this MR- and CT-compatible robotic system," *IEEE Eng Med Biol Mag.* **27**, 66-73 (2008).

[10] Muntener M, Patriciu A, Petrisor D, Schär M, Ursu D, Song DY, Stoianovici D, "Transperineal prostate intervention: robot for fully automated MR imaging-system description and proof of principle in a canine model," *Radiology.* **247**, 543-549 (2008).

[11] Morikawa S, Naka S, Murakami K, Kurumi Y, Shiomi H, Tani T, Haque HA, Tokuda J, Hata N, Inubushi T, "Preliminary clinical experiences of a motorized manipulator for magnetic resonance image-guided microwave coagulation therapy of liver tumors," *Am J Surg.* **198**, 340-347 (2009).

[12] Schouten MG, Ansems J, Renema WK, Bosboom D, Scheenen TWJ, Fütterer JJ, "The accuracy and safety aspects of a novel robotic needle guide manipulator to perform transrectal prostate biopsies," *Med Phys.* **37**, 4744-4750 (2010).

[13] van den Bosch MR, Moman MR, van Vulpen M, Battermann JJ, Duiveman E, van Schelven LJ, de Leeuw H, Lagendijk JJW, Moerland MA, "MRI-guided robotic system for transperineal prostate interventions: proof of principle," *Phys Med Biol.* **55**, 133-140 (2010).

[14] Gossmann A, Bangard C, Warm M, Schmutzler RK, Mallmann P, Lackner KJ, "Real-time MR-guided wire localization of breast lesions by using an open 1.0-T imager: initial experience," *Radiology.* **247**, 535-542 (2008).

[15] van den Bosch MAAJ, Daniel BL, Pal S, Nowels KW, Birdwell RL, Jeffrey SS, Ikeda DM, "MRI-guided needle localization of suspicious breast lesions: results of a freehand technique," *Eur Radiol.* **16**, 1811-1817 (2006).

[16] Guermazi A, Miaux Y, Zaim S, Peterfy CG, White D, Genant HK, "Metallic artefacts in MR imaging: effects of main field orientation and strength," *Clin Radiol.* **58**, 322-328 (2003).

[17] Müller-Bierl B, Graf H, Lauer U, Steidle G, Schick F, "Numerical modeling of needle tip artifacts in MR gradient echo imaging," *Med Phys.* **31**, 579-587 (2004).

[18] Lagerburg V, Moerland MA, Seppenwoolde JH, Lagendijk JJW, "Simulation of the artefact of an iodine seed placed at the needle tip in MRI-guided prostate brachytherapy," *Phys Med Biol.* **53**, 59-67 (2008).

[19] Machann J, Schlemmer HP, Schick F, "Technical challenges and opportunities of whole-body magnetic resonance imaging at 3T," *Phys Med.* **24**, 63-70 (2008).

[20] Dempsey MF, Condon B, Hadley DM, "Investigation of the factors responsible for burns during MRI," *J Magn Reson Imaging.* **13**, 627-631 (2001).

[21] Yeung CJ, Susil RC, Atalar E, "RF safety of wires in interventional MRI: using a safety index," *Magn Reson Med.* **47**, 187-193 (2002).

[22] van den Bergen B, van den Berg CAT, Klomp DWJ, JJW Lagendijk, "SAR and power implications of different RF shimming strategies in the pelvis for 7T MRI," *J Magn Reson Imaging.* **30**, 194-202 (2009).

[23] Schenck JF, "Safety of strong, static magnetic fields," *J Magn Reson Imaging.* **12**, 2-19 (2000).

[24] Dempsey MF, Condon B, Hadley DM, "MRI safety review," *Semin Ultrasound CT MR.* **23**, 392-401 (2002).

[25] Shellock FG, "Biomedical implants and devices: assessment of magnetic field interactions with a 3 0-Tesla MR system," *J Magn Reson Imaging.* **16**, 721-732 (2002).

[26] Van Gellekom MPR, Moerland MA, Battermann JJ, Lagendijk JJW, "MRI-guided prostate brachytherapy with single needle method-a planning study," *Radiother Oncol.* **71**, 327-332 (2004).

[27] Robertson NM, Diaz-Gomez M, Condon B, "Estimation of torque on mechanical heart valves due to magnetic resonance imaging including an estimation of the significance of the Lenz effect using a computational model," *Phys Med Biol.* **45**, 3793-3807 (2000).

[28] Graf H, Lauer UA, Schick F, "Eddy-current induction in extended metallic parts as a source of considerable torsional moment," *J Magn Reson Imaging.* **23**, 585-590 (2006).

[29] Graf H, Steidle G, Martirosian P, Lauer UA, Schick F, "Metal artifacts caused by gradient switching," *Magn Reson Med.* **54**, 231-234 (2005).

[30] Port JD, Pomper MG, "Quantification and minimization of magnetic susceptibility artifacts on GRE images," *J Comput Assist Tomogr.* **24**, 958-964 (2000).

[31] Haacke EM, Brown RW, Thompson MR, Venkatesan R, *Magnetic Resonance Imaging – physical principles and sequence design*, 1st ed. (John Wiley & Sons, New York, 1999).

[32] Scheffler K, Lehnhardt S, "Principles and applications of balanced SSFP techniques," *Eur Radiol.* **13**, 2409-2418 (2003).

[33] Bakker CJG, Moerland MA, Bhagwandien R, Beersma R, "Analysis of machine-dependent and object-induced geometric distortion in 2DFT MR imaging," *Magn Reson Imaging.* **10**, 597-608 (1992).

[34] Lagerburg V, Moerland MA, van Vulpen M, Lagendijk JJW, "A new robotic needle insertion method to minimise attendant prostate motion," *Radiother Oncol.* **80**, 73-77 (2006).

[35] Lagerburg V, Moerland MA, Lagendijk JJW, Battermann JJ, "Measurement of prostate rotation during insertion of needles for brachytherapy," *Radiother Oncol.* **77**, 318-323 (2005).

[36] Abolhassani N, Patel R, Moallem M, "Control of soft tissue deformation during robotic needle insertion," *Minim Invasive Ther Allied Technol.* **15**, 165-176 (2006).

[37] Lagerburg V, Moerland MA, Konings MK, van de Vosse RE, Lagendijk JJW, Battermann JJ, "Development of a tapping device: a new needle insertion method for prostate brachytherapy," *Phys Med Biol.* **51**, 891-902 (2006).

[38] Blumenfeld P, Hata N, DiMaio S, Zou K, Haker S, Fichtinger G, Tempany CMC, "Transperineal prostate biopsy under magnetic resonance image guidance: a needle placement accuracy study," *J Magn Reson Imaging.* **26**, 688-694 (2007).

[39] Konings MK, Bartels LW, Smits HFM, Bakker CJG, "Heating around intravascular guidewires by resonating RF waves," *J Magn Reson Imaging.* **12**, 79-85 (2000).

[40] Pictet J, Meuli R, Wicky S, van der Klink JJ, "Radiofrequency heating effects around resonant lengths of wire in MRI," *Phys Med Biol.* **47**, 2973-2985 (2002).

[41] Park SM, Kamondetdacha R, Nyenhuis JA, “Calculation of MRI-induced heating of an implanted medical lead wire with an electric field transfer function,” *J Magn Reson Imaging.* **26**, 1278-1285 (2007).

[42] Yeung CJ, Karmarkar P, McVeigh ER, “Minimizing RF heating of conducting wires in MRI,” *Magn Reson Med.* **58**, 1028-1034 (2007).

[43] van den Bosch MR, Moerland MA, Lagendijk JJW, Bartels LW, van den Berg CAT, “New method to monitor RF safety in MRI-guided interventions based on RF induced image artifacts,” *Med Phys.* **37**, 814-821 (2010).

[44] Mohsin SA, Sheikh NM, Saeed U, “MRI-induced heating of deep brain stimulation leads,” *Phys Med Biol.* **53**, 5745-5756 (2008).

[45] Fu L, Ng WS, Liu H, O'Dell W, Rubens D, Strang J, Schell MC, Brasacchio R, Liao L, Messing E, Yu Y, “Bouquet brachytherapy: feasibility and optimization of conically spaced implants,” *Brachytherapy.* **4**, 59-63 (2005).

[46] Schaefers G, “Testing MR safety and compatibility: an overview of the methods and current standards,” *IEEE Eng Med Biol Mag.* **27**, 23-27 (2008).

[47] Yu N, Gassert R, Riener R, “Mutual interferences and design principles for mechatronic devices in magnetic resonance imaging,” *Int J Comput Assist Radiol Surg.* [ahead of print] (2010).

[48] Condon B, Hadley DM, Hodgson R, “The ferromagnetic pillow: a potential MR hazard not detectable by a hand-held magnet,” *Br J Radiol.* **74**, 847-851 (2001).

[49] Zimmer C, Janssen MN, Treschan TA, Peters J, “Near-miss accident during magnetic resonance imaging by a "flying sevoflurane vaporizer" due to ferromagnetism undetectable by handheld magnet,” *Anesthesiology.* **100**, 1329-1330 (2004).

[50] Jezzard P, Clare S, “Sources of distortion in functional MRI data,” *Hum Brain Mapp.* **8**, 80-85 (1999).

[51] Park Y-L, Elayaperumal S, Ryu S, Daniel B, Black RJ, Moslehi B, Cutkosky MR, “MRI-compatible Haptics: Strain sensing for real-time estimation of three dimensional needle deflection in MRI environments,” *oral presentation at the ISMRM 17th scientific meeting & exhibition*, Honolulu, USA (2009).

[52] Ehses P, Fidler F, Nordbeck P, Pracht ED, Warmuth M, Jakob PM, Bauer WR, “MRI thermometry: Fast mapping of RF-induced heating along conductive wires,” *Magn Reson Med.* **60**, 457-461 (2008).

[53] Overall WR, Pauly JM, Stang PP, Scott GC, “Ensuring safety of implanted devices under MRI using reversed RF polarization,” *Magn Reson Med.* **64**, 823-833 (2010).

This chapter has been published as:

van den Bosch MR, Moman MR, van Vulpen M, Battermann JJ, Duiveman E, van Schelven LJ, de Leeuw H, Lagendijk JJW, Moerland MA, "MRI-guided robotic system for transperineal prostate interventions: proof of principle," *Phys Med Biol.* **55**, 133-140 (2010).

MRI-guided robotic system for transperineal prostate interventions: proof of principle

5

Abstract

In this study, we demonstrate the proof of principle of the University Medical Center Utrecht (UMCU) robot dedicated for Magnetic Resonance Imaging (MRI)-guided interventions in patients. The UMCU robot consists of polymers and non-ferromagnetic materials. For transperineal prostate interventions, it can be placed between patient's legs inside a closed bore 1.5 T MR scanner. The robot can manually be translated and rotated resulting in five degrees of freedom. It contains a pneumatically driven tapping device to automatically insert a needle stepwise into the prostate using a controller unit outside the scanning room. To define the target positions and to verify the needle insertion point and the needle trajectory, a high-resolution 3D balanced Steady State Free Precession (bSSFP) scan that provides a T_2/T_1-weighted contrast is acquired. During the needle insertion fast 2D bSSFP images are generated to track the needle on-line. When the target position is reached, the radiation oncologist manually places a fiducial gold marker (small seed) at this location. In total two needle trajectories are used to place all markers. Afterwards, a high-resolution 3D bSSFP scan is acquired to visualize the fiducial gold markers. Four fiducial gold markers were placed transperineally into the prostate of a patient with a clinical stage T3 prostate cancer. In the generated scans, it was possible to discriminate the patient's anatomy, the needle and the markers. All markers were delivered inside the prostate. The procedure time was 1.5 h. This study proves that needle placement and seed delivery in the prostate with the UMCU robot are feasible.

5.1. Introduction

In the diagnostic and treatment procedures in prostate cancer such as biopsies and brachytherapy, magnetic resonance imaging (MRI) offers superior soft tissue contrast and consequently improved lesion detection [1]. Therefore, MR-compatible robotic systems allowing real on-line MRI guidance would be extremely valuable with these procedures [2-6].

Technical difficulties, such as the restriction of using solely non-ferromagnetic materials, the limited space within the MR bore [2,7], the needle-induced prostate rotation and deformation [8,9], the needle-induced susceptibility imaging artefacts [10] and the RF heating of the needles and catheters [11,12], make robotic MRI guidance a hard task.

We worked for several years on the development of an MR-compatible robotic system which is able to solve the above-mentioned problems and allows reliable on-line MRI guidance [2,7-11]. In this study we describe our first clinical experiences of this University Medical Center Utrecht (UMCU) robot dedicated for MRI-guided interventions in patients, as a proof of principle.

5.2. Materials and methods

In this institutional review board approved study, we deliver fiducial gold markers (small seeds) inside prostates of patients eligible for external beam radiotherapy treatment (EBRT) using our MRI-guided robot. The markers will be used for the position verification of the prostate during EBRT [13].

Since the marker placement accuracy criteria are soft (target volume is the whole prostate gland), the MRI-guided implantation of these markers is ideal for *in vivo* investigation of the performance of the robot in a 1.5 T magnetic field, the ability to track the needle during insertion with fast MR images and the ability to place a small seed in the prostate.

The main characteristics of the first patient included in this study are the clinical tumour stage T3, age 76 years, body weight 84 kg, length 1.76 m, BMI 27 kg m^{-2}, prostate volume 75 cc.

5.2.1. Procedure

In accordance with the current manual ultrasound (US)-guided transperineal implantation technique, four gold markers (length 5 mm, outer diameter 1 mm) with a steel inner core (length 5 mm, diameter 0.1 mm) were placed with the UMCU robot transperineally inside the prostate using two parallel needle trajectories.

The patient was placed in supine position on the MR table with legs spread within the MR bore to provide space for the robot as shown in Figure 5.1. For anaesthesia, lidocaine was injected in the perineal area prior to the procedure.

The needle insertion points at the perineum were determined by the radiation oncologist, each point about 1 cm lateral from the midplane. The needle was pushed manually just beneath the patient's skin through one of the insertion points. A high-resolution 3D MR scan (see paragraph 5.2.3 for more scan details) was acquired to check whether the prostate was freely accessible following the needle trajectory and to define a target position.

After image inspection, the robot tapped the needle stepwise towards this position while controlling the step size (typically 5 mm) and the needle depth. During the tapping fast 2D MR scans were acquired to track the needle trajectory on-line and to independently monitor the needle depth.

When the target position was reached the radiation oncologist manually placed a gold marker through the needle at this location. Then, the needle was tapped backwards to the second target position located on the same needle trajectory and the second marker was delivered. Next, the needle was tapped out of the patient and a second 3D MR scan generated to visualize the gold markers. This process was repeated for the second needle.

After the procedure, the patient was asked to define the pain score on the visual analogue scale (range 0-10, where 0 and 10 represent no pain and severe pain, respectively).

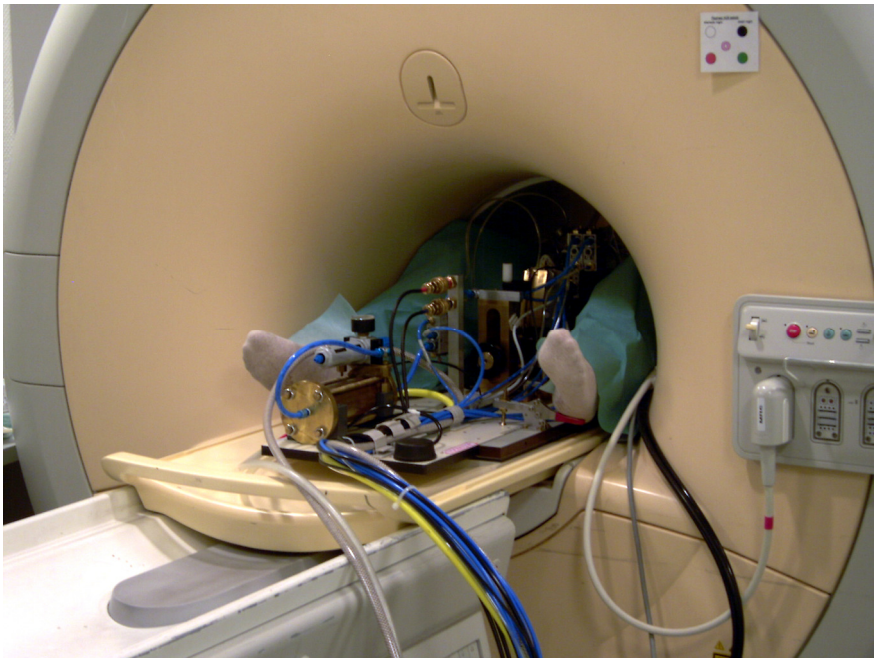

Figure 5.1. *Illustration of experimental set-up. The robot was positioned between the legs of the patient.*

5.2.2. Robot

The robot consists of polymers and non-ferromagnetic materials such as brass, copper, titanium and aluminium, and is pneumatically and hydraulically driven (see Figure 5.2). The robot fits inside a closed 1.5 T MR scanner (Achieva, Philips Healthcare, Best, The Netherlands) and can generally be placed between the legs of a patient with a body mass index (BMI) of <30 kg m^{-2} (see Figure 5.1). The robot is fixated on a wooden plateau that can be slid over the MR table. A clamp is used to hold this plateau at a chosen position (see Figure 5.1).

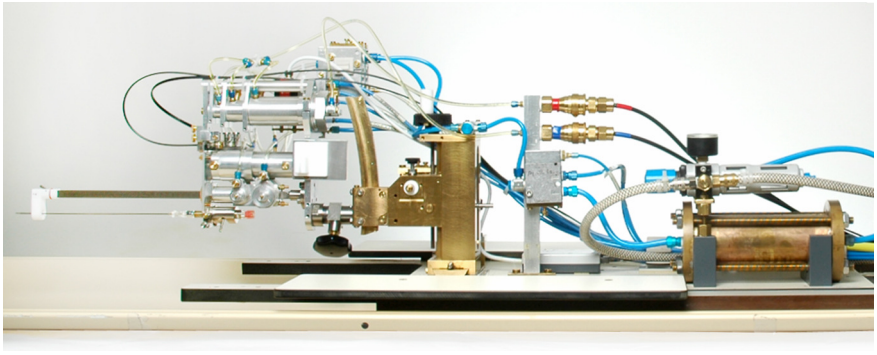

Figure 5.2. *Picture of the UMCU robot that was used for the MRI-guided fiducial gold marker implantation.*

The robot contains a tapping device to pneumatically tap a titanium needle including stylet (length 20 cm, outer diameter 1.65 mm) stepwise into the patient. Stepwise tapping has two major advantages: due to the high needle insertion speed tissue deformation will be reduced [8,9], and the needle trajectory can be controlled and modified in the time breaks between the steps. The tapping device produces a momentum of approximately 0.6 Ns. The maximum insertion depth of the needle per tap, the so-called stepsize, is adjustable using a buffer stop set by a hydraulic cylinder. The stepsize is measured by a potentiometer and the accuracy is <1 mm.

Both the tapping device and bufferstop can be controlled outside the scanning room using a controller unit, enabling the radiation oncologist to monitor the needle insertion on the MR scans in the operating room.

The tapping part can be manually rotated and translated offering five degrees of freedom. In this way, the entire prostate gland can be reached [2]. In this study, however, only needle trajectories parallel to the MR bore were chosen.

5.2.3. Imaging

Since the needle should not penetrate critical structures as rectum and pubic arch, and the markers have to be delivered inside the prostate gland, the MR images should not only visualize the needle and markers, but also patient's anatomy. For the implantation of the markers, a clear distinction of the prostatic border rather than the tumour is important. Furthermore, the field of view (FOV) of the MR scans should be large to cover both the insertion point and prostate, while the acquisition time ought to be short to allow frequent image acquisitions. We applied balanced Steady State Free Precession (bSSFP) sequences to generate the desired images. These scans provide a T2/T1-weigthed contrast [14].

For the high-resolution 3D bSSFP scan we used the following scan protocol: repetition time (TR) = 6.4 ms, echo time (TE) = 3.2 ms, acquisition time (T_{acq}) = 261 s, flip angle = 50°, read-out bandwidth (BW_{read}) = 781.3 Hz/voxel, FOV (FH/AP/RL) = 340 x 271 x 100 mm^3, acquisition voxel (FH/AP/RL) = 1.3 x 1.0 x 2.0 mm^3, overcontiguous slices = yes, number of signals averaged (NSA) = 6.

The following scan protocol was applied to generate dynamic 2D bSSFP scans: TR = 5.7 ms, TE = 2.8 ms, T_{acq} = 5.2 s, flip angle = 45°, BW_{read} = 256.6 Hz/voxel, FOV = 300 x 300 mm^2, acquisition voxel = 1.3 x 1.3 x 10.0 mm^3, number of slices = 2, NSA = 2. These scans were planned in less than a minute to acquire images in two orthogonal planes (coronal and sagittal) with the insertion line of the planes on the needle trajectory. The position of the first 2D plane was set on the already acquired 3D bSSFP scan, while the location of the second orthogonal 2D plane was planned using the first generated 2D scan. In all scans a surface coil (SENSE Flex-L, Philips Healthcare, Best, The Netherlands) was used for signal reception.

5.3. Results

Needle insertion was monitored on dynamic MR imaging in two planes. Figure 5.3 shows several dynamic scans that were generated at different time points during needle insertion.

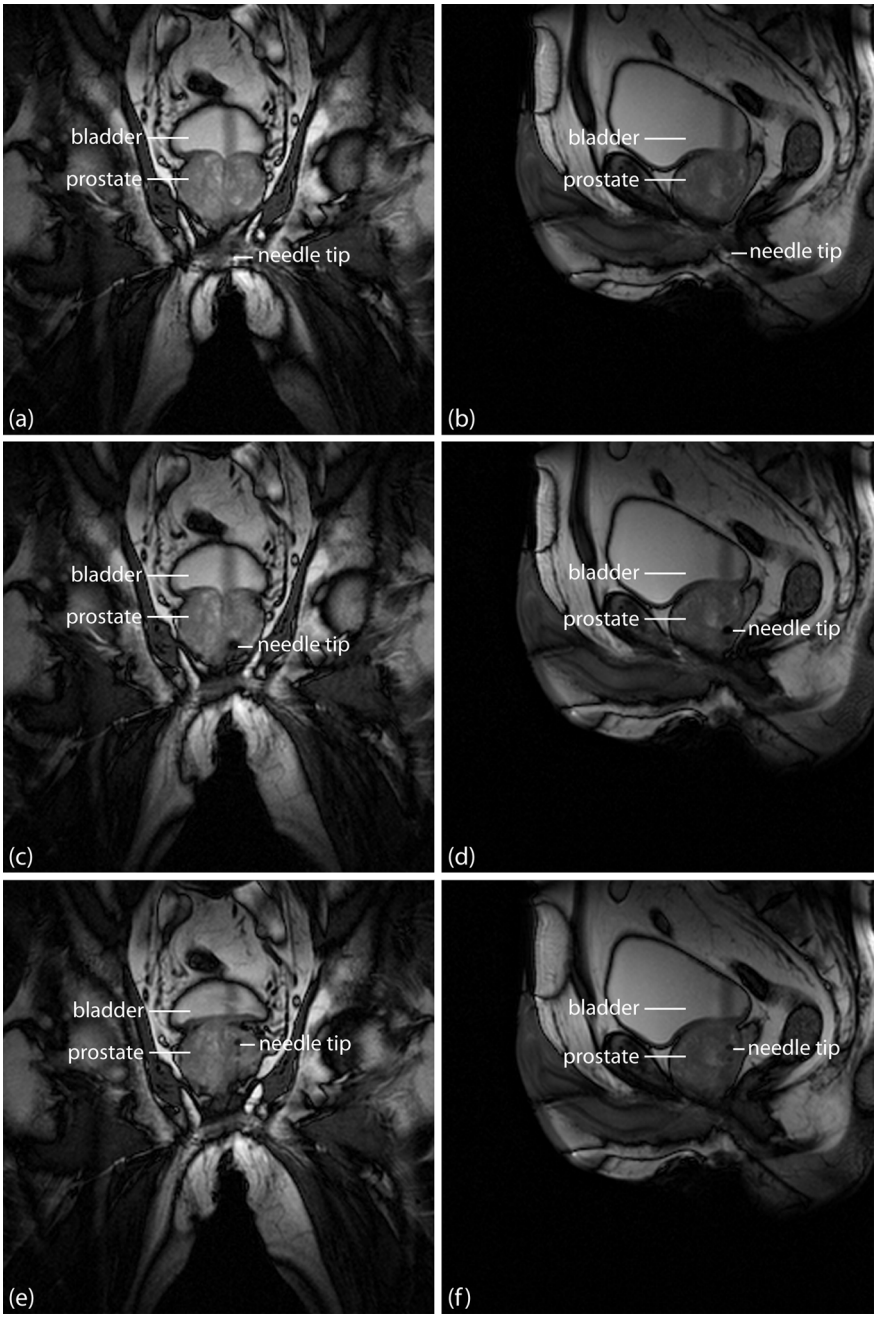

Figure 5.3. *Coronal (a, c, e) and sagittal planes (b, d, f) of the needle and the prostate at three different time points.*

Anatomical structures such as prostate, rectum and bladder are clearly visible. Furthermore, the needle can be distinguished due to a susceptibility artefact. The tip is better visible than the shaft. This figure also illustrates that some prostate deformation still occurs during the needle insertion. The displacement of the prostate base in Figure 5.3e (needle in prostate) with respect to Figure 5.3a (before prostate insertion) was 7 mm.

In Figure 5.4a one of the acquired 3D bSFFP images is shown. This scan was generated after the insertion of the first needle just beneath the skin to control the intended needle trajectory. The needle artefact and patients anatomical structures are well definable. Small image artefacts due to the needle guide of the robot are visible. In Figure 5.4b another 3D bSFFP scan is shown, which was acquired at the end of the procedure. The gold markers induce a susceptibility artefact in the image, which makes it possible to localize them.

The robot was able to tap the needle stepwise into the prostate with a stepsize ranging from 2 to 8 mm. All markers were delivered inside the prostate. The procedure time was 1.5 h. Pain score on the visual analogue scale was 2.5 points.

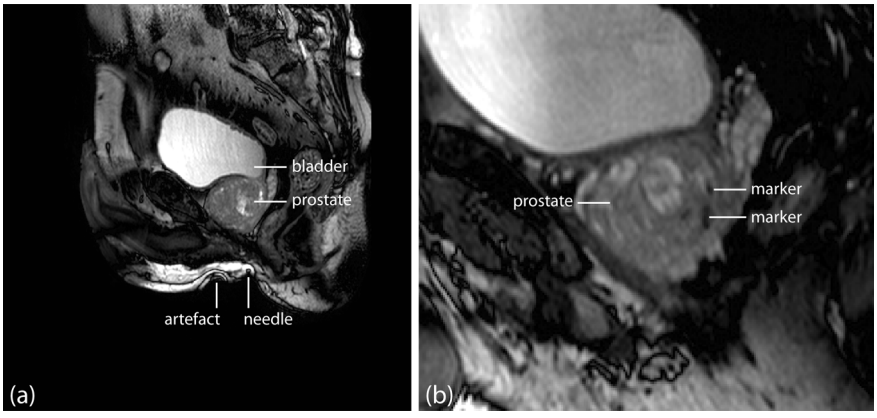

Figure 5.4. *(a) 3D bSSFP scan after the insertion of the first needle to control intended needle trajectory, (b) 3D bSSFP at the end of the procedure.*

5.4. Discussion

This study reveals MRI-guided interventions are possible using the UMCU robot. The robot was able to tap the needle stepwise into the prostate during acquisition of fast dynamic 2D bSSFP scans to track the needle on-line. In only 5 s two images of orthogonal slices were obtained that visualized both the patient's anatomy and the needle, as shown in Figure 5.3.

Since the susceptibility artefact around a titanium needle parallel to the static magnetic field is confined to the tip, the needle tip is better visible than the shaft in Figure 5.3. From simulations and experiments we know that the real needle tip is approximately 5 mm proximal from the outer edge of the artefact using the bSSFP sequences of this study at 1.5 T [10]. The shaft of the needle can also be distinguished in these images, mainly due to a signal void, and may become more prominent when the slice thickness is reduced. In the same figure a prostate deformation up to 7 mm was measured, which suggests to further increase the needle insertion speed [8,9].

The robot was MR-compatible, because no forces were measured when sliding the robot into the MR scanner. Nevertheless, the robot causes some image artefacts (see Figure 5.4). These artefacts are due to the susceptibility differences between the robot materials and human tissue and indicate the presence of local magnetic field distortions [10,14]. These magnetic field distortions will lead to geometric image distortions [15], which are confined to the region around the robot and minimized by the use of large read-out gradients, so that they are negligible near the target position.

The patient was comfortable with the procedure. He was not deterred by the movements of the robot or the noise of the MR scanner.

For this first patient the procedure time was 1.5 h. We aim to reduce the procedure time to about 45 min by speeding up the manual procedure steps as well as the imaging acquisitions. This might allow the acquisition of more (3D) MR images to investigate the marker placement accuracy under *in vivo* conditions. Up until now we have concentrated on needle tracking and needle insertion accuracy.

In the future, we want to test the procedure for angular needle insertion and develop software to automatically track the tip of the needle and target position. This software may be used to further automate the procedure.

Furthermore, we want to use the UMCU robot for MRI-guided diagnostic and treatment procedures such as biopsies and brachytherapy in the prostate. For these purposes, we would like to combine (or replace) our fast bSSFP scans with MR scans optimized for tumour visualisation.

Because of its unique way of needle insertion (tapping rather than pushing), which minimizes tissue deformation, the UMCU robot may also be useful for diagnostic and treatment procedures at other sites, where tissue deformation due to needle insertion is problematic, like breast.

5.5. Conclusion

This study shows that it is feasible to place fiducial gold markers in the prostate under MRI guidance using the UMCU robot. The possibility to tap a needle and to deliver seeds in the prostate under MRI guidance with our robot is a major step towards MRI-guided prostate brachytherapy and biopsies. It proves that *in vivo* MRI-guided robotic interventions are possible.

Acknowledgements

We would like to thank T Nguyen (department of Radiotherapy, University Medical Center Utrecht) for assistance with the implantation, J Verwoerd (Philips Healthcare Nederland) for the MR sequence developments, and the Department of Medical Technology & Clinical Physics (University Medical Center Utrecht) for building the robot and for the technical support during the first clinical test. This work was funded by the Dutch Cancer Society (project UU 2006-3638).

References

[1] Barentsz J, Takahashi S, Oyen W, Mus R, De Mulder P, Reznek R, Oudkerk M, Mali W, "Commonly used imaging techniques for diagnosis and staging," *J Clin Oncol.* **24**, 3234-3244 (2006).

[2] Van Gellekom MPR, Moerland MA, Battermann JJ, Lagendijk JJW, "MRI-guided prostate brachytherapy with single needle method-a planning study," *Radiother Oncol.* **71**, 327-332 (2004).

[3] Beyersdorff D, Winkel A, Hamm B, Lenk S, Loening SA, Taupitz M, "MR imaging-guided prostate biopsy with a closed MR unit at 1.5 T: initial results," *Radiology.* **234**, 576-581 (2005).

[4] Zangos S, Herzog C, Eichler K, Hammerstingl R, Lukoschek A, Guthmann S, Gutmann B, Schoepf UJ, Costello P, Vogl TJ, "MR-compatible assistance system for punction in a high-field system: device and feasibility of transgluteal biopsies of the prostate gland," *Eur. Radiol.* **17**, 1118-1124 (2007).

[5] Fischer GS, Iordachita I, Csoma C, Tokuda J, DiMaio SP, Tempany CM, Hata N, Fichtinger G, "MRI-compatible pneumatic robot for transperineal prostate needle placement," *IEEE/ASME Transactions on Mechatronics.* **13**, 295-305 (2008).

[6] Muntener M, Patriciu A, Petrisor D, Schär M, Ursu D, Song DY, Stoianovici D, "Transperineal prostate intervention: robot for fully automated MR imaging-system description and proof of principle in a canine model," *Radiology.* **247**, 543-549 (2008).

[7] van den Bosch MR, Lips IM, Lagerburg V, van Vulpen M, Lagendijk JJW, Moerland MA, "Feasibility of adequate dose coverage in permanent prostate brachytherapy using divergent needle insertion methods," *Radiother Oncol.* **86**, 120-125 (2008).

[8] Lagerburg V, Moerland MA, Konings MK, van de Vosse RE, Lagendijk JJW, Battermann JJ, "Development of a tapping device: a new needle insertion method for prostate brachytherapy," *Phys Med Biol.* **51**, 891-902 (2006).

[9] Lagerburg V, Moerland MA, van Vulpen M, Lagendijk JJW, "A new robotic needle insertion method to minimise attendant prostate motion," *Radiother Oncol.* **80**, 73-77 (2006).

[10] Lagerburg V, Moerland MA, Seppenwoolde JH, Lagendijk JJW, "Simulation of the artefact of an iodine seed placed at the needle tip in MRI-guided prostate brachytherapy," *Phys Med Biol.* **53**, 59-67 (2008).

[11] van den Bosch MR, Moerland MA, van Lier ALHMW, Bartels LW, Lagendijk JJW, van den Berg CAT, "New method to quantify RF induced currents inside conductive wires," *e-poster at 17th Scientific Meeting & Exhibition ISMRM*, Honolulu, USA, 2009.

[12] Yeung CJ, Karmarkar P, McVeigh ER, “Minimizing RF heating of conducting wires in MRI,” *Magn Reson Med.* **58**, 1028-1034 (2007).

[13] Van der Heide UA, Kotte ANTJ, Dehnad H, Hofman P, Lagendijk JJW, van Vulpen M, “Analysis of fiducial marker-based position verification in the external beam radiotherapy of patients with prostate cancer,” *Radiother Oncol.* **82**, 38-45 (2007).

[14] Scheffler K, Lehnhardt S, “Principles and applications of balanced SSFP techniques,” *Eur Radiol.* **13**, 2409-2418 (2003).

[15] Moerland MA, Beersma R, Bhagwandien R, Wijrdeman HK, Bakker CJG, “Analysis and correction of geometric distortions in 1.5 T magnetic resonance images for use in radiotherapy treatment planning,” *Phys Med Biol.* **40**, 1651-1654 (1995).

This chapter has been submitted as:

van den Bosch MR, de Leeuw H, Zwanenburg JJM, Lagendijk JJW, Moerland MA, "Single shot MR tagging to quantify local tissue deformation during MRI-guided needle interventions: a feasibility study," *Med Phys.* (2010).

Single shot MR tagging to quantify local tissue deformation during MRI-guided needle interventions: a feasibility study

6

Abstract

Introduction: In MRI-guided needle interventions, such as prostate biopsies and brachytherapy, tissue deformation caused by needle movement may result in localization errors and thus hamper the outcome of the procedure. Monitoring the local tissue deformation provides the ability to compensate for it, e.g. by increasing the needle insertion depth. Fast MR scans are useful to track the needle, but cannot be used to quantify local tissue deformation, in case anatomical landmarks are missing. Artificial landmarks can be created by MR tagging. This method provides a spatial saturation pattern (tag) in the tissue. Deformation of this pattern reflects the tissue motion between tag creation and tag imaging. As needle movement is non-periodic, k-space cannot be acquired with a multi-shot approach, like is done for cardiac imaging. Hence, a single shot MR tagging sequence is needed. In this study, the applicability of single shot MR tagging for MRI-guided needle interventions in phantom and volunteer experiments is shown.

Methods: Four different experiments were performed on a 1.5 T MR scanner: the first to quantify translations, the second to quantify rotations, the third to mimic a needle intervention, and the fourth to investigate the tag persistence in a volunteer. The tag pattern is created by a 1331 composite pulse. A balanced Steady State Free Precession sequence is used for imaging. To minimize undesired changes in contrast or sharpness of the tag pattern we chose a relatively small flip angle and a short imaging time.Scan parameters were: α = 20°, TE = 1.9 ms, TR = 3.7 ms, imaging time = 254 ms, read-out bandwidth = 887.8 Hz/voxel, read-out direction = F, field of view in sagittal orientation (FH x AP) = 352 x 270 mm^2, acquisition matrix = 352 x 68, slice thickness = 8 mm, number of signals averaged = 1, profile order = linear, tag spacing = 5 mm, tag delay = 100 ms, and trigger delay = 600 ms up to 3100ms. In all scans, head or surface coils were used for signal reception.

Results: In all experiments, the tag pattern was clearly visible and could be used to quantify the local tissue deformation caused by (needle) movement. Strong correlations between the imposed and measured (angular) phantom motions

were obtained. In the needle intervention experiment, the tag lines were perfectly horizontal in case without needle movement. With needle movement, tissue displacements up to 5 mm were observed. Volunteer's anatomy could be discriminated, despite the tag pattern. The tag pattern in the prostate could still be read in the tagging image with a trigger delay of 2.1 seconds. In structures with a longer T_1 value, such as the content of the bladder, the tag persistence was even longer.

Conclusion: This study demonstrates that single shot MR tagging can be used to quantify tissue deformation caused by needle movement. The *in vivo* tag persistence is sufficient to enable the application of the tagging sequence during MRI-guided needle interventions in patients.

6.1. Introduction

In MRI-guided needle interventions, such as prostate biopsies and brachytherapy, tissue deformation due to needle movement (insertion or retraction) may lead to localization errors and thus hamper the outcome of the procedure.

Lagerburg *et al.* reported unpredictable prostate translations and rotations caused by manual needle movement up to 22 mm and 14 degrees, respectively [1]. This implies the need for monitoring the tissue deformation during the intervention to provide the ability to compensate for the deformation, e.g. by increasing the needle insertion depth or by updating the dose plan. By tapping the needle, the tissue deformation caused by needle movement can be diminished [1,2], but even then, the ability to monitor tissue deformation during the intervention is valuable to ensure the quality of the needle tapping.

At our department, we built an MR-compatible robot to perform *in vivo* MRI-guided prostate inverventions [3]. It contains a tapping device to reduce the tissue deformation caused by needle movement [1,3,4]. Nevertheless, displacements of the prostate base up to 7 mm were measured in the first interventions [3]. Fast anatomical MR scans were useful to track the needle during insertion [3], but could not be used to quantify the local tissue deformation, due to the lack of anatomical landmarks.

Artificial landmarks for the quantification of tissue deformation can be created by MR tagging [5-7]. It provides a spatial saturation pattern (tag) by periodically modulating the longitudinal magnetization, resulting in a series of parallel lines or orthogonal grids in the MR image [5-8]. Deformations of the tags reflect the underlying motion of the saturated tissue in the period between the tag creation and the imaging.

MR tagging is commonly applied in cardiac MRI [5-8], where the heart contraction is periodic. By triggering, it is possible to create and image the tag pattern at identical time points in the cardiac cycle for all tagging acquisitions. This offers the ability to repeat the acquisitions and to fill k-space in a segmented fashion with only the MR signals recorded during a specific cardiac phase [5,6]. In MRI-guided interventions with non-repeating needle movements, it is not possible to obtain identical tissue geometries for each tagging acquisition and consequently to sample k-space in a segmented fashion.

The entire k-space must be filled using a single tagging sequence (single shot MR tagging).

In this study, we demonstrate the applicability of the single shot MR tagging for MRI-guided needle interventions in phantom and volunteer experiments.

6.2. Methods

6.2.1. Theoretical considerations

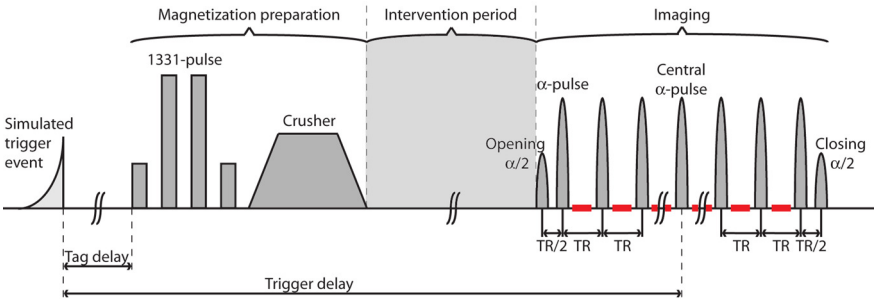

Figure 6.1. *Schematic overview of the proposed single shot tagging sequence. The red lines indicate the sample periods. Tag delay is defined as the time between the simulated trigger event and the application of the 1331-pulse, while the trigger delay determines the time between the trigger event and the center of the excitation pulse that samples the central line in k-space (k=0).*

Our single shot tagging sequence consists of two parts: one to create the tag pattern (magnetization preparation) and one to visualize this pattern (imaging), as illustrated by Figure 6.1. In the first part, the longitudinal magnetization (M_z) is spatially saturated using a 1331 composite pulse with a total flip angle of 90°. In the time period between the magnetization preparation and imaging (indicated as 'intervention period' in Figure 6.1), the longitudinal magnetization of the completely saturated spins returns to its original value ($M_{z,0}$) with the longitudinal relaxation time of the tissue (T_1), as described by equation 6.1:

$$M_z(t) = \left[1 - e^{-t/T1}\right] M_{z,0} \qquad (6.1)$$

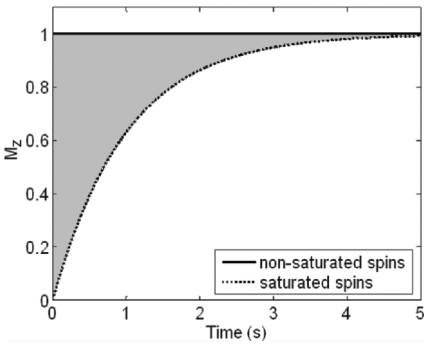

Figure 6.2. *Longitudinal magnetization in time after magnetization preparation, assuming T1=1000 ms and $M_{z,0}$ =1. The difference in longitudinal magnetization between the non-saturated and saturated spins is shaded in grey.*

As a result, the spatial fluctuations in amplitude of the longitudinal magnetization (difference between non-saturated and saturated spins) created by the tagging pulse, decrease with time (t) during the intervention period, as shown in Figure 6.2.

The imaging is based on a balanced Steady State Free Precession (bSSFP) sequence. This sequence type is fast and provides, in combination with tagging, a high tag contrast-to-noise ratio (CNR) [5,8-11]. Its train of RF-pulses, with identical flip angle (α) but altering angle sign, is preceded by an $\alpha/2$-pulse to ensure the transverse magnetization magnitude ($M_{\perp}$) of in-phase spins (spins that have a phase of 0° after a +α pulse) smoothly approaches a steady state value ($M_{\perp,ss}$) [8-10].

The transverse magnetization steady state value of the non-saturated spins as well as the saturated spins can be described by the following equation [5,10]:

$$M_{\perp,ss} = \frac{M_{z,0}(1-E_1)\sin\alpha\sqrt{E_2}}{1-(E_1-E_2)\cos\alpha-E_1E_2} \qquad (6.2)$$

where TR is the repetition time of the imaging sequence, T_2 represents the transversal relaxation time of the tissue, $E_1 = e^{-TR/T1}$ and $E_2 = e^{-TR/T2}$.

As derived by Scheffler *et al.* [10], both the $M_{\perp}$ decay of the non-saturated spins and $M_{\perp}$ growth of the saturated spins towards the steady state value can be approximated by equation 6.3:

$$M_{\perp}(n) = \left[M_{z,i}\, sin(\alpha/2) - M_{\perp,ss}\right]\lambda^n + M_{\perp,ss} \tag{6.3}$$

where n equals the excitation pulse number, $M_{z,i}$ represents the initial longitudinal magnetization at start of imaging, and λ is a rate parameter:

$$\lambda = E_2\, sin^2(\alpha/2) + E_1\, cos^2(\alpha/2) \tag{6.4}$$

The smaller λ, the faster the steady state value is approached. Provided that $n = t/TR$, it can be seen that the rate parameter λ is a weighted average between pure T_1-decay ($\alpha = 0^\circ$) and the faster T_2-decay ($\alpha = 180^\circ$). In general, λ decreases with increasing flip angle. Furthermore, λ is smaller for lower T_1 and T_2 values.

The tag contrast, which is defined as the transverse magnitude difference between non-saturated and completely saturated spins, can be derived from equation 6.3, resulting in equation 6.5. It shows that the maximum initial tag contrast is obtained when $\alpha = 180^\circ$. The closer to steady state, the smaller the tag contrast.

$$Tag\_contrast(n) = \left[\left(\underbrace{M_{z,i}}_{non\_sat} - \underbrace{M_{z,i}}_{sat}\right) sin(\alpha/2)\right]\lambda^n \tag{6.5}$$

As illustration, both $M_{\perp}$ and the tag contrast are plotted against time for different values of α, T_1 and T_2, in Figure 6.3. Increasing the flip angle results in a larger initial tag contrast, as well as a faster approach to $M_{\perp,ss}$, and consequently a faster decay of the tag contrast.

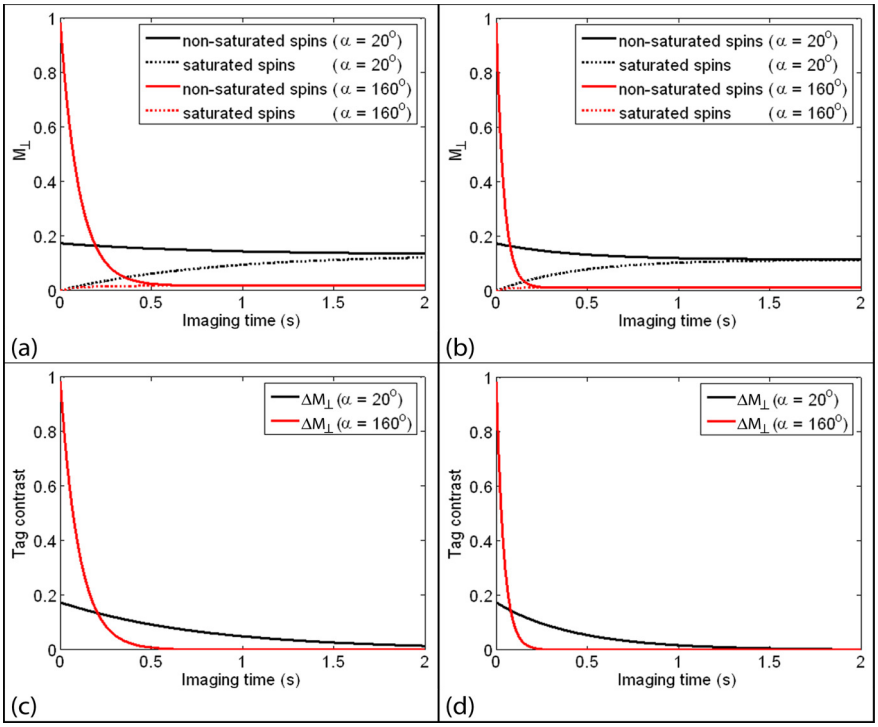

Figure 6.3. *Transverse magnetization magnitude in time for the flip angles 20° and 160°, assuming the imaging takes place directly after magnetization preparation, $M_{z,0}$ = 1, n = t / TR, TR = 4 ms, (a) T1 = 1000 ms and T2 = 100 ms, (b) T1 = 600 ms and T2 = 40 ms (c-d) corresponding tag contrast.*

In the single shot MR tagging sequence, the entire k-space is filled during the $M_\perp$ decay of the non-saturated spins and $M_\perp$ growth of the saturated spins towards the steady state value. These temporal modulations of $M_\perp$ lead to a weighting in k-space and affect the image quality by filtering in the phase encoding direction.

In general, the central k-lines that are dominated by low spatial frequencies are responsible for the image contrast information, while the outer lines of k-space with high spatial frequencies account for the image detail. Starting with the higher $M_\perp$ values at the central line of k-space and moving to the outer lines of k-space in an alternating fashion (profile order: low-high) will result in a reduction of the image detail (blurring). Starting at the outer k-space line (e.g. the profile order: linear) will result in less image contrast. Figure 6.4 illustrates these filtering effects and demonstrates that they can be reduced by minimizing the temporal modulations of $M_\perp$ (for example by applying low flip angles).

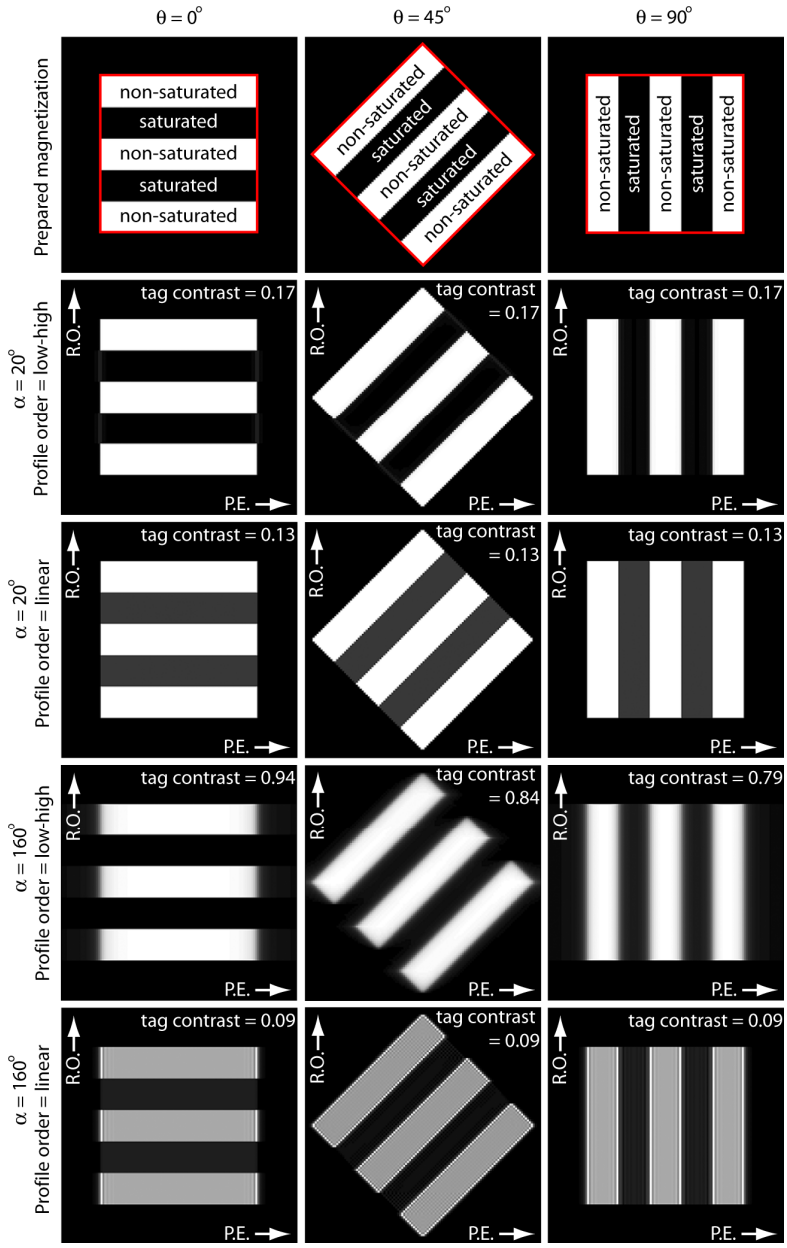

Figure 6.4. *Simulated tagging images for different flip angles and profile orders in k-space, assuming the imaging was performed directly after magnetization preparation with $M_{z,0}$ = 1, TR = 4 ms, acquisition matrix = 120 x120, and that the tag pattern can be described by a block pattern with a tag spacing of 16 pixels. The abbreviation R.O. stands for read-out, while P.E. means phase encoding. The tag contrast is determined using the central voxels of the non-saturated and saturated areas.*

6.2.2. Experiments

Four different experiments were performed on a 1.5 T MR scanner (Achieva, Philips Healthcare, Best, The Netherlands): the first to quantify translations, the second to quantify rotations, the third to mimic a needle intervention, and the fourth to investigate the tag persistence in a volunteer.

6.2.2.1. Experimental set-up

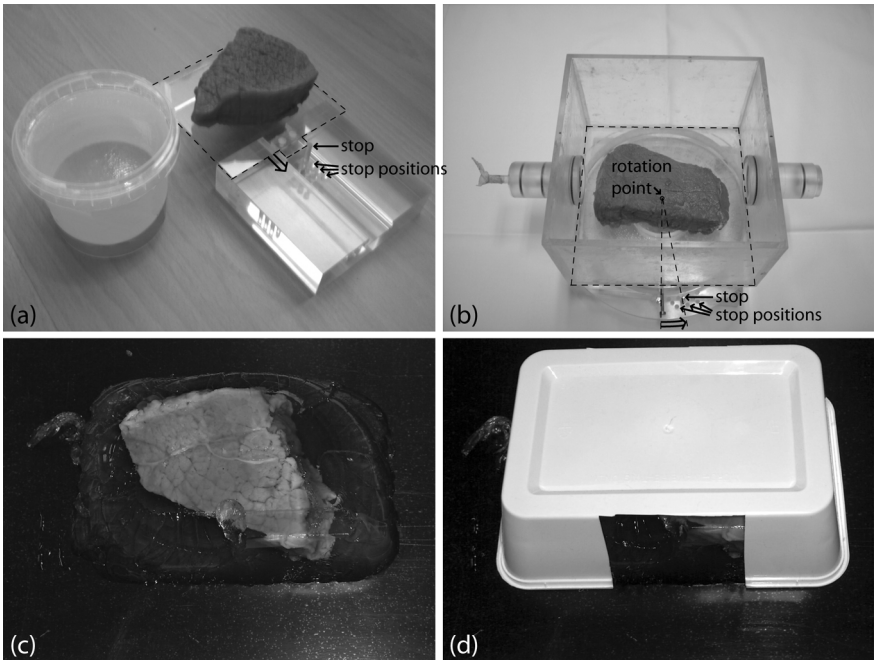

Figure 6.5. *(a) translation phantom, (b) rotation phantom, (c) needle intervention phantom without plastic cover, (d) needle intervention phantom with plastic cover.*

In the first experiment, a steak was placed on a plastic plateau that was manually translated (see Figure 6.5a) in the intervention period. As reference, a plastic cylinder filled with gelatin was positioned next to this translation phantom. The imposed movement of the steak was restricted by a mechanical stop (plastic pin) and ranged from 2 to 12 mm with an increment of 2 mm. By

the sound produced by the MR scanner during the tag pattern creation, the end of this period and consequently the start of the intervention period (see Figure 6.1) was detected by ear in the scanning room. In the intervention period the steak was translated. In the acquired tagging images, the centers of eight tag lines were manually selected. The absolute differences between the corresponding lines in the steak and reference phantom were calculated. The mean displacement was plotted against the imposed displacement.

Next, a steak was placed in a plastic box (see Figure 6.5b) that could be rotated in the intervention period. The imposed rotation of the steak was restricted by a mechanical stop (plastic pin) and ranged from 2 to 20° with an increment of 2°. In the generated tagging images, two points situated on the tag line were manually selected for eight different tag lines. Using these points, the angular orientations of the tag lines were determined. The mean rotation was plotted against the imposed rotation.

In the third experiment, a 14 G titanium needle of a biopsy gun (Invivo, Schwerin, Germany) was inserted approximately parallel to the static magnetic field into a steak that was enclosed by gelatin and fixated by a plastic cover (see Figure 6.5c and 6.5d). The openings at both long sides of the cover, allowed needle insertion and local phantom deformation, while the plastic cover prevented the gelatin edges of the phantom from moving. Afterwards, the needle was manually retracted. Tagging images were acquired to visualize tissue deformations during needle movement (insertion and retraction).

In the last experiment, a volunteer was placed in supine position on the MR table. Tagging sequences with different trigger delays were applied to investigate the tag contrast and persistence in a human anatomy.

6.2.2.2. MR sequences

The tag pattern was created by a 1331 composite pulse with a total flip angle of 90° followed by a crusher to destroy any residual transverse magnetizations. The total duration of the magnetization preparation was 4 ms.

To minimize the transverse magnetization modulation during the sampling of k-space and consequently diminish the filtering effects, we chose a relatively small flip angle (but large enough to get adequate signal) and short imaging

time. The latter was achieved by reducing the number of phase encoding steps and TR. An advantage of using a short TR and consequently a short TE, is that the susceptibility image artefact induced by the needle is less prominent [9]. Furthermore, the read-out gradient strength is high, due to the short TR, which minimizes the geometric image distortions caused by the needle [12,13].

Scan parameters were: α = 20°, TE = 1.9 ms, TR = 3.7 ms, imaging time = 254 ms, read-out bandwidth = 887.8 Hz/voxel, read-out direction = F, field of view in sagittal orientation (FH x AP) = 352 x 270 mm^2, acquisition matrix = 352 x 68, slice thickness = 8 mm, number of signals averaged (NSA) = 1, profile order = linear, tag spacing = 5 mm, tag delay = 100 ms, and trigger delay = 600 ms. In the last experiment, the trigger delay ranged from 600 ms to 3100 ms with increment of 500 ms. In the first experiment a SENSE-Head-8 coil (Philips Healthcare, Best, The Netherlands) was applied for signal reception, in the other experiments a SENSE Flex-L (Philips Healthcare, Best, The Netherlands) coil was used.

6.3. Results

Figure 6.6 illustrates the results of the displacement experiment. Figures 6.6a-6.6c show the tag patterns after a steak displacement of 0, 6 and 12 mm, respectively. The straight horizontal lines in both gelatin and steak confirm that only translation was imposed on the steak. Due to the non-uniform signal intensity, the tag lines in the heterogeneous steak phantom are harder to discriminate. The white lines in these subfigures indicate corresponding tag lines in the gelatin and steak. The graph in Figure 6.6d illustrates the good agreement between the measured and imposed displacements.

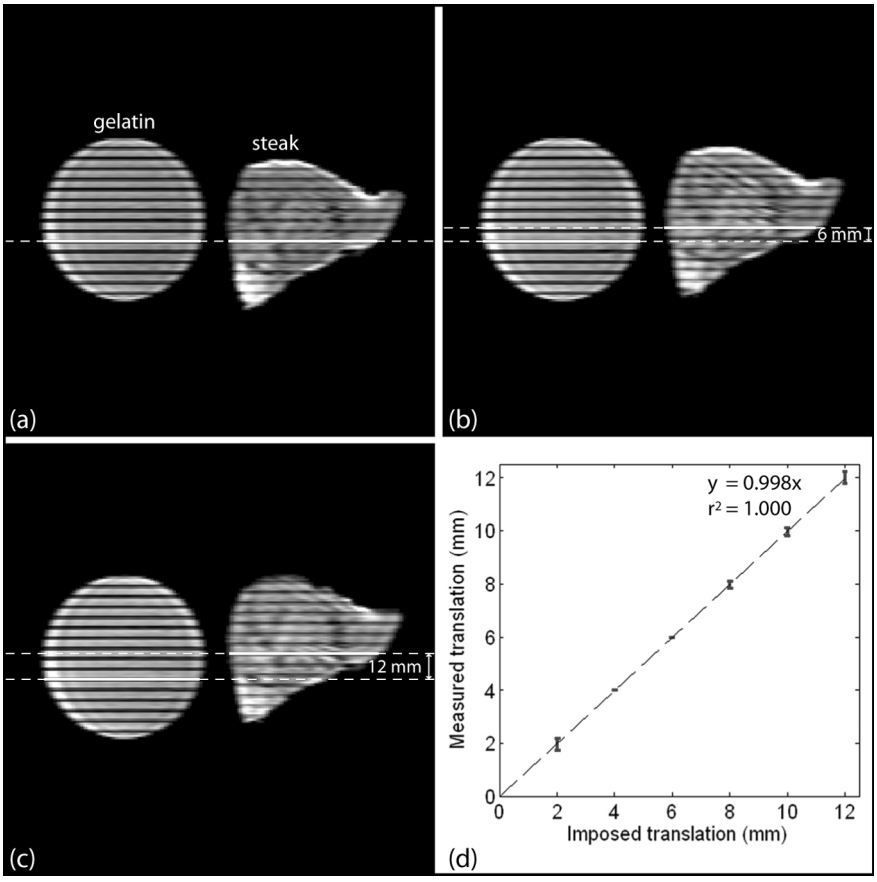

Figure 6.6. *Tag pattern after steak displacement of (a) 0 mm, (b) 6 mm, and (c) 12 mm. The white lines indicate corresponding tag lines. (d) Scatter plot of the measured and imposed displacements. The error bar represents the 95% confidence interval (twice the standard deviation).*

The angular orientations of the tag lines, after phantom rotation, are illustrated in the figures 6.7a-6.7c. These figures show the tag patterns after a steak rotation of 0°, 10° and 20°, respectively. At the steak edge banding artefacts are visible. There is a strong correlation between the measured and the imposed rotation as shown in Figure 6.7d.

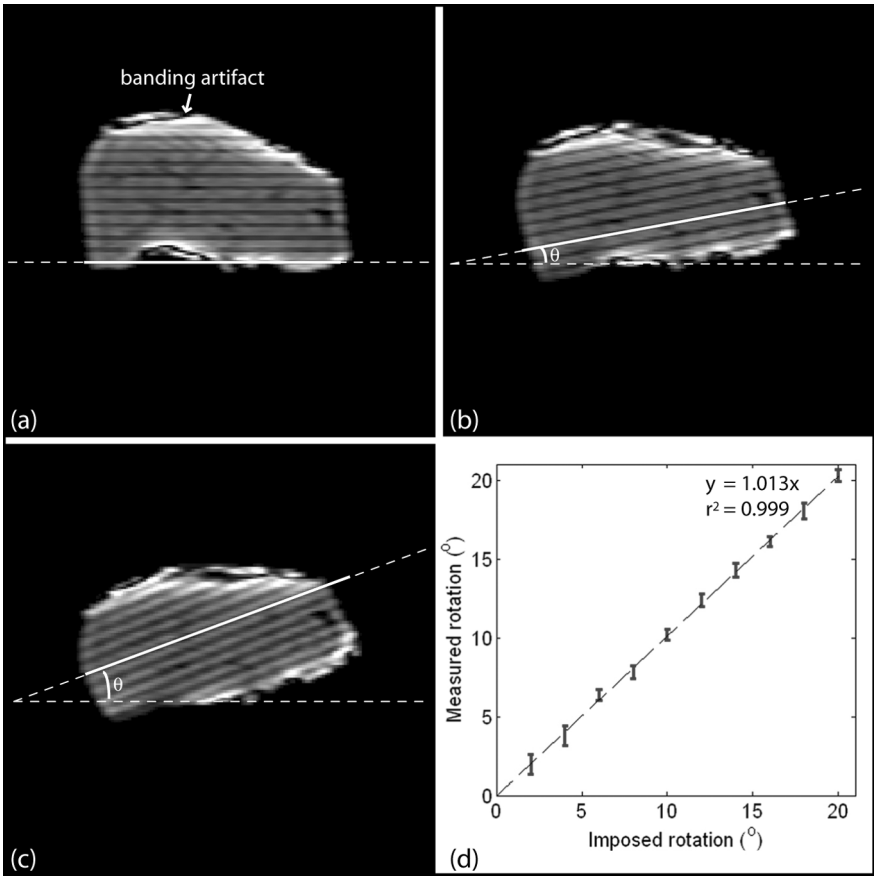

Figure 6.7. *Tag pattern after steak rotation of (a) 0°, (b) 10°, and (c) 20°. (d) Scatter plot of the measured and imposed rotations. The error bar represents the 95% confidence interval (twice the standard deviation).*

In Figure 6.8 the results of the needle intervention experiment are shown. The needle can be discriminated due to its signal intensity artefact. Without needle movement, the tag lines are perfectly horizontal (see Figure 6.8a). The tag lines are curved in case of needle movement (see Figure 6.8b and 6.8c), which implies that the phantom locally deforms during needle insertion and retraction. Taking the tag pattern at the phantom edge as reference, the tissue displacement at the needle tip is 5 mm and 4 mm for needle insertion and retraction, respectively. In this figure banding and ghosting artefacts are visible.

Figure 6.9 shows the tag pattern in a volunteer for different trigger delays. Especially in the bladder, deformations of the tag lines are observed. The tag contrast decreases with the trigger delay. This degradation is generally larger in areas with a smaller T_1-value.

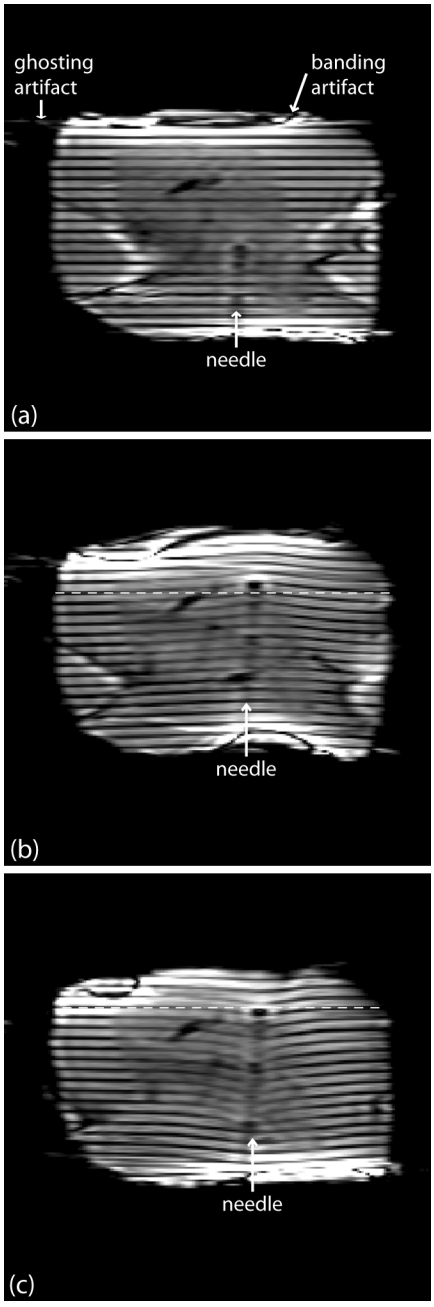

Figure 6.8. *Tag pattern (a) with 14 G titanium needle situated in the steak, (b) during needle insertion and (c) during needle retraction. The dashed line mimics an undeformed tagging line (reference).*

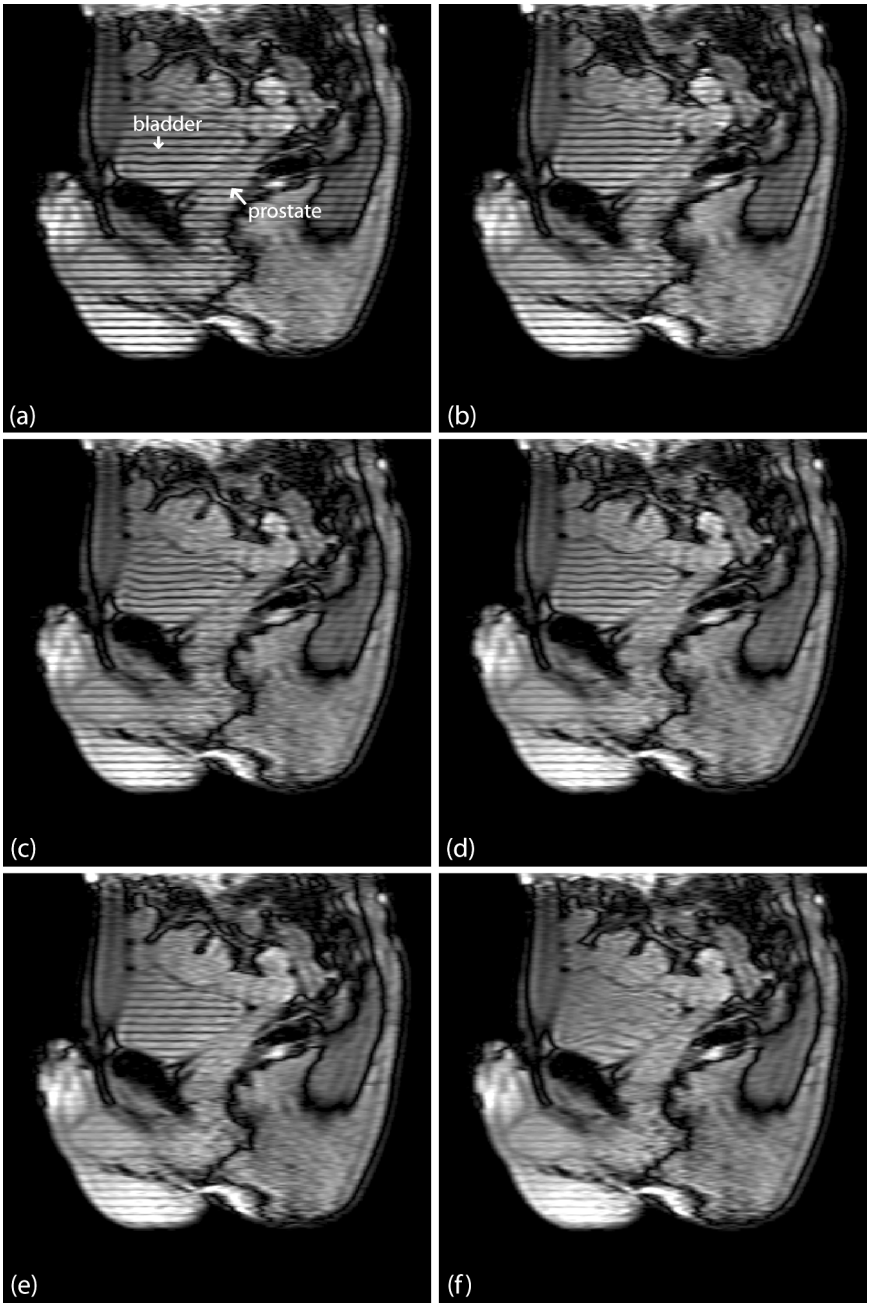

Figure 6.9. *Tagging images of the pelvic area of the volunteer when the tag delay was 100 ms and the trigger delay was (a) 600 ms, (b) 1100 ms, (c) 1600 ms, (d) 2100 ms, (e) 2600 ms, and (f) 3100 ms.*

6.4. Discussion

In the phantom and volunteer experiments, the tag pattern was clearly visible and could be used to quantify the local tissue deformation caused by (needle) movement. Knowing the local deformation provides the ability to compensate for it, e.g. by increasing the needle insertion depth.

The strong correlations between the imposed and measured (angular) phantom motions demonstrate that our single shot tagging sequence can be applied to quantify translations and rotations (see Figure 6.6 and 6.7).

In the tagging images, the intervention needle can be distinguished due to its signal artefact [3,14,15], as illustrated by Figure 6.8. Furthermore, this figure demonstrates that the presence of the needle does not distort the tag pattern (lines remain horizontal). In the needle intervention experiment, tissue displacements up to 5 mm and 4 mm were observed close to the needle tip during needle insertion and retraction, respectively. This implies that, in case of tumour biopsies, the tumour tissue might not yet have been reached at the moment of tissue collection. In case of an intervention, where particles are delivered inside a human structure during needle retraction, such as fiducial gold marker implantation or low-dose rate brachytherapy, tissue deformation results in a placement error with respect to the planning. The quantified local tissue deformation can be used to improve the outcome of the intervention, e.g. by adjusting the needle position or updating the dose plan.

As shown in Figure 6.9 it is possible to discriminate volunteer's anatomy, despite the tag pattern. The tag pattern in the prostate could still be read in the tagging image with a trigger delay of 2.1 seconds. In structures with a longer T_1 value, such as the content of the bladder, the tag persistence is even longer.

As illustrated by Figures 6.7 and 6.8, banding and ghosting artefacts are distinguishable in the tagging images, but they do not influence the results. Banding artefacts are typical for bSSFP images and are caused by local magnetic field distortions [9], for example due to air-tissue interfaces. Ghosting artefacts are caused by out-of-phase spins [8], probably due to inadequate shimming or fatty tissue, and appear in the phase-encoding direction. Ghosting artefacts from fatty tissue can be reduced by applying fat suppression or by replacing the startup $\alpha/2$-pulse by pulses with linearly increasing startup flip angles [8].

Because of the air gap between the steak and gelatin structure in Figure 6.7, it is hard to directly link the tag lines in these structures without prior knowledge of the imposed translation or the use of the contour displacement. Fortunately, for *in vivo* measurements no human structure is completely surrounded by air, implying there will always be a transition area as for example shown in the needle intervention experiment (see Figure 6.8).

The use of higher flip angles results in a higher initial tag contrast, but also in a faster tag contrast decay (and thus more filtering effects) compared to lower flip angles. Therefore, the flip angle was small in this study to diminish the filtering effects in all tissue types. Nevertheless, the amount of filtering also depends on the T_1 and T_2 values of the tissue (as shown in Figure 6.3). In the tissues with longer T_1 and T_2 values, the filtering is less prominent. Higher flip angles are allowed in these cases, resulting in a better tag contrast in the concerning tissues. A better tag contrast will permit a longer intervention period. The single shot tagging sequence may be optimized for different tissue types and k-space filling schemes. Furthermore, the filtering effects may be eliminated using a train of RF excitation pulses with ramped flip angles during imaging, as described by Ibrahim *et al.* [5].

To successfully monitor tissue deformations in *in vivo* MRI-guided needle interventions using MR tagging, the needle movement should be established in the intervention period (time period after the tag creation and before visualization). In the scanning room, it is possible to hear the end of tag creation and thus the start of the intervention period, which can be used as a trigger for manual interventions. In case robotic devices are applied, needle insertion can be triggered by the simulated event pulse of the scanner.

Since the *in vivo* tag persistence is adequate and the intervention needle can be discriminated in a tagging image (see Figure 6.8), the single shot tagging sequence is in principle applicable to monitor both the local tissue deformations and the needle displacement during *in vivo* MRI-guided needle interventions.

The single shot tagging sequence can be applied to improve needle interventions (e.g. by increasing the needle insertion depth or updating the dose plan) or as a quantitative method to compare the effect of different needle insertion techniques, such as needle tapping [1] and axial needle rotation [16]. Furthermore, it can be used in the quality assurance of robotic devices that insert a needle into the patient [3,17].

In addition to MRI-guided needle interventions, the sequence might be useful to monitor tissue deformation in other non-repeating processes or in cases where the structure motion is irregular and therefore hard to trigger. It can also be valuable in periodic processes, such as respiratory liver motion, since this single shot MR tagging sequence is fast with respect to the original sequences that fill the k-space in a segmented fashion.

6.5. Conclusion

This study demonstrates that single shot MR tagging can be used to quantify tissue deformation caused by non-repeating processes, such as a needle intervention. In the tagging images, it is possible to discriminate different tissue types and the needle. The *in vivo* tag persistence is sufficient to enable the application of the tagging sequence during MRI-guided needle interventions in patients. In the future, we want to further optimize the sequence for different tissue types and use it in the *in vivo* experiments with our robotic device for prostate interventions.

References

[1] Lagerburg V, Moerland MA, van Vulpen M, Lagendijk JJW, "A new robotic needle insertion method to minimise attendant prostate motion," *Radiother Oncol.* **80**, 73-77 (2006).

[2] Lagerburg V, Moerland MA, Lagendijk JJW, Battermann JJ, "Measurement of prostate rotation during insertion of needles for brachytherapy," *Radiother Oncol.* **77**, 318–323 (2005).

[3] van den Bosch MR, Moman MR, van Vulpen M, Battermann JJ, Duiveman E, van Schelven LJ, de Leeuw H, Lagendijk JJW, Moerland MA, "MRI-guided robotic system for transperineal prostate interventions: proof of principle," *Phys Med Biol.* **55**, 133-140 (2010).

[4] Lagerburg V, Moerland MA, Konings MK, van de Vosse RE, Lagendijk JJW, Battermann JJ, "Development of a tapping device: a new needle insertion method for prostate brachytherapy," *Phys Med Biol.* **51**, 891-902 (2006).

[5] Ibrahim el-SH, Stuber M, Schär M, Osman NF, "Improved myocardial tagging contrast in cine balanced SSFP images," *J Magn Reson Imaging.* **24**, 1159-1167 (2006).

[6] Markl M, Reeder SB, Chan FP, Alley MT, Herfkens RJ, Pelc NJ, "Steady-state free precession MR imaging: improved myocardial tag persistence and signal-to-noise ratio for analysis of myocardial motion," *Radiology.* **230**, 852-861 (2004).

[7] Shehata ML, Cheng S, Osman NF, Bluemke DA, Lima JA, "Myocardial tissue tagging with cardiovascular magnetic resonance," *J Cardiovasc Magn Reson.* **11**:55 (2009).

[8] Zwanenburg JJM, Kuijer JPA, Marcus JT, Heethaar RM, "Steady-state free precession with myocardial tagging: CSPAMM in a single breathhold," *Magn Reson Med.* **49**, 722-730 (2003).

[9] Scheffler K, Lehnhardt S, "Principles and applications of balanced SSFP techniques," *Eur Radiol.* **13**, 2409-2418 (2003).

[10] Scheffler K, "On the transient phase of balanced SSFP sequences," *Magn Reson Med.* **49**, 781-783 (2003).

[11] Herzka DA, Guttman MA, McVeigh ER, "Myocardial tagging with SSFP," *Magn Reson Med.* **49**, 329-340 (2003).

[12] Bakker CJG, Moerland MA, Bhagwandien R, Beersma R, "Analysis of machine-dependent and object-induced geometric distortion in 2DFT MR imaging," *Magn Reson Imaging.* **10**, 597-608 (1992).

[13] Port JD, Pomper MG, "Quantification and minimization of magnetic susceptibility artifacts on GRE images," *J Comput Assist Tomogr.* **24**, 958-964 (2000).

[14] Lagerburg V, Moerland MA, Seppenwoolde JH, Lagendijk JJW, "Simulation of the artefact of an iodine seed placed at the needle tip in MRI-guided prostate brachytherapy," *Phys Med Biol.* **53**, 59-67 (2008).

[15] Müller-Bierl B, Graf H, Lauer U, Steidle G, Schick F, “Numerical modeling of needle tip artifacts in MR gradient echo imaging,” *Med Phys.* **31**, 579-587 (2004).

[16] Abolhassani N, Patel R, Moallem M, “Control of soft tissue deformation during robotic needle insertion,” *Minim Invasive Ther Allied Technol.* **15**, 165-176 (2006).

[17] Muntener M, Patriciu A, Petrisor D, Schär M, Ursu D, Song DY, Stoianovici D, “Transperineal prostate intervention: robot for fully automated MR imaging-system description and proof of principle in a canine model,” *Radiology.* **247**, 543-549 (2008).

Summary and general discussion

7

Magnetic resonance imaging (MRI) visualizes anatomical soft tissue structures and tumour suspicious regions better than other image modalities, such as ultrasound (US), cone-beam computed tomography (CT) and portal imaging, implying that online MRI would be valuable in the diagnostic and treatment techniques for prostate cancer. Multiple institutes intend to perform or are performing MRI-guided biopsies, brachytherapy and new treatment techniques, such as cryoablation, radiofrequency (RF) ablation and high intensity focussed ultrasound (HIFU) [1-6].

Since the access to the patient is limited due to the MR bore, robotic devices are needed to achieve accurate needle (or transducer) placement under real-time MR guidance. Several robotic devices have been built to automatically align the needle or even automatically insert the needle inside the MR scanner [7-14]. All these systems have to deal with technical difficulties, such as the restriction to use solely non-ferromagnetic materials, the needle-induced prostate deformation, image artefacts caused by the robotic device and needle, and undesired tissue heating around the needle tip due to the resonating RF waves that are needed to generate an MR image.

This thesis describes the clinical introduction of the University Medical Center Utrecht (UMCU) robot dedicated for MRI-guided needle interventions in the prostate. The robot consists of polymers and non-ferromagnetic materials, such as copper, titanium, brass and aluminium. It contains a tapping device to automatically tap the needle stepwise towards the prostate using a remote control outside the scanning room. By tapping the needle, tissue deformation is reduced with respect to manual insertion [15]. In the time periods between each tap the needle trajectory can be verified using fast MR images and abnormalities with respect to the planning (e.g. needle deflection or critical structure movement into the desired needle trajectory) can be detected in time [14]. The robot has five degrees of freedom: four passive and one active, which is the needle insertion. The prostate accessibility is ensured using a rotation point just underneath the skin of patient's perineum and a divergent needle insertion method [16,17].

In Chapter 2, the results are presented of a feasibility study on the dose coverage in low-dose rate (LDR) brachytherapy using divergent needle insertion methods, as could theoretically be established inside the MR scanner applying the UMCU robot. In LDR brachytherapy, the prostate is irradiated by seeds with low activity, which are delivered inside the prostate using needles. The seeds remain in the prostate permanently and their activities decrease in time.

The study was based on 10 patient MRI datasets. For every patient the prostate, rectum, bladder and urethra were delineated on the abdomen MR scan. Optimal dose distributions were generated using our own developed inverse planning software, based on inverse planning by simulated annealing (IPSA) [18-20]. It used hard dose constraints to distinguish between useful and unacceptable dose distributions and soft dose constraints for balancing one dose constraint against another to get the optimal dose distribution. Adequate dose coverage and uniformity were accomplished inside the prostate, while the urethra and rectum were spared sufficiently.

The study revealed that the dose distributions of the divergent needle insertion methods were comparable with the ones of the current parallel needle insertion method. This result is in agreement with Fu *et al.*, who performed a planning study for LDR brachytherapy based on US images and an anatomical model [21].

Since MRI visualizes (in contradiction to US) critical structures, such as neurovascular bundles and penile bulb, the number of needles that pierce these critical structures may determine the insertion method of choice.

In general, the dose distributions may be further improved by increasing the accessible prostate volume, by reducing the diameter of the urethra catheter or by enlarging the distance between the two lateral rotation points when used. Furthermore, better dose distributions may be obtained by increasing the number of seed positions inside the prostate.

Chapter 2 also showed that in case the planning target volume (PTV) surrounds the prostate with a 3 mm margin as recommended by Salembier *et al.* [22], it is necessary to place the seeds partly outside the prostate to achieve an adequate dose coverage.

Cunha *et al.* reported that divergent needle insertion methods could also be applied to establish adequate dose distributions in high dose rate (HDR) brachytherapy [23]. In HDR brachytherapy, a single source with high activity is

attached to the tip of a drive wire that can be positioned at different depths in all catheters placed in the prostate. By varying the time that the source dwells at various positions in each catheter, the dose to the prostate including tumour can be shaped. The total dose is given in multiple fractions. Since this brachytherapy modality does not require seed delivery in the prostate but only adequate needle positioning, MRI-guided HDR brachytherapy is principally simpler to perform than MRI-guided LDR brachytherapy.

Chapter 3 describes a new method to detect undesired situations with risk of tissue heating at the needle tip caused by RF waves.

Elongated conductive structures, such as vascular guidewires, catheters, and intervention needles, can interact with the electromagnetic RF field resulting in tissue heating at the structure tip [24-27]. The strength of the field interaction correlates with the induced current inside the structure, which in turn is related to the tissue heating at the tip [28,29]. In case the RF waves can resonate along the structure, large temperature rises over 35 degrees Celsius were reported in phantom experiments with long conductive wires [24,25]. Since it is hard to predict the exact length at which resonance occurs under *in vivo* conditions, there is a need for methods to investigate or if necessary to monitor this resonance behaviour.

Our method quantifies the induced current inside the structure. Several spoiled gradient echo images with different nominal flip angle settings are acquired to map the field interaction. From the field map, the induced current can be extracted by fitting an analytical model.

Two phantom experiments were performed: one with a short needle placed centrally in the bore of a 3T MR scanner and one with a longer wire positioned in an off-center position to mimic a worst case scenario for the patient. Both structures were inserted parallel to the static magnetic field at multiple depths. A fiberoptic temperature sensor was positioned at the structure tip to record the temperature.

The study revealed that it is possible to quantify the induced current using the constructed field map at a radius between 7 and 10 mm from the structure. The wave pattern of the current profile could be derived using this method. In the long wire the induced current was much higher than in the needle. Main causes were the off-center position of the wire and the larger length of the wire. Only

in the second experiment a temperature rise was detected (2.4°C in 1 min). The observation in the first experiment that the induced current could be determined in cases without tissue temperature increase suggests that our method is a very sensitive method to investigate resonance behaviour.

For structures placed under an angle, the method is expected to be applicable when keeping the fit planes perpendicular to the structure. In these cases, signal correction for the susceptibility artefact might be needed because this artefact will no longer be confined to the tip of the structure [30].

Independent measurement of the RF induced currents are necessary for further validation of our method and may be possible in near future with recently developed sensors [29,31].

The exact resonance conditions on the structures are generally difficult to simulate, but can be characterized using the current profiles derived by our method. It was shown for elongated structures inserted in a phantom, but it is also applicable *in vivo*. The method can be used to monitor the resonance behaviour and to investigate for instance the effect of needle coating on the resonance length. The next step is to determine the specific absorption rate (which is a measure for the tissue heating) at the needle tip from the current profiles.

In Chapter 4, development considerations and quality assurance methods of MRI-guided robotic devices dedicated for needle interventions are listed.

For the design of the robot, the available space inside an MR scanner is important. Closed bore and open MR scanners provide different accessibility to the patient. Higher field strengths are available for closed bore MR scanners, resulting in better image quality [32]. Furthermore, alignment of the intervention needle along the direction of the static magnetic field is more logical in a closed bore MR scanner. For this needle orientation, the susceptibility artefact caused by the needle is confined to the tip of the needle in the MR image [30]. However, there are also disadvantages of using high field strengths for robotic interventions. The main disadvantages are: increased static field distortions and signal intensity artefacts caused by the robot and the needle [32,33], and the wavelength reduction of the electromagnetic RF waves, which increase the risk of serious tissue heating around the intervention needle tip due to resonating RF waves along the needle [24,27].

The patient accessibility can be investigated using a planning study. For the MR compatibility of the robot and the performance of the robot inside a magnetic field, the robotic materials are important. In general, the use of ferromagnetic materials should be avoided. For the reduction of eddy currents that may hamper the performance of the robot, it is recommended to minimize conductive loop areas and to avoid conductive loops where possible [34-36]. However, eddy currents did not limit the performance of the UMCU robot that contains various conductive components in a 1.5 T magnetic field, which demonstrates that an MR compatible robotic device can also be made of conductive materials.

Geometric image distortions caused by static magnetic field perturbations (static field error) or non-linearity of the gradients (gradient error) may hamper the needle placement accuracy [37]. They can be quantified using a tube phantom. Static magnetic field perturbations induced by the UMCU robot decreased with distance from the robot: e.g. 16 parts per million (ppm) close to the robot to 5 ppm in the scanner isocenter. The geometric distortions due to these field perturbations can generally be minimized by increasing the readout gradient strength or by using robotic materials with a susceptibility close to that of human tissue, like polymers [37]. Gradient errors can be reduced by applying the geometric image correction provided by the software of the MR scanner. The differences in the gradient error between the situation with and without the robot present are negligible, except in the FH direction close to the robot (error increase <2 mm).

Also the susceptibility artefact at the tip of the needle makes the exact tip localization difficult. Although these artefacts are well understood and the underlying tip position can be reconstructed in tissue with known susceptibility [30], it is harder to estimate the exact needle tip location in heterogeneous human tissue with unidentified susceptibility. The uncertainty in the needle tip localization can be reduced by the use of needle materials closer to human tissue or by optimising the scan parameters, e.g. addition of an extra 180 degree refocusing pulse to compensate for static magnetic field inhomogeneities [30,33,38,39].

Tissue deformation during needle insertion might influence the placement accuracy. Several solutions to decrease the deformation are suggested, such as axial needle rotation [40], needle shooting [12] and needle tapping [41]. The UMCU robot uses the latter solution.

Needle deflection also hampers the placement accuracy and can be a safety hazard for the patient. In case of the UMCU robot, the deflection can be monitored in time using fast MR images and stepwise needle insertion. If necessary, the needle can be retracted for reinsertion.

The risk of tissue heating at the tip of the needle, due to resonating RF waves, can be estimated performing several phantom experiments that mimic worst-case scenarios. Mostly, the temperature at the tip of the needle is measured by fiberoptic temperature sensors [24-27,42]. The measured temperature is highly dependent on the location of the temperature sensor with respect to the tip, since the heating is deposited locally [43]. MR thermometry can generally also be applied to monitor tissue heating, but not close to the needle tip due to the susceptibility artefact [43]. The sensitive method based on RF induced image artefacts (see chapter 3 of this thesis) quantifies induced currents inside the needle to investigate the RF safety [42]. A new qualitative technique to estimate the safety risk is based on reversed RF polarization [44]. The last two methods are effective for detecting potentially dangerous situations non-invasively, although they do not measure the exact heat deposition at the needle tip.

Needle coating or the use of non-conductive needle materials can reduce or exclude the risk of tissue heating, respectively [27].

Chapter 5 reports the proof of principle of our robot. Four fiducial gold markers were placed under MR guidance inside the prostate of a prostate cancer patient using two parallel needle trajectories. The fiducial gold markers (with dimensions similar to brachytherapy seeds) were used for the prostate localization during external beam radiotherapy [45]. Since the target volume is the entire prostate, the exact location of the markers is not essential making this an ideal application to test our robot on patients.

The robot including the needle was manually aligned and the needle was manually pushed just beneath the skin of patient's perineum through one of the insertion points. MRI was applied to verify the needle trajectory, and to define target positions. The robot tapped the needle into the prostate under MRI guidance using a remote control outside the scanning room. When the target position was reached, the radiation oncologist manually placed a fiducial gold marker at this location.

In all MR scans, it was possible to discriminate patient's anatomy (e.g. prostate, rectum and pubic arch), the fiducial gold markers, and the needle. Real time imaging to track the needle during tapping could be established by frequently generating two orthogonal MR images within 5.2 s. From simulations and experiments the real needle tip was estimated to be approximately 5 mm proximal from the outer edge of the artefact in the acquired images of this study [30]. In the images signal artefacts caused by the robot were distinguishable, which indicated the presence of local magnetic field distortions [46]. These magnetic field distortions lead to geometric image distortions, but were minimized by the use of large read-out gradients and were negligible near the target position [37]. Despite the needle tapping, a prostate deformation up to 7 mm was measured, which suggests the need to improve the tapping device for further reduction of the deformation.

In Chapter 6, it is investigated whether it is possible to quantify local prostate deformations caused by the needle movement, by creating artificial landmarks in the prostate using single shot MR tagging. It provides a spatial saturation pattern (tag) that can be used to quantify tissue deformations in the period between tag creation and tag visualization. The method can be used to inspect the quality of the tapping of the UMCU robot, or, in general, to improve the outcome of the intervention, e.g. by adjusting the needle position or updating the dose plan, taking into account the deformation.

Our single shot MR tagging consisted of a 1331 composite pulse to create a tag line pattern and a balanced Steady State Free Precession sequence to visualize it after a predefined delay. The scan parameters were optimised to obtain adequate image quality in all experiments of this study. Four experiments were performed on a 1.5 T MR scanner: the first to quantify translations, the second to quantify rotations, the third to mimic a needle intervention, and the fourth to investigate the tag persistence in a volunteer.

In all experiments, the tag pattern was clearly visible. The strong correlations between the imposed and measured phantom motions demonstrated that our single shot tagging sequence can be applied to quantify translations and rotations. In the needle intervention experiment, tissue displacements up to 5 mm were observed. In case without needle movement the tag lines were perfectly horizontal, suggesting the presence of the needle did not distort the tag pattern. In the volunteer experiment, the tag pattern in the prostate could

still be read in the tagging image with a trigger delay of 2.1 seconds, while the tag persistence was even larger in structures with a longer T_1 value, such as the content of the bladder.

Banding and ghosting artefacts were distinguishable in the tagging images, but they did not influence the results. Ghosting artefacts from fatty tissue can be reduced by applying fat suppression or using linearly increasing startup flip angles in the imaging part [47]. Increasing the flip angle in case of tissues with longer T_1 and T_2 values might further optimise the tagging sequence.

In these experiments with manual needle insertion, the start of the intervention period was identified using the sound of the MR scanner. In case of robotic devices, the automated needle insertion can be triggered by the simulated event pulse of the scanner.

The single shot tagging sequence can be applied to improve needle interventions, e.g. by monitoring and if necessary adjusting the needle insertion depth, or as an investigative method to compare the effect of different needle insertion techniques on tissue deformation. The sequence might also be useful in other applications, for example to monitor tissue deformation due to respiratory movement.

The clinical introduction of the UMCU robot and the first clinical experiences with this robotic device are described in this thesis. Although the principles of the robotic devices of other institutes are different, our findings might be valuable for them to test, quantify and improve the performance of their robot or to safely introduce their robotic devices into the clinic.

The findings reported in this thesis can also be used to identify the strengths and weaknesses of the robotic devices described in the introduction of this thesis.

The manipulator described by Fischer *et al.* is compatible with a 3 T magnetic field [10,11]. The current version has limited degrees of freedom, which probably hampers the accessibility of the prostate. A modified system with more degrees of freedom has been designed [10]. Due to manual needle insertion, advanced needle insertion techniques to minimize tissue deformation are missing. The relatively short wavelengths of the electromagnetic RF field at 3 T require adequate investigation of the RF safety during the intervention (see chapter 3 of this thesis).

The robotic needle guide manipulator with its mechanical main body positioned above the head of the surgeon and two rigid arms reaching down into the surgical field [7], will result in negligible image artefacts. However, the open 0.5 T MR scanner lacks high image quality. Furthermore the intervention needle will generally be oriented perpendicularly to the static magnetic field, resulting in a susceptibility artefact along the entire needle [30]. The manipulator does not contain any advanced needle insertion technique (e.g tapping, shooting or axial needle rotation) to minimize tissue deformation during insertion.

Also the manipulator described by Schouten *et al.* is compatible with a 3 T magnetic field [8]. Since the robot is made of plastic, negligible image artefacts are expected. Due to the gadolinium-doped water reservoir, the automated positioning of the working channel can be monitored with real-time MR images. However, in the essential part of the procedure online MRI is lacking, since the needle insertion takes place outside the MR scanner. Any needle deflection, unexpected piercing of critical structures (e.g. bladder) or tissue deformation during insertion will not be detected. Furthermore, also this manipulator lacks any advanced needle insertion technique for the reduction of tissue deformation.

The robotic device, which is reported by Muntener *et al.* [12,13], has an advanced design with many active degrees of freedom and a specific needle insertion technique, namely shooting. Nevertheless, this system has not yet been introduced into the clinic, while it has already been tested successfully on canines in 2007 [12]. Probably, this is due to the needle insertion technique. Since the needle is shot to the target, there is no possibility to correct for any needle deflection, needle misalignment, unexpected piercing of critical structures (e.g. pubic bone) or tissue deformation during insertion.

The UMCU robot requires manual needle alignment, but enables stepwise needle insertion inside the MR scanner [14]. Online MRI during needle insertion is possible. The obtained images are of high quality and the needle can be tracked. The tapping device of the UMCU robot to minimize tissue deformation and the needle entrance rotation point to increase prostate accessibility make the robot unique. Currently, the tapping device is further improved to diminish tissue deformations. In the future, motors will be added to automatically steer the needle in the desired orientation.

To our knowledge, the UMCU robot is the first and up-to-now the only robotic device in the world that performed a needle insertion in patients inside an MR

scanner, while tracking the needle using online MRI. The possibility of tapping a needle under MRI guidance with the UMCU robot is a major step towards online MRI-guided prostate brachytherapy and biopsies.

The modified robot might also be applicable for new techniques as cryoablation, RF ablation and HIFU. The advantage of these techniques above brachytherapy is that the ablative area can be monitored with MRI, due to the direct change in tissue properties [5]. The disadvantage of these techniques is that the healthy tissue in the ablative area does not have the chance to recover, which makes e.g. the ablation of tumour cells adjacent to, for example, the urethra difficult. Furthermore, blood flow affects the local tissue temperature during the ablation, implying vessel modelling is mandatory for adequate planning and treatment [48].

The first applications of the modified UMCU robot will be prostate biopsies and HDR brachytherapy for focal salvage in patients with prostate recurrences. Both applications need adequate needle placement, but do not require any seed delivery, which makes the design of the new tapping device easier.

References

[1] Susil RC, Camphausen K, Choyke P, McVeigh ER, Gustafson GS, Ning H, Miller RW, Atalar E, Coleman CN, Ménard C, "System for prostate brachytherapy and biopsy in a standard 1.5 T MRI scanner," *Magn Reson Med.* **52**, 683-687 (2004).

[2] Ares C, Popowski Y, Pampallona S, Nouet P, Dipasquale G, Bieri S, Ozsoy O, Rouzaud M, Khan H, Miralbell R, "Hypofractionated boost with high-dose-rate brachytherapy and open magnetic resonance imaging-guided implants for locally aggressive prostate cancer: a sequential dose-escalation pilot study," *Int J Radiat Oncol Biol Phys.* **75**, 656-663 (2009).

[3] Woodrum DA, Gorny KR, Mynderse LA, Amrami KK, Felmlee JP, Bjarnason H, Garcia-Medina OI, McNichols RJ, Atwell TD, Callstrom MR, "Feasibility of 3.0T magnetic resonance imaging-guided laser ablation of a cadaveric prostate," *Urology.* **75**, 1514.e1-1514.e6 (2010).

[4] Engelhard K, Hollenbach HP, Kiefer B, Winkel A, Goeb K, Engehausen D, "Prostate biopsy in the supine position in a standard 1.5-T scanner under real time MR-imaging control using a MR-compatible endorectal biopsy device," *Eur Radiol.* **16**, 1237-1243 (2006).

[5] Josan S, Bouley DM, van den Bosch M, Daniel BL, Butts Pauly K, "MRI-guided cryoablation: In vivo assessment of focal canine prostate cryolesions," *J Magn Reson Imaging.* **30**, 169-176 (2009).

[6] Chopra R, Burtnyk M, N'djin WA, Bronskill M, "MRI-controlled transurethral ultrasound therapy for localised prostate cancer," *Int J Hyperthermia.* **26**, 804-821 (2010).

[7] DiMaio SP, Pieper S, Chinzei K, Hata N, Haker SJ, Kacher DF, Fichtinger G, Tempany CM, Kikinis R, "Robot-assisted needle placement in open MRI: system architecture, integration and validation," *Comput Aided Surg.* **12**, 15-24 (2007).

[8] Schouten MG, Ansems J, Renema WKJ, Bosboom D, Scheenen TWJ, Fütterer JJ, "The accuracy and safety aspects of a novel robotic needle guide manipulator to perform transrectal prostate biopsies," *Med Phys.* **37**, 4744-4750 (2010).

[9] Chinzei K, Hata N, Jolesz F, Kikinis R, "Surgical assist robot for the active navigation in the intraoperative MRI: Hardware design issues," *Proceedings of the IEEE/RSJ International Conference on Intelligent Robots and Systems*, Takamatsu, Japan, 727–732 (2000).

[10] Fischer GS, Iordachita I, Csoma C, Tokuda J, Dimaio SP, Tempany CM, Hata N, Fichtinger G, "MRI-Compatible Pneumatic Robot for Transperineal Prostate Needle Placement," *IEEE ASME Trans Mechatron.* **13**, 295-305 (2008).

[11] Fischer GS, DiMaio SP, Iordachita I, Fichtinger G, "Robotic Assistant for Transperineal Prostate Interventions in 3T Closed MRI," *Med Image Comput Comput Assist Interv.* **10**, 425-433 (2007).

[12] Muntener M, Patriciu A, Petrisor D, Schär M, Ursu D, Song DY, Stoianovici D, "Transperineal prostate intervention: robot for fully automated MR imaging-system description and proof of principle in a canine model," *Radiology.* **247**, 543-549 (2008).

[13] Muntener M, Patriciu A, Petrisor D, Mazilu D, Bagga H, Kavoussi L, Cleary K, Stoianovici D, "Magnetic resonance imaging compatible robotic system for fully automated brachytherapy seed placement," *Urology.* **68**, 1313-1317 (2006).

[14] van den Bosch MR, Moman MR, van Vulpen M, Battermann JJ, Duiveman E, van Schelven LJ, de Leeuw H, Lagendijk JJW, Moerland MA, "MRI-guided robotic system for transperineal prostate interventions: proof of principle," *Phys Med Biol.* **55**, 133-140. Feb 10 (2010).

[15] Lagerburg V, Moerland MA, van Vulpen M, Lagendijk JJW, "A new robotic needle insertion method to minimise attendant prostate motion," *Radiother Oncol.* **80**, 73-77 (2006).

[16] Van Gellekom MPR, Moerland MA, Battermann JJ, Lagendijk JJW, "MRI-guided prostate brachytherapy with single needle method-a planning study," *Radiother Oncol.* **71**, 327-332 (2004).

[17] van den Bosch MR, Lips IM, Lagerburg V, van Vulpen M, Lagendijk JJW, Moerland MA, "Feasibility of adequate dose coverage in permanent prostate brachytherapy using divergent needle insertion methods." *Radiother Oncol.* **86**, 120-125 (2008).

[18] Lessard E, Kwa SL, Pickett B, Roach M 3rd, Pouliot J, "Class solution for inversely planned permanent prostate implants to mimic an experienced dosimetrist," *Med Phys.* **33**, 2773-2282 (2006).

[19] Lessard E, Pouliot J, "Inverse planning anatomy-based dose optimization for HDR-brachytherapy of the prostate using fast simulated annealing algorithm and dedicated objective function," *Med Phys.* **28**, 773-779 (2001).

[20] Pouliot J, Tremblay D, Roy J, Filice S, "Optimization of permanent 125I prostate implants using fast simulated annealing," *Int J Radiat Oncol Biol Phys.* **36**, 711-720 (1996).

[21] Fu L, Ng WS, Liu H, O'Dell W, Rubens D, Strang J, Schell MC, Brasacchio R, Liao L, Messing E, Yu Y, "Bouquet brachytherapy: feasibility and optimization of conically spaced implants," *Brachytherapy.* **4**, 59-63 (2005).

[22] Salembier C, Lavagnini P, Nickers P, Mangili P, Rijnders A, Polo A, Venselaar J, Hoskin P; GEC ESTRO PROBATE Group, "Tumour and target volumes in permanent prostate brachytherapy: a supplement to the ESTRO/EAU/EORTC recommendations on prostate brachytherapy," *Radiother Oncol.* **83**, 3-10 (2007).

[23] Cunha JA, Hsu IC, Pouliot J, "Dosimetric equivalence of nonstandard HDR brachytherapy catheter patterns," *Med Phys.* **36**, 233-239 (2009).

[24] Dempsey MF, Condon B, Hadley DM, "Investigation of the factors responsible for burns during MRI," *J Magn Reson Imaging.* **13**, 627-631 (2001).

[25] Konings MK, Bartels LW, Smits HF, Bakker CJG, "Heating around intravascular guidewires by resonating RF waves," *J Magn Reson Imaging.* **12**, 79-85 (2000).

[26] Yeung CJ, Karmarkar P, McVeigh ER, "Minimizing RF heating of conducting wires in MRI," *Magn Reson Med.* **58**, 1028-1034 (2007).

[27] Yeung CJ, Susil RC, Atalar E, "RF safety of wires in interventional MRI: using a safety index," *Magn Reson Med.* **47**, 187-193 (2002).

[28] Nitz WR, Oppelt A, Renz W, Manke C, Lenhart M, Link J, "On the heating of linear conductive structures as guide wires and catheters in interventional MRI," *J Magn Reson Imaging.* **13**, 105-114 (2001).

[29] Nordbeck P, Weiss I, Ehses P, Ritter O, Warmuth M, Fidler F, Herold V, Jakob PM, Ladd ME, Quick HH, Bauer WR. "Measuring RF-induced currents inside implants: Impact of device configuration on MRI safety of cardiac pacemaker leads," *Magn Reson Med.* **61**, 570-578, (2009).

[30] Lagerburg V, Moerland MA, Seppenwoolde JH, Lagendijk JJW, "Simulation of the artefact of an iodine seed placed at the needle tip in MRI-guided prostate brachytherapy," *Phys Med Biol.* **53**, 59-67 (2008).

[31] Zanchi MG, Venook R, Pauly JM, Scott G, "An optically-coupled system for quantitative monitoring of MRI-induced RF currents into long conductors", *oral presentation at the ISMRM 16th scientific meeting & exhibition*, Toronto, Canada, 2008.

[32] Machann J, Schlemmer HP, Schick F, "Technical challenges and opportunities of whole-body magnetic resonance imaging at 3T," *Phys Med.* **24**, 63-70 (2008).

[33] Guermazi A, Miaux Y, Zaim S, Peterfy CG, White D, Genant HK, "Metallic artefacts in MR imaging: effects of main field orientation and strength," *Clin Radiol.* **58**, 322-328 (2003).

[34] Dempsey MF, Condon B, Hadley DM, "MRI safety review," *Semin Ultrasound CT MR.* **23**, 392-401 (2002).

[35] Graf H, Lauer UA, Schick F, "Eddy-current induction in extended metallic parts as a source of considerable torsional moment," *J Magn Reson Imaging.* **23**, 585-590 (2006).

[36] Robertson NM, Diaz-Gomez M, Condon B, "Estimation of torque on mechanical heart valves due to magnetic resonance imaging including an estimation of the significance of the Lenz effect using a computational model," *Phys Med Biol.* **45**, 3793-3807 (2000).

[37] Bakker CJG, Moerland MA, Bhagwandien R, Beersma R, "Analysis of machine-dependent and object-induced geometric distortion in 2DFT MR imaging," *Magn Reson Imaging.* **10**, 597-608 (1992).

[38] Müller-Bierl B, Graf H, Lauer U, Steidle G, Schick F, "Numerical modeling of needle tip artifacts in MR gradient echo imaging," *Med Phys.* **31**, 579-587 (2004).

[39] Port JD, Pomper MG, "Quantification and minimization of magnetic susceptibility artifacts on GRE images," *J Comput Assist Tomogr.* **24**, 958-964 (2000).

[40] Abolhassani N, Patel R, Moallem M, “Control of soft tissue deformation during robotic needle insertion,” *Minim Invasive Ther Allied Technol.* **15**, 165-176 (2006).

[41] Lagerburg V, Moerland MA, Konings MK, van de Vosse RE, Lagendijk JJW, Battermann JJ, “Development of a tapping device: a new needle insertion method for prostate brachytherapy,” *Phys Med Biol.* **51**, 891-902 (2006).

[42] van den Bosch MR, Moerland MA, Lagendijk JJW, Bartels LW, van den Berg CAT, “New method to monitor RF safety in MRI-guided interventions based on RF induced image artifacts,” *Med Phys.* **37**, 814-821 (2010).

[43] Ehses P, Fidler F, Nordbeck P, Pracht ED, Warmuth M, Jakob PM, Bauer WR, “MRI thermometry: Fast mapping of RF-induced heating along conductive wires,” *Magn Reson Med.* **60**, 457-461 (2008).

[44] Overall WR, Pauly JM, Stang PP, Scott GC, “Ensuring safety of implanted devices under MRI using reversed RF polarization,” *Magn Reson Med.* **64**, 823-833 (2010).

[45] Van der Heide UA, Kotte ANTJ, Dehnad H, Hofman P, Lagendijk JJW, van Vulpen M, “Analysis of fiducial marker-based position verification in the external beam radiotherapy of patients with prostate cancer,” *Radiother Oncol.* **82**, 38-45 (2007).

[46] Scheffler K, Lehnhardt S, “Principles and applications of balanced SSFP techniques,” *Eur Radiol.* **13**, 2409-2418 (2003).

[47] Zwanenburg JJM, Kuijer JPA, Marcus JT, Heethaar RM, “Steady-state free precession with myocardial tagging: CSPAMM in a single breathhold,” *Magn Reson Med.* **49**, 722-730 (2003).

[48] Raaymakers BW, Crezee J, Lagendijk JJW, “Modelling individual temperature profiles from an isolated perfused bovine tongue,” *Phys Med Biol.* **45**, 765-780 (2000).

Nederlandse samenvatting

8

MRI (magnetic resonance imaging) is een niet-invasieve techniek, waarmee weke delen beter kunnen worden afgebeeld in vergelijking met andere beeldvormende technieken, zoals echografie, CT (computed tomography) en doorlichting. Bovendien kunnen met speciale MRI-technieken gebieden worden gedetecteerd die tumorweefsel bevatten [1-3]. Het gebruik van MRI is daarom tijdens het uitvoeren van de verschillende diagnose- en behandelmethodes van prostaatkanker gewenst en zal de kwaliteit van deze methodes verder verhogen. In het geval van MRI-geleide biopsie kunnen bijvoorbeeld gerichtere biopten worden genomen [3]. Bij MRI-geleide behandelingen van prostaatkanker door middel van ioniserende straling, kan mogelijk een hogere stralingsdosis aan de tumor worden afgegeven, terwijl de dosis in de gezonde omliggende organen laag blijft [4,5].

Verschillende instituten hebben de intentie om te starten met of zijn al begonnen met het uitvoeren van MRI-geleide diagnose- en behandelmethodes van prostaatkanker. Om tijdens de uitwendige bestraling van prostaatkanker MR-afbeeldingen van het doelgebied en omliggende kritieke organen te maken, worden speciale MR-scanners en bestralingstoestellen geïntegreerd [7-9]. Huidige klinische MR-scanners zijn nu al geschikt voor het uitvoeren van MRI-geleide naaldinterventies, zoals biopsie en brachytherapie [10-12]. Ook nieuwe technieken zoals lokale bevriezing door cryoablatie [13] of verhitting door radiofrequente (RF) ablatie [14] of met HIFU (high intensity focussed ultrasound) [15] kunnen in deze MR-scanners worden uitgevoerd.

Omdat de tunnel van de MR-scanner de toegang tot de patiënt beperkt, zijn robots noodzakelijk om de voor de behandeling benodigde naald (of transducer) accuraat te positioneren. Alle MRI-geleide robots hebben hierbij te maken met technische moeilijkheden of restricties. Zo is het gebruik van ferromagnetische materialen in het algemeen verboden, dienen de beeldverstoringen door de robot en de naald te worden geminimaliseerd, moet de deformatie van het weefsel als gevolg van het prikken van de naald worden beperkt, en dient te worden voorkomen dat de RF-golven, die nodig zijn voor het maken van een MR-afbeelding, resoneren over de naald omdat dit leidt tot ongewenste weefselopwarming aan de punt van de naald.

MRI-geleide robots zijn in twee types te onderscheiden. Het eerste type, ook wel een MRI-geleide naaldmanipulator genoemd, lijnt de naald automatisch uit onder MRI-geleiding. Echter, de naald moet handmatig in de patiënt worden geprikt. Deze handeling wordt bij voorkeur (maar niet altijd) in de MR-scanner uitgevoerd, zodat de naald met MRI kan worden gevolgd. Er zijn verscheidene MRI-geleide naaldmanipulatoren ontwikkeld voor verschillende type MR-scanners en voor de verschillende manieren waarop de naald wordt ingebracht (bijvoorbeeld via het perineum of het rectum) [16-19]. Een nadeel van MRI-geleide naaldmanipulatoren is dat ze geen geavanceerde naaldinbrengtechniek (zoals het tikken of schieten van de naald) bevatten om weefselvervorming als gevolg van het prikken van de naald tegen te gaan. Bij het tweede type robot wordt de naald, nadat deze handmatig of automatisch is uitgelijnd, automatisch en onder MRI-geleiding in de prostaat gebracht. Op dit moment zijn er twee dergelijke robots ontwikkeld. Een daarvan is ontwikkeld door het John Hopkins Instituut (Verenigde Staten) en getest op honden [20]. Het bevat een speciaal mechanisme om de naald direct naar de gewenste positie te schieten. Echter, door deze techniek is het onmogelijk om in te grijpen bij onverwachte naaldafbuigingen of bij verschuivingen van het doelgebied of omliggende kritieke organen. De andere robot is ontwikkeld door het Universitair Medisch Centrum Utrecht (UMCU) [21]. De UMCU-robot bevat een speciaal tikmechanisme om de naald in kleine stappen naar het doel te tikken. Deze stapsgewijze tiktechniek heeft twee voordelen: weefselvervormingen als gevolg van het inbrengen van de naald worden sterk gereduceerd [22] en naaldafbuigingen of veranderingen van de anatomie kunnen tijdig worden waargenomen. De naald kan dan worden teruggetrokken en opnieuw ingebracht. Verder kan met de robot de gehele prostaat worden bereikt door de naald onder verschillende hoeken in te brengen vanuit een zogenaamd rotatiepunt onder de huid van het perineum [23].

Dit proefschrift beschrijft de klinische introductie van de UMCU-robot: van computersimulaties via fantomen naar *in vivo* patiëntbehandelingen. Ook worden de ontwikkelde methodes voor de kwaliteitsbewaking uitvoerig besproken.

Het tweede hoofdstuk beschrijft een haalbaarheidsstudie voor LDR (low-dose-rate) brachytherapie met de robot in een 1,5 T MR-scanner. Bij deze behandeling worden radioactieve bronnetjes met lage activiteit, ook wel zaden genoemd, met behulp van naalden permanent in de prostaat gepositioneerd.

De zaden geven lokaal de gewenste dosis af om de tumor te vernietigen. De straling neemt af met de tijd.

Door de beperkte ruimte in de tunnel van de MR-scanner is het over het algemeen niet mogelijk om de naalden parallel aan elkaar te prikken, zoals gangbaar is bij de huidige echo-geleide behandeling. Om in de MR-scanner de gehele prostaat te kunnen bereiken maakt de robot gebruik van een rotatiepunt net onder de huid van het perineum. In deze studie worden drie methodes met elkaar vergeleken: parallel prikken (gangbare methode), divergerend prikken vanuit één rotatiepunt en divergerend prikken vanuit twee rotatiepunten. De studie is gebaseerd op MR-afbeeldingen van 10 patiënten. Op de MR-afbeeldingen van het abdomen zijn voor elke patiënt de prostaat, het rectum, de blaas en de urethra ingetekend. Voor elke patiënt is de optimale dosisverdeling verkregen met zelfgeschreven software, dat gebaseerd is op IPSA (inverse planning by simulated annealing) [24-26]. Voor de optimalisatie zijn harde eisen, wat betreft een adequate dosisverdeling, gedefinieerd om onderscheid te maken tussen bruikbare en onacceptabele dosisverdelingen. Verder zijn de wensen voor een ideale dosisverdeling in de software opgenomen om de dosisverdeling verder te optimaliseren. Bij elke patiënt kreeg het doelgebied (de volledige prostaat) de gewenste dosis en werden de omliggende kritieke organen voldoende gespaard.

Deze studie toonde aan dat de verkregen dosisverdelingen bij divergerend prikken net zo goed zijn als die van parallel prikken.

Omdat MRI ook de kritische structuren afbeeldt, kan het aantal naalden dat door een kritiek orgaan wordt geprikt om het doelgebied te bereiken (bijvoorbeeld door structuren die verantwoordelijk zijn voor erectiele functies) een reden zijn om voor een bepaalde implantatiemethode te kiezen.

In het algemeen kunnen de dosisverdelingen verder worden verbeterd door het bereikbare prostaatgebied (achter de urethra) te vergroten, bijvoorbeeld door het reduceren van de catheterdiameter of door de afstand tussen de twee rotatiepunten te vergroten. Het verhogen van het aantal mogelijke bronposities kan ook tot een betere dosisverdeling leiden.

Verder volgt uit het tweede hoofdstuk dat bij vergroting van het het doelgebied (3 mm marge om prostaat) de zaden gedeeltelijk buiten de prostaat moeten worden gelegd om een adequate dosisverdeling te bewerkstelligen.

In hoofdstuk 3 wordt een nieuwe methode geïntroduceerd, waarmee aan de hand van artefacten in de MR-afbeeldingen kan worden voorspeld of er ongewenste weefselopwarming rondom de (robot)naald plaatsvindt.

Het is namelijk bekend dat langgerekte, elektrisch geleidende voorwerpen, zoals voerdraden, catheters, en naalden een interactie met het elektromagnetisch veld van de MR-scanner aan kunnen gaan, wat in weefselopwarming aan de punt van het voorwerp kan resulteren [27-30]. De mate van interactie correleert met de in het voorwerp geïnduceerde elektrische stroom, die op zijn beurt gerelateerd is aan de weefselopwarming aan de punt van het voorwerp [31,32]. In fantomen met lange voerdraden zijn grote temperatuurstijgingen van 35 graden Celsius gemeten [27,28]. In deze gevallen resoneerden de RF-golven over het voorwerp. Het is echter moeilijk te voorspellen wanneer resonantie *in vivo* precies optreedt, omdat dit afhangt van vele factoren, zoals de diëlektrische eigenschappen en het volume van het omliggend weefsel en de RF-excitatiefrequentie.

De nieuwe methode waarmee deze ongewenste situaties met kans op weefselopwarming kunnen worden gedetecteerd, wordt in dit hoofdstuk uitgewerkt en getest in twee verschillende fantoomexperimenten. Het eerste experiment bootst een interventie met een brachytherapienaald na. Centraal in de tunnel van een 3T MR-scanner wordt een korte naald in een cilinder met gelatine geprikt. In het tweede experiment wordt een lange voerdraad aan de rand van de tunnel van de MR-scanner in een cilinder gebracht die gevuld is met water waar $MnCl_2$ in is opgelost. In beide experimenten wordt de insteekdiepte gevarieerd en zijn de voorwerpen parallel gelegen aan de richting van het statische magneetveld. Een voor de MRI geschikte temperatuursensor is op de punt van het voorwerp geplaatst om de temperatuur te bemonsteren. Vervolgens zijn er verscheidene MR-afbeeldingen (type: ‘spoiled gradient echo’) met verschillende fliphoeken gemaakt om de veldinteractie in kaart te brengen. Daarna is er een analytisch model aan de veldinteractie gefit om de in het voorwerp geïnduceerde stroom te kwantificeren.

Deze studie toont aan dat het mogelijk is om de in het voorwerp geïnduceerde stroom te kwantificeren door de veldinteractiewaardes op 7 tot 10 mm van het voorwerp te gebruiken. Het golfgedrag in het stroomprofiel was duidelijk zichtbaar. In het algemeen was de stroom in de lange voerdraad veel hoger dan in de naald. De belangrijkste oorzaken hiervan zijn de grotere lengte en de off-center positie van de voerdraad. Alleen in het tweede experiment werden temperatuurstijgingen aan de punt van het voorwerp waargenomen (2,4°C in 1

minuut), terwijl voor beide experimenten stroomprofielen konden worden opgesteld. Dit suggereert dat onze methode een hele gevoelige methode is om het resonantiegedrag te onderzoeken.

De methode lijkt ook toepasbaar voor voorwerpen die onder een hoek ten opzichte van het magneetveld zijn geplaatst, mits de vlakken waarin de fit wordt uitgevoerd loodrecht op het voorwerp worden gedefinieerd. Mogelijk moet er vooraf nog worden gecorrigeerd voor de beeldverstoring langs het voorwerp als gevolg van verschil in magnetische susceptibiliteit tussen de naald en het omliggend weefsel (susceptibiliteitsartefact). Dit artefact is bij deze oriëntatie namelijk langs het gehele voorwerp zichtbaar (in plaats van alleen dichtbij de punt) [33].

De stroomprofielen die berekend zijn met deze methode kunnen mogelijk in de toekomst worden gevalideerd met stroomsensoren [32,34].

De methode kan worden gebruikt voor veiligheidstesten of om bijvoorbeeld het effect van naaldcoating op de resonantielengte te onderzoeken. Hoewel de methode *ex vivo* is getest, is deze in principe ook *in vivo* toepasbaar. De volgende stap is de bepaling van SAR (specific absorption rate) aan de punt van het voorwerp. Dit is een maat voor de weefselopwarming.

In hoofdstuk 4 staan de overwegingen, die bij het ontwikkelen van een robot voor MRI-geleide interventies moeten worden gemaakt, en verschillende veiligheids- en kwaliteitstesten vermeld.

De beschikbare ruimte in de MR-scanner en de toegang tot de patiënt zijn belangrijk bij het ontwerpen van de robot. Tussen de twee magneetpolen van de open MR-scanners kan de patiënt vanuit vrijwel elke hoek worden bereikt. Bij gesloten MR-scanners is de toegankelijkheid beperkter. Daarentegen is de beschikbare veldsterkte voor gesloten MR-scanners hoger, wat resulteert in betere beeldkwaliteit [35]. Bovendien ligt het bij een gesloten MR-scanner meer voor de hand dat de naald parallel aan het statische magneetveld wordt geprikt. Voor deze naaldoriëntatie is het susceptibiliteitsartefact, dat door de naald in de MR-afbeelding wordt veroorzaakt, beperkt tot de naaldpunt [33]. Hogere veldsterktes hebben echter ook nadelen voor robotgestuurde interventies. De belangrijkste nadelen zijn: de golflengteafname van de RF-golven, waardoor de kans op ernstige weefselopwarming aan de punt van de naald toeneemt [27,30], en de grotere verstoringen van het statische magneetveld en

bijbehorende grotere beeldartefacten die door de robot en de naald worden veroorzaakt [35,36].

De toegang tot de patiënt en het doelgebied kan worden onderzocht door het fictief uitvoeren van de gewenste interventie op bijvoorbeeld reeds verkregen MR-afbeeldingen. De materiaalkeuze van de robot is van belang voor de compatibiliteit met het magneetveld en de werking in het magneetveld. Vanwege de grote aantrekkende krachten is het gebruik van ferromagnetische metalen niet toegestaan. Metalen als aluminium, koper en titanium zijn toegestaan, maar omdat ongewenste wervelstromingen (eddy currents) in geleidende platen of in lussen de werking van de robot negatief beïnvloeden, is het aanbevolen om het oppervlak van deze platen of lussen te verminderen en waar mogelijk het gebruik van deze structuren te vermijden [37-39]. Onze robot bevat elektrisch geleidende platen en andere componenten, maar de werking van de robot is niet merkbaar afgenomen in een 1,5 T magnetisch veld. Dit bewijst dat MRI-geleide robots weldegelijk elektrisch geleidende componenten kunnen bevatten.

Geometrische beeldverstoringen als gevolg van verstoringen in het statische magneetveld (statische veldfouten) of niet-lineariteit van de gradiënten (gradiëntfout) kunnen de nauwkeurigheid van de naaldpositionering verminderen [40]. De fouten kunnen worden gekwantificeerd door een experiment in de MR-scanner uit te voeren met een buisjesfantoom. De statische veldfouten, die door de UMCU-robot worden veroorzaakt, nemen af naarmate de afstand tot de robot toeneemt: van 16 delen per miljoen (ppm) nabij de robot tot 5 ppm in het midden van het isocentrum, dat in dit geval op 17 cm van de robot af is gelegen. De geometrische beeldverstoringen als gevolg van verstoringen van het statische veld kunnen in het algemeen worden geminimaliseerd door de sterkte van de uitleesgradiënt te verhogen of door het gebruik van (robot)materialen met een magnetische susceptibiliteit die meer overeenkomt met die van menselijk weefsel, zoals polymeren [40]. Gradiëntfouten kunnen worden gereduceerd door te corrigeren voor de niet-lineariteiten van de gradiënten, bijvoorbeeld met behulp van de scannersoftware voor geometrische beeldcorrectie. De verschillen in gradiëntfouten tussen de situaties met en zonder robot in de MR-scanner zijn verwaarloosbaar, behalve in de cranio-caudale richting waar de toename van de beeldverstoring < 2mm bedroeg.

Ook het susceptibiliteitsartefact aan de punt van de naald in de MR-afbeelding, maakt de naaldpositionering moeilijk. Hoewel het artefact voor homogeen

weefsel met bekende magnetische susceptibiliteit goed kan worden gesimuleerd en de positie van de naald hiermee nauwkeurig kan worden geschat [33], is het moeilijk om de exacte positie van de naaldpunt te achterhalen in heterogeen weefsel met onbekende magnetische susceptibiliteit. Deze lokalisatieonzekerheid kan worden verminderd door naaldmaterialen met een susceptibiliteit dichter bij weefsel te gebruiken of door de scanparameters te optimaliseren, bijvoorbeeld door een 180° refocusserende puls toe te voegen om statische veldinhomogeniteiten te compenseren [33,36,41,42].

Als weefsel vervormt tijdens het inbrengen van de naald kan dit negatieve gevolgen hebben voor de positioneringnauwkeurigheid. Er zijn verschillende geavanceerde naaldinbrengtechnieken ontwikkeld om deze vervormingen tegen te gaan. Enkele voorbeelden zijn axiale naaldrotatie [43], het schieten van de naald [20], en het tikken van de naald [22]. Onze robot maakt gebruik van de laatste techniek.

Als de naald op de weg naar het doelgebied afbuigt heeft dit ook negatieve gevolgen voor de positioneringnauwkeurigheid. Bovendien kan het gevaarlijk zijn voor de patiënt. Daarom maakt de UMCU-robot gebruik van een techniek, waarbij de naald stapsgewijze naar binnen wordt getikt, zodat op de snelle MR-afbeeldingen ongewenste naaldafbuigingen tijdig kunnen worden waargenomen. De naald kan in zulke gevallen worden teruggetrokken om vervolgens opnieuw in te worden gebracht.

Het risico van ongewenste weefelopwarming aan de punt van de naald, als gevolg van resonerende RF-golven over de naald, kan worden onderzocht door het uitvoeren van verscheidene fantoomexperimenten, die de slechts denkbare scenario's nabootsen. Meestal worden MRI-geschikte temperatuursensoren gebruikt om de weefseltemperatuur aan de punt van de naald te meten [27-30,44]. De verkregen waarde is zeer afhankelijk van de sensorlocatie ten opzichte van de naaldpunt, omdat de energie lokaal wordt gedeponeerd [45]. MR-thermometrie is een bruikbare niet-invasieve MR-techniek om weefselopwarmning in de gaten te houden, maar kan in dit geval helaas niet worden gebruikt in verband met het susceptibiliteitsartefact (rond de punt) van de naald [45]. Onze methode, die in hoofdstuk 3 werd beschreven, kwantificeert aan de hand van beeldartefacten rond de naald de geïnduceerde stroom in de naald en kan worden gebruikt om de RF-veiligheid te onderzoeken [44]. Bij een recent gepubliceerde nieuwe kwalitatieve methode om deze RF-veiligheid te onderzoeken wordt alleen het weefsel rond een eventueel

aanwezig gevaarlijk voorwerp op de MR-afbeelding zichtbaar [46]. Met de laatste twee genoemde methodes kunnen potentiële gevaarlijke situaties niet-invasief worden gedetecteerd, zonder de weefseltemperatuur zelf te meten.

Het aanbrengen van coating op de naald of het gebruik van niet-geleidende naaldmaterialen kan het risico op weefselopwarming respectievelijk verminderen of uitsluiten [30].

Hoofdstuk 5 levert het bewijs dat MRI-geleide naaldinterventies in de prostaat met onze robot kunnen worden uitgevoerd. In deze studie worden vier goudmarkers met behulp van de robot in de prostaat van een patiënt gebracht. De goudmarkers, die een vergelijkbare afmeting hebben als de brachytherapiezaden, worden gebruikt voor de positieverificatie van de prostaat tijdens uitwendige bestraling buiten de MRI [47]. Omdat de gehele prostaat het doelgebied is, is de exacte positionering van de markers niet essentieel. Hierdoor is het een ideale toepassing om de robot op patiënten uit te proberen.

Om de vier markers te plaatsten werden in totaal twee naalden (elk voor het plaatsen van twee markers) na elkaar en parallel aan de longitudinale as van de MR-tunnel in de prostaat getikt. De procedure bevatte de volgende stappen. De patiënt werd na lokale verdoving op zijn rug, met zijn benen licht gespreid langs de robot, op de MR-tafel gelegd. Daarna werd de robot inclusief de naald met de hand uitgelijnd en werd de naald manueel door de huid van het perineum geduwd. MRI werd gebruikt om het naaldtraject te controleren en de doelposities te definiëren. Vervolgens tikte de robot de naald in kleine stappen naar de verste doelpositie, terwijl de naald met snelle MR-afbeeldingen werd gevolgd. Vervolgens plaatste de radiotherapeut een goudmarker door de naald op de bereikte plek. Daarna werd de naald onder MRI-geleiding door de robot teruggetikt naar de tweede doelpositie om daar de tweede goudmarker achter te laten. Nadat de tweede goudmarker was geplaatst, werd de naald naar zijn nulstand teruggetikt en werd er een MR-afbeelding van de prostaat met de markers gegenereerd. Deze procedure werd herhaald om de derde en vierde goudmarker in de prostaat achter te laten.

In alle MR-afbeeldingen was het mogelijk om zowel de anatomie van de patiënt (bijvoorbeeld prostaat, rectum en os pubis) als de goudmarkers en de naald te onderscheiden. De naald kon goed worden gevolgd met de snelle MR-afbeeldingen, die elkaar frequent opvolgden. Binnen 5,2 seconden konden twee

orthogonale afbeeldingen met de snijlijn op de naald worden bewerkstelligd. In deze afbeeldingen is het susceptibiliteitsartefact aan de tip van de naald duidelijk zichtbaar. Simulaties en experimenten hebben eerder aangetoond dat, bij de in deze studie gebruikte MRI-instellingen, de punt van de naald in werkelijkheid ongeveer 5 mm proximaal van de rand van dit artefact is gelegen [33]. In de MR-afbeeldingen zijn artefacten waar te nemen, die door de robot zijn veroorzaakt. Dit wijst op de aanwezigheid van lokale verstoringen in het magnetisch veld [48]. Deze verstoringen leiden tot geometrische verstoringen in de MR-afbeelding, maar kunnen worden beperkt door het gebruik van grote uitleesgradiënten [40]. Bovendien zijn ze verwaarloosbaar klein dichtbij het doelgebied. Ondanks het tikken van de naald, deformeert de buitenrand van de prostaat nabij de blaas 7 mm in de afbeelding. Dit suggereert dat het tikmechanisme van de robot verder moet worden geoptimaliseerd.

In de snelle MR-afbeeldingen, die worden gebruikt om de naald tijdens het tikken te volgen, is het niet mogelijk om de lokale weefselvervorming als gevolg van het inbrengen van de naald te kwantificeren. Dit komt doordat bij deze MR-sequenties waarneembare structuren in de prostaat ontbreken. In hoofdstuk 6 is onderzocht of het mogelijk is om kunstmatige structuren in de prostaat aan te brengen, zodat die lokale weefselvervormingen wel kunnen worden achterhaald. Door middel van zogenaamde MR-tagging kunnen kunstmatige structuren (tags) tijdelijk worden aangebracht. Dit wordt gedaan door volgens een gedefinieerd patroon de magnetisatie in het weefsel te verzadigen, waardoor er een lijn- of bandpatroon in de MR-afbeelding zichtbaar wordt. De deformatie van dit patroon komt overeen met de deformatie van het weefsel in de periode tussen patrooncreatie en –visualisatie. In het algemeen wordt deze techniek gebruikt bij repeterende processen zoals hartcontractie, waarbij informatie van meerdere cycli samengevoegd kunnen worden voor de vorming van een afbeelding met optimaal contrast. Doordat de naaldbeweging eenmalig is, dient een adequate afbeelding in één keer te worden verkregen. Zo'n methode kan niet alleen worden gebruikt om de kwaliteit van het tikken door de robot te testen, maar ook om de naaldinterventie te verbeteren, bijvoorbeeld door op grond van de deformatie-informatie de naaldpositie aan te passen.

Onze MR-taggingmethode bevat een zogenaamde 1331-puls om het tagpatroon te creëren en een sequentie gebaseerd op bSSFP (balanced Steady State Free Precession) om het patroon te visualiseren. In de tussenliggende periode, de

zogenaamde interventieperiode, dient de naaldbeweging plaats te vinden. De scanparameters zijn geoptimaliseerd voor het bewerkstelligen van een goede beeldkwaliteit in alle experimenten. Vier experimenten werden er uitgevoerd op een 1,5 T MR-scanner. De eerste om translaties te kwantificeren, de tweede voor het kwantificeren van rotaties, de derde om een naaldinterventie na te bootsten en de vierde om op een vrijwilliger te achterhalen na hoeveel tijd het tagpatroon nog kan worden gevisualiseerd.

Het tagpatroon was in alle experimenten duidelijk te onderscheiden. De sterke correlaties tussen de opgelegde en opgemeten verplaatsingen tonen aan dat onze MR-taggingmethode kan worden gebruikt om translaties en rotaties te kwantificeren. In het naaldinterventie-experiment waren aan de hand van het tagpatroon weefselverplaatsingen tot wel 5 mm zichtbaar. Wanneer er geen naaldbeweging plaatsvond waren de taglijnen in de afbeelding perfect horizontaal. Dit suggereert dat het patroon niet is verstoord door de aanwezigheid van de naald. Bij de vrijwilliger kon het tagpatroon in de prostaat 2 seconden na het opleggen nog worden onderscheiden. Deze periode was nog langer voor weefsels met een grotere T_1-waarde, zoals (de inhoud) van de blaas.

In de afbeeldingen zijn donkere kringen (banding artefacts) waar te nemen. Ook is er signaal van het object in gebieden met lucht terecht gekomen (ghosting artefacts). De ghosting artefacten die afkomstig zijn van vettig weefsel kunnen worden gereduceerd door het gebruik van vetonderdrukking in de scansequentie of door de fliphoeken van de eerste pulsen van het afbeeldingsgedeelte linear toe te laten nemen [49].

In het geval dat het weefsel, waarin het gewenste tagpatroon moet worden afgebeeld, lange T_1 - en T_2-waardes bevat, kan de sequentie verder worden geoptimaliseerd, bijvoorbeeld door het verhogen van de fliphoek.

In de naaldexperimenten werden de naaldbewegingen manueel uitgevoerd. Het begin van de interventieperiode kon in de scanruimte worden herkend door het geluid dat de MR-scanner produceert. Indien er robots worden gebruikt voor het inbrengen van de naald, is het mogelijk om het moment van inbreng softwarematig te koppelen aan de startpuls van de MR-scanner.

Onze MR-taggingmethode kan worden gebruikt om naaldinterventies te verbeteren, bijvoorbeeld door de naaldpositie aan de hand van de deformatie-informatie aan te passen. Het kan ook worden gebruikt om het effect van verschillende naaldinbrengtechnieken (tikken, schieten, rotatie) te vergelijken. De sequentie is mogelijk ook bruikbaar bij andere situaties met

weefseldeformaties in de tijd, bijvoorbeeld om weefseldeformaties als gevolg van ademhaling vast te leggen.

De klinische introductie van de UMCU-robot en de eerste klinische ervaringen met deze robot zijn in dit proefschrift beschreven. De UMCU-robot moet handmatig worden uitgelijnd, maar tikt de naald automatisch en onder MRI-geleiding in de prostaat. Het is mogelijk om tijdens het tikken van de naald MR-afbeeldingen te maken. Deze afbeeldingen zijn van hoge kwaliteit en kunnen worden gebruikt om de naald te volgen. Het tikmechanisme om weefselvervormingen tijdens het prikken van de naald te minimaliseren en het gebruik van een rotatiepunt om de gehele prostaat te bereiken, maken de robot uniek. Op dit moment wordt het tikmechanisme verder geoptimaliseerd om weefselvervormingen geheel te voorkomen.

Voor zover bekend is de UMCU-robot wereldwijd de eerste en tot nu toe enige robot met automatische naaldinbreng die voor patiëntinterventies in de MR-scanner is gebruikt. De mogelijkheid om een naald met de robot onder MRI-geleiding te tikken is een grote stap naar MRI-geleide biopten en brachytherapie.

De eerste toepassingen van de geoptimaliseerde robot zullen MRI-geleide biopten en focale HDR (high-dose-rate) brachytherapie zijn. Bij beide toepassingen hoeven geen zaden, goudmarkers, of andere kleine deeltjes in de prostaat te worden achtergelaten en is alleen een hoge nauwkeurigheid van de naaldpositionering gewenst. Dit maakt het herontwerpen van het tikmechanisme een stuk eenvoudiger.

References

[1] Delongchamps NB, Rouanne M, Flam T, Beuvon F, Liberatore M, Zerbib M, Cornud F, "Multiparametric magnetic resonance imaging for the detection and localization of prostate cancer: combination of T2-weighted, dynamic contrast-enhanced and diffusion-weighted imaging," *BJU Int.* Nov 2. doi: 10.1111/j.1464-410X.2010.09808.x. [ahead of print] (2010).

[2] Groenendaal G, Moman MR, Korporaal JG, van Diest PJ, van Vulpen M, Philippens MEP, van der Heide UA, "Validation of functional imaging with pathology for tumor delineation in the prostate," *Radiother Oncol.* **94**, 145-150 (2010).

[3] Labanaris AP, Engelhard K, Zugor V, Nützel R, Kühn R, "Prostate cancer detection using an extended prostate biopsy schema in combination with additional targeted cores from suspicious images in conventional and functional endorectal magnetic resonance imaging of the prostate," *Prostate Cancer Prostatic Dis.* **13**, 65-70 (2010).

[4] van Vulpen M, van der Heide UA, "FLAME: Investigate the benefit of a focal lesion ablative microboost in prostate cancer," www.clinicaltrials.gov/ct2/show/NCT01168479, visited 15-11-2011.

[5] Daanen V, Gastaldo J, Giraud JY, Fourneret P, Descotes JL, Bolla M, Collomb D, Troccaz J, "MRI/TRUS data fusion for brachytherapy," *Int J Med Robot.* **2**, 256-261 (2006).

[6] Smitsmans MHP, de Bois J, Sonke JJ, Betgen A, Zijp LJ, Jaffray DA, Lebesque JV, van Herk M, "Automatic prostate localization on cone-beam CT scans for high precision image-guided radiotherapy," *Int J Radiat Oncol Biol Phys.* **15**, 975-984 (2005).

[7] Lamey M, Burke B, Blosser E, Rathee S, De Zanche N, Fallone BG, "Radio frequency shielding for a linac-MRI system," *Phys Med Biol.* **55**, 995-1006 (2010).

[8] Raaymakers BW, Lagendijk JJW, Overweg J, Kok JGM, Raaijmakers AJE, Kerkhof EM, van der Put RW, Meijsing I, Crijns SPM, Benedosso F, van Vulpen M, de Graaff CHW, Allen J, Brown KJ, "Integrating a 1.5 T MRI scanner with a 6 MV accelerator: proof of concept," *Phys Med Biol.* **54**, 229-237 (2009).

[9] Kron T, Eyles D, Schreiner JL, Battista J, "Magnetic resonance imaging for adaptive cobalt tomotherapy: A proposal," *J Med Phys.* **31**, 242-254 (2006).

[10] Susil RC, Camphausen K, Choyke P, McVeigh ER, Gustafson GS, Ning H, Miller RW, Atalar E, Coleman CN, Ménard C, "System for prostate brachytherapy and biopsy in a standard 1.5 T MRI scanner," *Magn Reson Med.* **52**, 683-687 (2004).

[11] Engelhard K, Hollenbach HP, Kiefer B, Winkel A, Goeb K, Engehausen D, "Prostate biopsy in the supine position in a standard 1.5-T scanner under real time MR-imaging control using a MR-compatible endorectal biopsy device," *Eur Radiol.* **16**, 1237-1243 (2006).

[12] Ares C, Popowski Y, Pampallona S, Nouet P, Dipasquale G, Bieri S, Ozsoy O, Rouzaud M, Khan H, Miralbell R, "Hypofractionated boost with high-dose-rate brachytherapy and open magnetic resonance imaging-guided implants for locally aggressive prostate cancer: a sequential dose-escalation pilot study," *Int J Radiat Oncol Biol Phys.* **75**, 656-663 (2009).

[13] Josan S, Bouley DM, van den Bosch M, Daniel BL, Butts Pauly K, "MRI-guided cryoablation: In vivo assessment of focal canine prostate cryolesions," *J Magn Reson Imaging.* **30**, 169-176 (2009).

[14] Woodrum DA, Gorny KR, Mynderse LA, Amrami KK, Felmlee JP, Bjarnason H, Garcia-Medina OI, McNichols RJ, Atwell TD, Callstrom MR, "Feasibility of 3.0T magnetic resonance imaging-guided laser ablation of a cadaveric prostate," *Urology.* **75**, 1514.e1-1514.e6 (2010).

[15] Chopra R, Burtnyk M, N'djin WA, Bronskill M, "MRI-controlled transurethral ultrasound therapy for localised prostate cancer," *Int J Hyperthermia.* **26**, 804-821 (2010).

[16] DiMaio SP, Pieper S, Chinzei K, Hata N, Haker SJ, Kacher DF, Fichtinger G, Tempany CM, Kikinis R, "Robot-assisted needle placement in open MRI: system architecture, integration and validation," *Comput Aided Surg.* **12**, 15-24 (2007).

[17] Schouten MG, Ansems J, Renema WKJ, Bosboom D, Scheenen TWJ, Fütterer JJ, "The accuracy and safety aspects of a novel robotic needle guide manipulator to perform transrectal prostate biopsies," *Med Phys.* **37**, 4744-4750 (2010).

[18] Chinzei K, Hata N, Jolesz F, Kikinis R, "Surgical assist robot for the active navigation in the intraoperative MRI: Hardware design issues," *Proceedings of the IEEE/RSJ International Conference on Intelligent Robots and Systems*, Takamatsu, Japan, 727–732 (2000).

[19] Fischer GS, DiMaio SP, Iordachita I, Fichtinger G, "Robotic Assistant for Transperineal Prostate Interventions in 3T Closed MRI," *Med Image Comput Comput Assist Interv.* **10**, 425-433 (2007).

[20] Muntener M, Patriciu A, Petrisor D, Schär M, Ursu D, Song DY, Stoianovici D, "Transperineal prostate intervention: robot for fully automated MR imaging-system description and proof of principle in a canine model," *Radiology.* **247**, 543-549 (2008).

[21] van den Bosch MR, Moman MR, van Vulpen M, Battermann JJ, Duiveman E, van Schelven LJ, de Leeuw H, Lagendijk JJW, Moerland MA, "MRI-guided robotic system for transperineal prostate interventions: proof of principle.", *Phys Med Biol.* **55**, 133-140. Feb 10 (2010).

[22] Lagerburg V, Moerland MA, van Vulpen M, Lagendijk JJW, "A new robotic needle insertion method to minimise attendant prostate motion," *Radiother Oncol.* **80**, 73-77 (2006).

[23] Van Gellekom MPR, Moerland MA, Battermann JJ, Lagendijk JJW, "MRI-guided prostate brachytherapy with single needle method-a planning study," *Radiother Oncol.* **71**, 327-332 (2004).

[24] Lessard E, Kwa SL, Pickett B, Roach M 3rd, Pouliot J, "Class solution for inversely planned permanent prostate implants to mimic an experienced dosimetrist," *Med Phys.* **33**, 2773-2282 (2006).

[25] Lessard E, Pouliot J, "Inverse planning anatomy-based dose optimization for HDR-brachytherapy of the prostate using fast simulated annealing algorithm and dedicated objective function," *Med Phys.* **28**, 773-779 (2001).

[26] Pouliot J, Tremblay D, Roy J, Filice S, "Optimization of permanent 125I prostate implants using fast simulated annealing," *Int J Radiat Oncol Biol Phys.* **36**, 711-720 (1996).

[27] Dempsey MF, Condon B, Hadley DM, "Investigation of the factors responsible for burns during MRI," *J Magn Reson Imaging.* **13**, 627-631 (2001).

[28] Konings MK, Bartels LW, Smits HF, Bakker CJG, "Heating around intravascular guidewires by resonating RF waves," *J Magn Reson Imaging.* **12**, 79-85 (2000).

[29] Yeung CJ, Karmarkar P, McVeigh ER, "Minimizing RF heating of conducting wires in MRI," *Magn Reson Med.* **58**, 1028-1034 (2007).

[30] Yeung CJ, Susil RC, Atalar E, "RF safety of wires in interventional MRI: using a safety index," *Magn Reson Med.* **47**, 187-193 (2002).

[31] Nitz WR, Oppelt A, Renz W, Manke C, Lenhart M, Link J, "On the heating of linear conductive structures as guide wires and catheters in interventional MRI," *J Magn Reson Imaging.* **13**, 105-114 (2001).

[32] Nordbeck P, Weiss I, Ehses P, Ritter O, Warmuth M, Fidler F, Herold V, Jakob PM, Ladd ME, Quick HH, Bauer WR. "Measuring RF-induced currents inside implants: Impact of device configuration on MRI safety of cardiac pacemaker leads," *Magn Reson Med.* **61**, 570-578, (2009).

[33] Lagerburg V, Moerland MA, Seppenwoolde JH, Lagendijk JJW, "Simulation of the artefact of an iodine seed placed at the needle tip in MRI-guided prostate brachytherapy," *Phys Med Biol.* **53**, 59-67 (2008).

[34] Zanchi MG, Venook R, Pauly JM, Scott G, "An optically-coupled system for quantitative monitoring of MRI-induced RF currents into long conductors," *oral presentation at the ISMRM 16th scientific meeting & exhibition*, Toronto, Canada, 2008.

[35] Machann J, Schlemmer HP, Schick F, "Technical challenges and opportunities of whole-body magnetic resonance imaging at 3T," *Phys Med.* **24**, 63-70 (2008).

[36] Guermazi A, Miaux Y, Zaim S, Peterfy CG, White D, Genant HK, "Metallic artefacts in MR imaging: effects of main field orientation and strength," *Clin Radiol.* **58**, 322-328 (2003).

[37] Dempsey MF, Condon B, Hadley DM, "MRI safety review," *Semin Ultrasound CT MR.* **23**, 392-401 (2002).

[38] Graf H, Lauer UA, Schick F, "Eddy-current induction in extended metallic parts as a source of considerable torsional moment," *J Magn Reson Imaging.* **23**, 585-590 (2006).

[39] Robertson NM, Diaz-Gomez M, Condon B, “Estimation of torque on mechanical heart valves due to magnetic resonance imaging including an estimation of the significance of the Lenz effect using a computational model,” *Phys Med Biol.* **45**, 3793-3807 (2000).

[40] Bakker CJG, Moerland MA, Bhagwandien R, Beersma R, “Analysis of machine-dependent and object-induced geometric distortion in 2DFT MR imaging,” *Magn Reson Imaging.* **10**, 597-608 (1992).

[41] Müller-Bierl B, Graf H, Lauer U, Steidle G, Schick F, “Numerical modeling of needle tip artifacts in MR gradient echo imaging,” *Med Phys.* **31**, 579-587 (2004).

[42] Port JD, Pomper MG, “Quantification and minimization of magnetic susceptibility artifacts on GRE images,” *J Comput Assist Tomogr.* **24**, 958-964 (2000).

[43] Abolhassani N, Patel R, Moallem M, “Control of soft tissue deformation during robotic needle insertion,” *Minim Invasive Ther Allied Technol.* **15**, 165-176 (2006).

[44] van den Bosch MR, Moerland MA, Lagendijk JJW, Bartels LW, van den Berg CAT, “New method to monitor RF safety in MRI-guided interventions based on RF induced image artifacts,” *Med Phys.* **37**, 814-821 (2010).

[45] Ehses P, Fidler F, Nordbeck P, Pracht ED, Warmuth M, Jakob PM, Bauer WR, “MRI thermometry: Fast mapping of RF-induced heating along conductive wires,” *Magn Reson Med.* **60**, 457-461 (2008).

[46] Overall WR, Pauly JM, Stang PP, Scott GC, “Ensuring safety of implanted devices under MRI using reversed RF polarization,” *Magn Reson Med.* **64**, 823-833 (2010).

[47] Van der Heide UA, Kotte ANTJ, Dehnad H, Hofman P, Lagendijk JJW, van Vulpen M, “Analysis of fiducial marker-based position verification in the external beam radiotherapy of patients with prostate cancer,” *Radiother Oncol.* **82**, 38-45 (2007).

[48] Scheffler K, Lehnhardt S, “Principles and applications of balanced SSFP techniques,” *Eur Radiol.* **13**, 2409-2418 (2003).

[49] Zwanenburg JJM, Kuijer JPA, Marcus JT, Heethaar RM, “Steady-state free precession with myocardial tagging: CSPAMM in a single breathhold,” *Magn Reson Med.* **49**, 722-730 (2003).

Dankwoord

Het geeft een fijn gevoel dat de resultaten van ruim vier jaar interessant onderzoek vereeuwigd zijn in dit proefschrift. Dit was niet gelukt zonder de steun van een aantal mensen die ik in dit dankwoord graag wil bedanken.

Om te beginnen bij mijn promotor, Jan Lagendijk. Jan, ik wil je bedanken voor het vertrouwen dat je in mij hebt gesteld en de mogelijkheden die je me hebt geboden om mezelf te ontplooien en te ontwikkelen. Daarmee bedoel ik niet alleen de stimulans die je bood tot het ruimer en vernieuwend denken, maar bijvoorbeeld ook de aanmoediging om veel congressen bij te wonen. Je deur stond altijd open voor vragen of advies, waarbij je altijd erg open en eerlijk was zonder een blad voor de mond te nemen. Dat waardeer ik enorm.

Ook wil ik mijn co-promotor en dagelijkse begeleider Rien Moerland bedanken. Rien, jouw enthousiasme, gestructureerdheid en taalvaardigheid is een voorbeeld voor iedereen. Je gaf me de ruimte om verschillende zijwegen van het project in te slaan op het moment dat er (door anderen) aan de robot gesleuteld moest worden. Als ik vragen had of even wilde klankborden kon ik altijd bij je binnen lopen, of je tijd had of niet. Een betere begeleider had ik me niet kunnen wensen.

Mijn andere co-promotor Marco van Vulpen, wil ik graag bedanken voor alle klinische ondersteuning en positivisme tijdens het project. Mede door je pragmatisch denken, praktische vaardigheden en grote patiëntbetrokkenheid is het gelukt om de MRI-geleide robot bij patiënten te gebruiken.

Nico, ook jij hebt me even begeleid. Het project ontstond tijdens een brainstorm in de tijd dat je mijn kamergenoot was. Naast het hard en geconcentreerd werken, was er tijd voor gezelligheid, zoals meezingen op Spinvis. Verder heb ik je leren kennen als een goede vriend, die altijd voor iedereen klaar staat. Op het laatste moment een slaapplek verzorgen omdat de treinen niet reden was geen probleem en werd aangegrepen om de stad tot in de nachtelijke uren te verkennen.

Uulke, bedankt dat je me hebt ‘geadopteerd’ in de prostaatgroep. Het gaf me niet alleen de kans mezelf te verbreden en resultaten te bediscussiëren in een grote groep, maar ook de mogelijkheid om te genieten van jouw kookkunsten tijdens de prostaatetentjes.

Marion en Vera, ik wil jullie graag bedanken voor de mooie basis die jullie hebben gelegd voor mijn promotieonderzoek. Leuk dat we elkaar altijd nog even opzoeken bij plechtigheden of sociale gelegenheden. Dat moeten we erin houden.

Irene en Maaike, bedankt voor het plezierig samenwerken en discussiëren tijdens robotoverleg en later ook prostaatoverleg. Ik kijk met plezier terug op de korte vakanties na congressen in Barcelona en Hawaii.

Hendrik, we hebben samen heel veel scanuren doorgebracht. Altijd was je bereid om te helpen en in staat om het onderzoek naar een hoger niveau te tillen. Naast het zijn van een wandelende MRI-encyclopedie heb ik je leren kennen als een enthousiast, toegewijd en gezellig persoon om mee samen te werken.

Tuan, ik wil je graag bedanken voor de assistentie bij de MRI-geleide goudmarkerimplantaties en natuurlijk voor het gezamenlijk organiseren van de voetbalpool tijdens het EK en WK met een mooie strijd op de afdeling als gevolg.

Verder zou ik graag Peter, Leonard, Joris, Han, Bert, Ed, Jan, Kees, Johan en Ruben van het cluster Medische Technologie & Klinische Fysica willen bedanken voor het ontwikkelen en optimaliseren van de robot, het vervaardigen van fantomen, en de technische ondersteuning tijdens de experimenten. Hiervoor werd, ondanks de drukte, altijd wel een gaatje gevonden. Bedankt voor de goede samenwerking.

Wilbert en Jaco, bedankt voor jullie prettige samenwerking en kennisoverdracht. Het gaf me de kans om van verschillende vakgebieden te proeven. Bovendien hoop ik ook iets van Wilbert’s instinct voor het vinden van gezellige eet- en feestgelegenheden in het buitenland op te hebben gepikt.

Dit is een mooie gelegenheid om Jan Verwoerd van Philips Healthcare nogmaals te bedanken voor onder andere het optimaliseren van de MR sequenties om scherpe afbeeldingen tijdens de robotexperimenten te bewerkstelligen.

Ook wil ik Stefan Franken en Chris Bakker bedanken voor hun bijdrage aan het robotproject.

Verder wil ik graag het laborantenteam van de brachytherapie bedanken voor het tijdig laten steriliseren van alle benodigde onderdelen voor iedere robotimplantatie.

Ook wil ik graag Roy Sanders bedanken voor de mooie foto's van de robot. Ondanks dat je hebt aangegeven dat ze door mij zonder jouw naamvermelding vrij te gebruiken zijn, kan ik dit in mijn proefschrift niet onvermeld laten. De foto's tonen de robot namelijk niet alleen in volle trots en glorie, maar zijn ook een mooie herinnering aan dit unieke project.

Daarnaast zou ik ook graag de afdeling Radiotherapie willen bedanken voor de prettige en informele werksfeer, de gezellige koffiepauzes, en leuke activiteiten als afdelingsuitjes en borrels.

Daarbij noem ik graag alle promovendi van de afgelopen jaren: Nico, Alexander, Vera, Bob, Richard, Ellen, Anette, Greetje, Jan, Catalina, Ilona, Joana, Astrid, Sjoerd, Mette, Özlem, Anna, Alessandro, Kimmy, Christel en Mariska. Ik kijk met veel plezier terug op de spannende verhalen, nieuwtjes en grote onzin tijdens de koffiepauzes, gezamenlijke lunches, borrels, AIO-uitjes, promoties en congresfeestjes. Dankzij jullie was mijn promotietijd super.

Aansluitend wil ik (oud-)kamergenoten bedanken voor de prima werksfeer en onvergetelijke momenten: Nico, Astrid, Özlem, Alie en Stijn.

Ook wil ik Gijs en Alexis bedanken voor alle hulp tijdens het programmeren en Ric, Kees en Rob voor het bewerkstelligen van goede computerfaciliteiten, betrouwbare back-ups en het oplossen van alle grote en kleine computerproblemen.

De Promovendiraad wil ik bedanken en dan in het bijzonder: Maurits, Marijn, Kajo, Jan Willem, Sara en Maartje. Ik kan wel interessant zeggen 'voor de gelegenheid om me organisatorisch verder te ontwikkelen', maar het was eigenlijk een mooi excuus om gezellig samen te eten en te borrelen. Ook het Carnavallen in Tilburg was een onvergetelijk moment!

Ellen, ik wil je bedanken voor het delen van je goede ervaringen op de afdeling Radiotherapie. Door jou heb ik daar gesolliciteerd met de promotieplek als beloning. Al sinds de studententijd hebben we al een goede band en veel lol samen. Leuk dat dit op het werk nu ook zo is. Op borrels en feesten zoeken we elkaar altijd even op en staat er vaak al een biertje voor de ander te wachten.

Alexander, ook jou wil ik bedanken voor alle gezelligheid en het veelvuldig verzorgen van een slaapplek als er weer eens een feestje was. Was de kroeg al dicht dan gingen we bij jou nog even verder. Ook tijdens congressen hebben we veel lol gehad.

Bas, als kamergenoot op verschillende congressen heb ik je leren kennen als een hartelijk, gezellig en optimistisch persoon. Ik wil je graag bedanken voor de kans die je me hebt gegeven om me als post-doc verder te ontwikkelen als wetenschapper.

Naast collegae, wil ik graag vrienden en familieleden bedanken. Om te beginnen met Peter, Simon, Tristan en Thieo. Bedankt voor alle ontspanning en gezellige uitjes. Ondanks dat jullie uit Eindhoven vertrokken zijn, blijven we elkaar opzoeken voor avonden vol chinees, bier, (on)zinnige discussies, pokeren of stappen. Ook de jaarlijkse derde kerstdag, Nacht van Brabant, en HK-weekend zijn een goede uitlaatklep, waar ik nu al naar uitkijk. Polen, we komen eraan!

Peter, gaaf dat je mijn paranimf wilt zijn. We kennen elkaar al lang en hebben veel avonturen beleefd. Leuk dat we wekelijks nog strijden in de voetbalpool en op de squashbaan, waar we naderhand op adem komen met een 'klein' biertje. Verder vind ik het super om als introducé mee naar de PSV-wedstrijden te gaan. Ik hoop dat we dit alles nog lang zullen doen.

Simon, leuk dat we als oud-huisgenoten elkaar nog steeds zien en samen ons brein resetten door bijvoorbeeld te stappen (zelfs een keer op rolschaatsen) en te fifa'en, buiten alle HK activiteiten om.

Dan wil ook graag mijn oude studiegenoten Cathryn, Ellen, Ruud, Egon, Marjon, Anne, Vera, Karin, Karolien, en Maud bedanken voor de blijvende interesse in elkaar en de gezelligheid. Grappig dat we elkaar nu vaak ook op werkgerelateerde borrels of congressen tegenkomen, met lange nachten als gevolg. Een goede traditie is natuurlijk het jaarlijkse ME-weekend. Ruud en ik zijn al druk bezig met de voorbereidingen en het belooft weer een top-weekend te worden.

Daarnaast wil ik ook Arjen en Din Su bedanken. Het komt zelden voor dat goede vrienden ook je buren zijn. Dit is erg handig wanneer we even bij elkaar langs lopen voor een borrel, gezelschapsspel of een etentje. Ik hoop dat we dat nog lang kunnen doen.

Mijn familie: papa, mama, Maurice, Steffie, Jessica, Sjoerd, Maarten, Meike en Jasper, en schoonfamilie: Paul, Els en Eric, bedankt voor alle steun en gezelligheid die jullie me gaven en geven. Fijn dat we zo'n hechte familie zijn. Ondanks de verschillende interesses weten we van elkaar wat er speelt en proberen we altijd op elkaars verjaardag te zijn. Met de verjaardagen van de neefjes Julius, Floris en Tibbe, en het nichtje Pleun erbij is dat behoorlijk frequent. Ook de familieaangelegenheden als Kerst en dergelijke zijn goede ontspanmomenten, hoewel de blauwe plekken na stoeipartijtjes soms anders doen vermoeden.

Maurice, ik wil jou extra bedanken voor alle gezellige koffiepauzes en bijkletsmomenten, die we samen hebben kunnen houden, omdat we op het werk maar een paar gangen van elkaar af zitten. Vrijdag weer een bakkie?

Maarten, fijn dat je mijn paranimf wilt zijn. Als tweelingbroer zijn we heel verschillend, maar daardoor vullen we elkaar goed aan. Ik kijk er al naar uit om dit unieke moment met jou te delen.

Ik wil graag afsluiten met mijn lieve vriendin Esther. Naast je enthousiasme, liefde, gezelligheid en vrolijkheid, sta je altijd voor mij klaar, neem je me taken uit handen als er weer eens een deadline in zicht komt en ben je een luisterend oor. Bovendien beheers je de kunst van het relativeren, het geven van advies en het formuleren van mooie zinnen als de beste. Nu nog even vlammen voor je afstuderen, waarin ik je hopelijk net zo kan bijstaan, en daarna lekker samen op vakantie!

Publications

Published papers

van den Bosch MR, Lips IM, Lagerburg V, van Vulpen M, Lagendijk JJW, Moerland MA, "Feasibility of adequate dose coverage in permanent prostate brachytherapy using divergent needle insertion methods," *Radiother Oncol.* **86**, 120-125 (2008).

van den Bosch MR, Moerland MA, Lagendijk JJW, Bartels LW, van den Berg CAT, "New method to monitor RF safety in MRI-guided interventions based on RF induced image artefacts," *Med Phys.* **37**, 814-821 (2010).

van den Bosch MR, Moman MR, van Vulpen M, Battermann JJ, Duiveman E, van Schelven LJ, de Leeuw H, Lagendijk JJW, Moerland MA, "MRI-guided robotic system for transperineal prostate interventions: proof of principle," *Phys Med Biol.* **55**, 133-140. (2010).

Submitted papers

van den Bosch MR, de Leeuw H, Zwanenburg JJM, Lagendijk JJW, Moerland MA, "Single shot MR tagging to quantify local tissue deformation during MRI-guided needle interventions: a feasibility study," *Med Phys.* (2010).

van den Bosch MR, Moerland MA, de Leeuw H, van Schelven LJ, Dijkstra PT, van den Berg CAT, van Vulpen M, Lagendijk JJW, "The development and quality assurance of robotic devices for MRI-guided brachytherapy and tumour biopsy," *Phys Med Biol.* (2011).

Abstracts

van den Bosch MR, Lips IM, Lagerburg V, van Vulpen M, Lagendijk JJW, Moerland MA, "Feasibility of adequate dose coverage in permanent prostate brachytherapy using a MR guided implant robot and inverse planning based on simulated annealing," *9th biennial ESTRO conference on physics and radiation technology for clinical radiotherapy*, Barcelona, Spain, 2007.

Moerland, MA Lagerburg V, van den Bosch MR, van Vulpen M, Lagendijk JJW, "Robotic single needle implant method for MRI guided prostate brachytherapy," *9th biennial ESTRO conference on physics and radiation technology for clinical radiotherapy*, Barcelona, Spain, 2007.

van den Bosch MR, van den Berg CAT, Moman MR, van Vulpen M, Lagendijk JJW, Moerland MA, "Pre-clinical tests with an MRI compatible implant robot for permanent prostate brachytherapy," *27th ESTRO conference*, Gothenburg, Sweden, 2008.

Moerland MA, van den Bosch MR, Lagerburg V, Battermann JJ, van Vulpen M, Lagendijk JJW, "An MRI scanner compatible implant robot for prostate brachytherapy," *World congress of brachytherapy*, Boston, USA, 2008.

van den Bosch MR, van den Berg CAT, de Leeuw H, Bakker CJG, Moman MR, van Vulpen M, Lagendijk JJW, Moerland MA, "Quantification of MR image artefacts induced by implant robot for permanent prostate brachytherapy," *10th biennial ESTRO conference on physics and radiation technology for clinical radiotherapy*, Maastricht, The Netherlands, 2009.

van den Bosch MR, Moerland MA, van Lier ALHMW, Bartels LW, Lagendijk JJW, van den Berg CAT, "New method to quantify RF induced currents inside conductive wires," *17th scientific meeting & exhibition ISMRM*, Honolulu, USA, 2009.

Moerland MA, van den Bosch MR, de Leeuw H, Bakker CJG, Moman MR, van Vulpen M, Lagendijk JJW, "Magnetic field perturbations and geometric image distortions induced by implant robot for prostate brachytherapy," *GEC-ESTRO-ISIORT annual conference*, Porto, Portugal, 2009

van Schelven LJ, Dijkstra PT, van den Bosch MR, Moerland MA, Duiveman E, "MRI compatible robot for prostate brachytherapy, using tapping action for needle insertion," *World Congress - medical physics and biomedical engineering*, Munich, Germany, 2009.

van den Bosch MR, Moman MR, van Vulpen M, van Schelven LJ, de Leeuw H, Lagendijk JJW, Moerland MA, "First in-vivo experiments with an MRI-guided robotic device for prostate brachytherapy interventions," *29th ESTRO conference*, Barcelona, Spain, 2010.

van den Bosch MR, Moman MR, van Vulpen M, Battermann JJ, Duiveman E, van Schelven LJ, de Leeuw H, Lagendijk JJW, Moerland MA, "Proof of principle of an MR-compatible robot for MRI-guided interventions using a unique tapping device," *joint annual meeting ISMRM-ESMRMB*, Stockholm, Sweden, 2010.

van den Bosch MR, Moman MR, van Vulpen M, Battermann JJ, Duiveman E, van Schelven LJ, de Leeuw H, Lagendijk JJW, Moerland MA, "Proof of principle of an MR-compatible robot for MRI-guided interventions using a unique tapping device," *annual Benelux ISMRM meeting*, Utrecht, The Netherlands, 2010.

Dijkstra PT, van den Bosch MR, Moerland MA, van Schelven LJ, "Tapping robot for MRI guided prostate interventions: first experience with use in patients," *3rd Dutch biomedical engineering conference*, Egmond aan zee, The Netherlands, 2011.

Curriculum Vitae

Michiel Robertus van den Bosch was born on January 11, 1981 in Nijmegen, The Netherlands. He graduated from pre-university secondary education at the Kruisheren Kollege in Uden in 1999. In that year he started to study Biomedical Engineering at the Eindhoven University of Technology (TU/e). He completed the Master's program of Medical Engineering and obtained his Master of Science degree with great appreciation in 2006. During the Master's program, Michiel completed an internship on respiratory correlated computed tomography at MAASTRO in Heerlen. He performed his Master's thesis project on the development of a neonatal cerebral EEG-monitoring system at the Academic Hospital Maastricht. In 2006, he started his PhD research at the Department of Radiotherapy at the University Medical Center Utrecht, which concerned the clinical introduction of an MRI-guided robot for needle interventions in the prostate. Michiel presented the findings of his research at national and international conferences, and described them extensively in this thesis. Furthermore, results have been published in various peer-reviewed journals. In January 2011, he started as a post-doc on the MRI-accelerator project at the Department of Radiotherapy at the University Medical Center Utrecht.